UNIVERSITY
OF ICELAND

Ph.D. Dissertation
in Chemistry

Molecular Motors and Chiral Media

Ivan Tambovtsev

December 2025

FACULTY OF PHYSICAL SCIENCES

Molecular Motors and Chiral Media

Ivan Tambovtsev

Dissertation submitted in partial fulfillment of a
Philosophiae Doctor degree in Chemistry

Ph.D. Committee
Hannes Jónsson (Chair)
Elvar Örn Jónsson
Tetiana Orlova
Gianluca Levi

Opponents
Karl-Heinz Ernst
Gísli H. Jóhannesson

Faculty of Physical Sciences
School of Engineering and Natural Sciences
University of Iceland
Reykjavik, December 2025

Molecular Motors and Chiral Media

(Molecular Motors and Chiral Media)

Dissertation submitted in partial fulfillment of a *Ph.D.* degree in Chemistry

Faculty of Physical Sciences
School of Engineering and Natural Sciences
University of Iceland
Dunhagi 5
107 Reykjavík Reykjavik
Iceland

Telephone: 525-4700

Bibliographic information:
Ivan Tambovtsev, 2025, *Molecular Motors and Chiral Media* , Ph.D.Dissertation, Faculty of Physical Sciences, University of Iceland, 109 pp.

Author ORCID: 0000-0001-9223-8961
ISBN: 978-9935-578-02-0

Printing: Háskólaprent ehf.
Reykjavik, Iceland, December 2025

Abstract

Light-driven second-generation molecular motors offer a route to controllable nanoscale motion and energy conversion. This dissertation applies established electronic-structure methods to quantify and tune their photophysical and kinetic properties, with emphasis on both the optical absorption that initiates rotation, characterized using time-dependent density functional theory (TDDFT), and the thermal steps that set the overall timescale of rotation. The limitations of standard TDDFT for complex, multi-chromophoric systems are also assessed, validating a time-independent orbital-optimized approach for systems featuring coupled chromophores and spatially separated excitations. Minimum-energy paths are obtained with the climbing-image nudged elastic band method using energy and atomic forces coming from density functional theory calculations, and rate constants are estimated via harmonic transition state theory.

Two general substitution patterns emerge across representative overcrowded-alkene scaffolds. Replacing the methyl group at the stereogenic center by bulkier or more electronegative substituents such as trifluoromethyl, trichloromethyl, tert-butyl, or fully fluorinated tert-butyl consistently increases the rotational speed and often enlarges the spectral separation between stable and metastable states, improving selective photo-addressability. In contrast, replacing hydrogen at the stereogenic center by fluorine or chlorine slows down the rotation, narrows the spectral gap, and can even alter the reaction mechanism by favoring a competing pathway. Across all systems studied, barrier shifts dominate the kinetics while the prefactor does not change much.

These results establish simple chemical rules for controlling the timescale and spectral properties of molecular motors through targeted substitution. Beyond benchmarking motor–motor comparisons, these guidelines support the design of responsive materials, including motor-doped cholesteric liquid crystals, where light-controlled actuation, reconfigurable photonics, and the transport of chiral textures - which are shown to be governed by attractive and anisotropic inter-soliton forces - become accessible. The unified workflow from density functional theory to minimum-energy paths and harmonic transition state theory provides a practical route to predict and optimize motor performance in diverse materials contexts.

Ágrip

Ljósdrifnar sameindavélar af annarri kynslóð bjóða upp á leið til stýra hreyfingu og orkuflutningum á nanóskala. Í þessari ritgerð er rafeindabygging slíkra sameinda reiknuð til að magngreina og stilla ljósgleypni og snúningshraða þeirra. Ljósgleyðnin sem kemur snúningnum af stað er reiknuð með tímaháðri þéttnifellafræði (TDDFT), og varmadrifnu skrefin sem ákvarða heildartímaskala snúningsins reiknuð með virkjunarástandsaðferðinni. Einnig eru takmarkanir hefðbundinnar tímaháðrar þéttnifellafræði metnar fyrir flúrljómandi sameindavélar og þar er tímaóháð, svigrúmabestuð aðferð prófuð til að fá betri lýsingu á örvunum sem fela í sér rafeindaflutning. Lágmarksorkuleiðir eru fundnar með þéttnifellafræði og klifurmyndar hnykktu teygjubandsaðferðinni (CI-NEB), og hraðafastar eru metnir með kjörsveifilsnálgunum.

Bent er á möguleika til að bæta eiginleikar sameindavéla með því að skipta út atómum og hópum atóma. Þegar metýlhópnum við handhverfumiðjuna er skipt út fyrir fyrirferðarmeiri og rafeindadrægari skiptihópum, svo sem tríflúormetýl, tríklórmetýl, tert-bútýl eða alflúoraðan tert-bútýl, eykst snúningshraðinn undantekningalaust og í flestum tilfellum verður litrófsaðskilnaður milli stöðugra og hálfstöðugra ástanda meiri, sem bætir sértæka ljósörvun. Aftur á móti, ef vetni við handhverfumiðjuna er skipt út fyrir flúor eða klór hægir á snúningnum, litrófsbilið minnkar og hvarfkerfið getur jafnvel breyst með því að bakhvarfið verður ríkjandi. Í öllum kerfunum sem rannsökuð voru stýra breytingar á orkuþröskuldinum hraðafræðinni á meðan breytingar á forliðnum hafa lítl áhrif.

Með þessum niðurstöðum er hægt að setja fram einfaldar efnafræðilegar reglur til að stjórna tímaskala og litrófseiginleikum sameindavéla með markvissum skiptingum á atómhópum. Þannig er hægt að leiðbeina við hönnun á viðbragðsnæmum efnum, þar með talið kólesterískum fljótandi kristöllum með íbótarveilum, þar sem sameindavélar eru notaðar til að ná fram ljósstýrðri virkjun og flutningi á handhverfri áferð er stjórnast af kröftum milli einbylgja (solitons). Hið samþætta verkflæði frá þéttnifellafræði að lágmarksorkuferlum og virkjunarástandsaðferð innan kjörsveiflisnálgunarinnar býður upp á skilvirka leið til að spá fyrir um og hámarka afköst sameindavéla við hinar ýmsu aðstæður.

Table of Contents

List of Figures

List of Tables

List of Publications

Paper I: **Ivan Tambovtsev**, Yorick L. A. Schmerwitz, Gianluca Levi, Darina D. Darmoroz, Pavel V. Nesterov, Tetiana Orlova, and Hannes Jónsson (2025). Fine Tuning of the Rotational Speed of Light-Driven, Second-Generation Molecular Motors by Fluorine Substitution. *J. Phys. Chem. Lett.* 16, 4014-4020. *Author contribution:* Performed DFT/NEB/HTST calculations, analysed data, drafted manuscript. Co-authors contributed methodology, supervision, and discussion.

Paper II: **Ivan Tambovtsev** and Hannes Jónsson (accepted). Tuning Molecular Motors with Tert-Butyl and Fluorinated Tert-Butyl Groups. *J. Phys. Chem. A* (in press). *arXiv:2509.14572*. *Author contribution:* Conceived FtBu strategy, performed computations and analysis, wrote manuscript draft.

Paper III: **Ivan Tambovtsev**, Oskar Kristinsson, and Hannes Jónsson (in preparation). The Effect of Chlorine Substitution on Rotational Speed and Light Absorption of Second Generation Molecular Motors. *Author contribution:* Performed part of the DFT/NEB/HTST calculations, assisted in setting up workflows, provided guidance to co-author, supervised a master's student, contributed to data analysis and manuscript preparation.

Paper IV: **Ivan M. Tambovtsev**, Igor S. Lobanov, Alexei D. Kiselev, and Valery M. Uzdin (2023). Pair interaction of localized topological structures in confined chiral media. *Phys. Rev. E* 108, 024705. *Author contribution:* Developed the three-step minimization procedure, performed numerical analysis of inter-soliton potentials, prepared figures, and wrote the manuscript draft.

Abbreviations

BO Born-Oppenheimer

CI-NEB Climbing-Image Nudged Elastic Band

CLC Cholesteric Liquid Crystal

CT Charge-Transfer

DFT Density Functional Theory

DO Direct Optimization

FR-DO Freeze-and-Release Direct Optimization

GGA Generalized Gradient Approximation

GMF Generalized Mode Following

HF Hartree-Fock

HOMO Highest Occupied Molecular Orbital

HTST Harmonic Transition State Theory

KS Kohn-Sham

LDA Local Density Approximation

LR-TDDFT Linear Response Time-Dependent Density Functional Theory

LUMO Lowest Unoccupied Molecular Orbital

MEP Minimum Energy Path

MOM Maximum Overlap Method

NEB Nudged Elastic Band

OCA Overcrowded-Alkene

PES Potential Energy Surface

SCF Self-Consistent Field

SF-TDDFT Spin-Flip Time-Dependent Density Functional Theory

S-IDPP Sequential-Image Dependent Pair Potential

TDDFT	Time-Dependent Density Functional Theory
THI	Thermal Helix Inversion
TI	Thermal Isomerization
TS	Transition State
TST	Transition State Theory
XC	Exchange-Correlation

Acknowledgements

I thank my advisor, Prof. Hannes Jónsson, for his guidance and support throughout this work, and my committee members Elvar Örn Jónsson, Tetiana Orlova, and Gianluca Levi for their valuable feedback.

I acknowledge the Icelandic Research Fund for supporting this work through a research grant, and the Icelandic High Performance Computing Centre for providing access to computational resources that made this research possible.

I am deeply grateful to my former supervisor, Prof. Valery Uzdin, whose initial collaboration and guidance sparked my research on molecular motors and led to my time in Iceland.

I am deeply grateful to Yorick Schmerwitz, who first introduced me to the field of computational chemistry, and to my colleagues Alejandro Peña Torres and Elli Inkeri Selenius, whose company and collaboration at the office have accompanied me from the very beginning of my Ph.D. to its completion. I would also like to thank Óskar Kristinsson for his valuable contributions as a co-author and colleague. I also thank Magnus Christiansen and V who joined along the way and made the work environment all the more enjoyable.

Among my colleagues, I am especially thankful to Moritz Sallermann and Amrita Goswami, as well as Rohit Goswami, for their friendship, kindness, and the many moments we shared beyond work. Their support and companionship have meant a great deal to me throughout this journey.

I also thank my colleagues in VRIII at the University of Iceland for discussions and for creating such a supportive and inspiring working environment.

My heartfelt gratitude goes to my parents for their love and care, to my grandparents for their unwavering support, and to my wife, Mariia, for moving to Iceland with me and for her constant companionship and encouragement throughout these years. I am also thankful to my friends Pavel and Anna for visiting me here in Iceland and for their continued friendship.

1 Introduction

One of the central goals of modern chemistry and materials science is to control structure and motion at the nanoscale. The 20th century established reliable routes to build static molecular architectures, from stereoselective synthesis to supramolecular assembly, enabling precise control over composition and shape [1, 2]. Early discussions of nanotechnology already emphasized that useful function would ultimately require molecules that could operate as machines, rather than simply forming static architectures.

Multiple strategies for nanoscale control over the assembly and placement of components then emerged. Self-assembly provided a general route to order across length scales [3], nucleic acids enabled programmable bottom-up design [4], and directed nanoparticle assembly bridged molecular design to mesoscale materials [5]. Complementary top-down approaches and soft lithography supplied external patterning at the nanometer to micrometer scale.

Against this backdrop, the notion of molecules as machines gained traction. Balzani, Credi, and Venturi argued for deliberately engineered nanoscale motion and responsiveness as chemical design targets [6, 7]. Biology offered concrete templates: ATP synthase, kinesin, and photosynthetic complexes translate electrochemical gradients or photons into directional motion and charge flow. Reproducing even simplified versions of these biological complexes in synthetic systems became a key challenge at the interface of chemistry, physics, and materials science [8, 9, 10, 11].

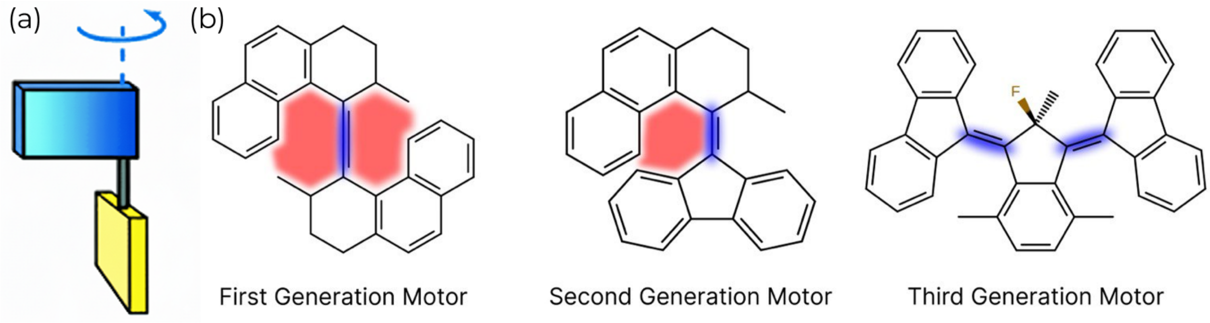

Figure 1.1. Overview of the systems used throughout this thesis. (a) Conceptual scheme of a light-driven overcrowded-alkene motor: a stator (yellow) and a rotor (blue) connected by an overcrowded C=C bond undergo unidirectional motion via cyclic photo/thermal steps. (b) Representative first–third generation designs. First-generation motors employ two stereocenters and helical strain; second-generation motors achieve directionality with a single stereocenter that also imparts a helical shape. The fjord region (red) and axial (blue) elements control the thermal rotational barrier, which is the focus of this work.

The 2016 Nobel Prize in Chemistry, awarded to Sauvage, Stoddart, and Feringa recognized the design and synthesis of molecular machines [12]. Catenanes and rotaxanes established mechanically interlocked architectures as controllable motifs [13, 14], and Overcrowded-Alkene (OCA) motors realized light-driven, unidirectional rotation with directionality encoded by stereochemistry and helical strain (Fig. 1.1a) [15, 16].

For OCA motors, the rotary cycle comprises two fast photochemical isomerizations and two slower thermal relaxation steps. These relaxation steps set the characteristic timescale of rotation. Experiments have shown that substituents at the stereogenic center and within the fjord region (Fig. 1.1b) strongly affect the kinetics of the thermal steps [17, 18, 19], yet predictive rules for tuning it remain incomplete. Developing these rules is a critical step toward designing motors that can operate on timescales compatible with the viscoelastic response of soft-matter hosts, enabling precise temporal control over material properties.

That need for predictive control is especially acute when motors are integrated into functional materials, where their nanoscale motion must be coupled to a macroscopic response.

Embedding motors in anisotropic hosts offers a route to translate molecular rotation into material response [20, 21]. Liquid crystalline networks (LCNs) are particularly effective, as their unique anisotropy and long-range order allow for efficient supramolecular amplification of molecular motion. In these systems, the motor often functions as both a cross-linker and a chiral dopant; consequently, its light-driven changes in shape and chirality directly modulate the helical pitch of the host material [22, 21]. This mechanism translates nanoscale rotation into diverse macroscopic functions, including color tuning, the rotation of micro-objects, and complex mechanical movements such as bending, walking, and reversible left- or right-handed helical coiling [22, 20]. In motor-doped Cholesteric Liquid Crystals (CLCs), the thermal relaxation timescale therefore controls not only molecular kinetics but also mesoscale optical and mechanical behavior. A notable example is the persistent clockwise/counter-clockwise supramolecular rotation observed under steady illumination (Fig. 1.2) [23, 24, 25, 26]. Recent demonstrations using motor-doped CLC microdroplets for optical information handling further motivate quantitative control over this thermal step [27].

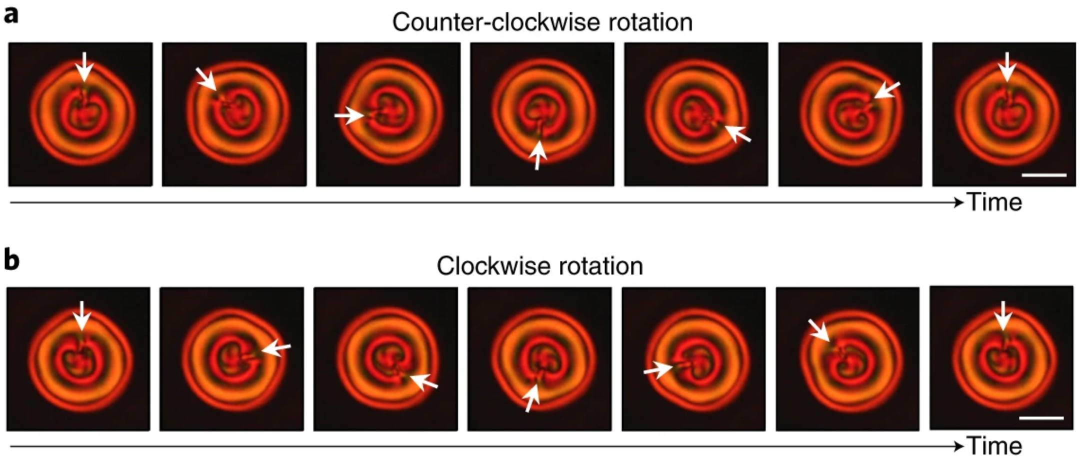

Figure 1.2. Continuous clockwise and counter-clockwise supramolecular rotation in motor-doped cholesteric liquid crystals under steady illumination. Reproduced with permission from Ref. [23].

2 Quantum Mechanical Foundations

2.1 Time-Independent Schrödinger Equation

The goal of quantum mechanical calculations in chemistry and physics is to describe the behavior of electrons and nuclei in a system by solving the time-independent Schrödinger equation [28]:

$$\hat{H}\psi = E\psi, \tag{1}$$

where $\hat{H}$ is the Hamiltonian operator, ψ is the wavefunction of the system, and E is the total energy eigenvalue. The Hamiltonian can be expressed as a sum of kinetic and potential energy contributions:

$$\hat{H} = \hat{T}_e + \hat{T}_n + \hat{V}_{ne} + \hat{V}_{ee} + \hat{V}_{nn}. \tag{2}$$

Here, $\hat{T}_e$ and $\hat{T}_n$ denote the kinetic energies of electrons and nuclei, respectively; $\hat{V}_{ne}$ is the electron–nucleus attraction; $\hat{V}_{ee}$ is the electron–electron repulsion; and $\hat{V}_{nn}$ is the nucleus–nucleus repulsion.

In practice, solving this full many-body equation exactly is only possible for hydrogen-like systems. For molecules or solids containing many electrons, the problem becomes computationally intractable due to the $3N$-dimensional nature of the wavefunction (where N is the number of electrons). Approximations are therefore essential to reduce this complexity while retaining predictive accuracy.

2.2 Born-Oppenheimer Approximation

The first key simplification is the Born-Oppenheimer (BO) approximation [29]. Nuclei are significantly heavier than electrons, so their motion is several orders of magnitude slower. Consequently, electrons can be assumed to instantaneously adjust to changes in nuclear positions, and the nuclear kinetic energy operator $\hat{T}_n$ can be neglected in the electronic problem.

Under this approximation, the total wavefunction factorizes as

$$\Psi(\mathbf{r},\mathbf{R}) = \Psi_n(\mathbf{R})\,\Psi_e(\mathbf{r};\mathbf{R}), \tag{3}$$

where $\mathbf{r}$ are electronic coordinates, $\mathbf{R}$ are nuclear coordinates, $\Psi_n(\mathbf{R})$ is the nuclear wavefunction, and $\Psi_e(\mathbf{r};\mathbf{R})$ is the electronic wavefunction parametrically dependent on nuclear positions. The electronic Hamiltonian at fixed nuclei is then

$$\hat{H}_{ele}\Psi_e = \left[-\tfrac{1}{2}\sum_{i=1}^{N}\nabla_i^2 - \sum_{i=1}^{N}\sum_{A=1}^{M}\frac{Z_A}{|\mathbf{r}_i - \mathbf{R}_A|} + \sum_{i=1}^{N}\sum_{j>i}^{N}\frac{1}{|\mathbf{r}_i - \mathbf{r}_j|}\right]\Psi_e = E_{ele}\Psi_e. \tag{4}$$

The total energy is obtained by adding the classical nucleus–nucleus repulsion:

$$E = E_{ele} + \sum_{A<B} \frac{Z_A Z_B}{|\mathbf{R}_A - \mathbf{R}_B|}. \tag{5}$$

The BO approximation greatly simplifies the quantum problem, enabling separate treatment of electronic structure and nuclear dynamics. It underlies nearly all modern electronic structure methods, including Hartree-Fock (HF) and Density Functional Theory (DFT).

2.3 Hartree-Fock Theory

Even after applying the BO approximation, the many-electron Schrödinger equation remains unsolvable in closed form. Hartree proposed an approximate solution by introducing a Self-Consistent Field (SCF) method [30]. The idea is to approximate the N-electron wavefunction as a product of single-electron orbitals $\psi_i(\mathbf{r}_i)$. However, such a product neglects the antisymmetry requirement of fermions.

To enforce antisymmetry, Slater introduced the determinant form of the wavefunction [31]:

$$\Psi(\mathbf{x}_1, \mathbf{x}_2, \ldots, \mathbf{x}_N) = \frac{1}{\sqrt{N!}} \begin{vmatrix} \chi_1(\mathbf{x}_1) & \chi_2(\mathbf{x}_1) & \cdots & \chi_N(\mathbf{x}_1) \\ \chi_1(\mathbf{x}_2) & \chi_2(\mathbf{x}_2) & \cdots & \chi_N(\mathbf{x}_2) \\ \vdots & \vdots & \ddots & \vdots \\ \chi_1(\mathbf{x}_N) & \chi_2(\mathbf{x}_N) & \cdots & \chi_N(\mathbf{x}_N) \end{vmatrix}, \tag{6}$$

where $\chi_i(\mathbf{x})$ are spin-orbitals, which are single-electron wavefunctions that depend on both the spatial coordinates ($\mathbf{r}$) and the spin state (s) of an electron. The Slater determinant automatically changes sign under exchange of two electrons, fulfilling the Pauli exclusion principle.

In Hartree-Fock theory, each electron moves in the average field of all the others. The Hamiltonian for electron i takes the form:

$$\hat{h}(i) = -\tfrac{1}{2}\nabla_i^2 - \sum_{A=1}^{M} \frac{Z_A}{|\mathbf{r}_i - \mathbf{R}_A|} + V_i^{HF}, \tag{7}$$

where the Hartree-Fock potential V_i^{HF} incorporates electron–electron interactions via the Coulomb operator $\hat{J}$ and the exchange operator $\hat{K}$:

$$V_i^{HF}(\mathbf{x}_1) = \sum_{j=1}^{N} \left(\hat{J}_j - \hat{K}_j\right). \tag{8}$$

These terms are nonlinear in the orbitals, so the equations must be solved iteratively until self-consistency is reached. This is the Hartree-Fock SCF procedure [32].

Hartree-Fock includes exchange exactly but neglects dynamic electron correlation, i.e. the instantaneous interactions between electrons. As a result, HF typically overestimates total energies, and the missing contribution is called the *correlation energy*. Post-HF methods such as configuration interaction (CI) [33, 34] and coupled cluster (CC) [35] systematically recover correlation, but their cost scales steeply with system size. Alternatively, DFT offers an efficient way to incorporate correlation at a lower computational cost, which has made it a widely used method in chemistry and materials science.

3 Density Functional Theory and Gaussian Basis Sets

3.1 Foundations: Hohenberg-Kohn and Kohn-Sham Formulations

DFT rests on the central insight that the electron density $\rho(\mathbf{r})$, a function of only three spatial coordinates, contains all the information needed to describe a many-electron system. The first Hohenberg-Kohn theorem establishes a one-to-one correspondence between the ground-state density and the external potential $v_{\text{ext}}(\mathbf{r})$, ensuring that $\rho(\mathbf{r})$ uniquely defines the Hamiltonian and thus all ground-state properties [36, 37, 38]. The second theorem provides a variational principle: for any trial density $\tilde{\rho}$, the energy functional $E[\tilde{\rho}]$ lies above or equal to the exact ground-state energy, achieving equality only if $\tilde{\rho}$ is the true ground-state density. Together, these results make the density a fundamental variable of quantum mechanics.

Kohn and Sham recast the many-body problem into an auxiliary noninteracting one [39]. The electrons move in an effective potential,

$$\hat{H}_{\text{KS}}[\rho]\phi_i = \left(-\tfrac{1}{2}\nabla^2 + v_{\text{ext}} + v_H[\rho] + v_{xc}[\rho]\right)\phi_i = \varepsilon_i\phi_i, \tag{9}$$

where $v_H[\rho]$ is the classical Coulomb (Hartree) potential and $v_{xc}[\rho]$ is the Exchange-Correlation (XC) contribution. Self-consistent solution of the Kohn-Sham (KS) equations yields the orbitals ϕ_i and density $\rho(\mathbf{r}) = \sum_i^{\text{occ}} |\phi_i(\mathbf{r})|^2$. In practice, the exact form of v_{xc} is unknown and must be approximated, which largely determines the accuracy and applicability of DFT.

3.2 Exchange-Correlation Approximations in Practice

A useful metaphor for XC functionals is "Jacob's ladder" of approximations, with each rung bringing us closer to "chemical heaven" of exact results [40].

- The Local Density Approximation (LDA) references the homogeneous electron gas. It is computationally stable but often overbinds molecules and solids [41, 42].
- Generalized Gradient Approximations (GGAs) include density gradients, improving structural parameters and atomization energies. PBE is a widely used example [43, 44].
- *Hybrid functionals* incorporate a fraction of exact Hartree-Fock exchange, mitigating self-interaction error and improving barrier heights and excitation spectra. B3LYP has become a standard in organic and organometallic chemistry [45, 46].

- *Range-separated hybrids* and screened exchange functionals (e.g., HSE) treat short- and long-range exchange differently, improving charge-transfer excitations and some barrier problems [47].
- Higher-rung methods such as double hybrids or explicitly correlated approaches can approach coupled-cluster accuracy but at considerably increased cost. These functionals are "double" because they mix in both exact Hartree-Fock exchange and a portion of non-local correlation energy from wave-function methods, typically second-order Møller-Plesset perturbation theory (MP2) [48].

Thus, at the lower end, LDA or simple GGA functionals are inexpensive but often too crude; at the higher end, double hybrids or wavefunction-based methods are accurate but too computationally demanding for systematic studies of medium-sized molecules. The practical balance between accuracy and cost for these types of systems is achieved by hybrid functionals such as B3LYP, which are therefore widely adopted as a community standard.

3.3 Gaussian Basis Sets: From Minimal to Polarized/Diffuse

In practice, KS orbitals are represented as linear combinations of basis functions. Gaussian type orbitals (GTOs) are standard because they enable analytic evaluation of multicenter integrals, introduced by Boys in 1950 [49]. Although Slater-type orbitals more closely resemble the exponential decay of true atomic orbitals [50], their integrals are much harder to compute.

Contracted Gaussians combine several primitives to approximate Slater forms efficiently. Minimal basis sets (STO-nG) assign one contracted function per occupied atomic orbital but are too rigid for realistic chemistry. Split-valence sets, such as 3-21G or 6-31G, introduce multiple functions for valence orbitals, offering greater flexibility while keeping compact core descriptions [51]. Two important extensions are routinely employed to handle the trade-off between accuracy and computational cost. Polarization functions (higher angular momentum), which account for anisotropy in bonding and transition states - for example, d-functions on heavy atoms or p-functions on hydrogens allow the orbitals to distort appropriately - and diffuse functions, indicated by “$+$”, which add very small exponents to capture extended electron density in anions, Rydberg states, or weakly bound complexes.

While minimal or unpolarized basis sets are computationally efficient, they lack the flexibility to describe reaction barriers and weak interactions. At the other extreme, large triple-ζ and quadruple-ζ sets with extensive diffuse and polarization functions can approach the complete basis set limit but at prohibitive cost for large series of molecules.

3.4 Balanced Protocols

Between these extremes, a practical compromise has emerged that combines a hybrid functional with a polarized split-valence basis set, most commonly B3LYP/6-31G(d,p). This level of theory has been extensively benchmarked and has become a reliable standard for studying main-group organic systems, including light-driven molecular motors. It provides accurate structures, vibrational spectra, and relative barrier heights at a computational cost that makes systematic studies feasible, establishing it as the workhorse for exploring reactivity and dynamics in this field. As such, it has been applied in several representative studies, such as Bauer *et al.*[18], Carfora *et al.*[52], and Kistemaker *et al.*[53].

4 Kinetics on Potential Energy Surfaces

4.1 Harmonic Transition State Theory

Thermally activated reaction rates are commonly described by Transition State Theory (TST), which assumes that the system passes through a dividing surface at the saddle point of the PES without recrossing. HTST, both the minimum and the transition structure are modeled as multidimensional harmonic oscillators, and the rate constant can be written in the Vineyard form [54, 55]:

$$k_{\mathrm{HTST}}(T) = \frac{\prod_{i=1}^{3N-6} \nu_i^{(\mathrm{min})}}{\prod_{j=1}^{3N-7} \nu_j^{(\ddagger)}} \exp\left[-\frac{E^{\ddagger} - E^{\mathrm{min}}}{k_B T}\right]. \tag{10}$$

Here, $\nu_i^{(\mathrm{min})}$ and $\nu_j^{(\ddagger)}$ are the real vibrational frequencies at the minimum and transition structure, respectively, and the exponential factor reflects the Boltzmann probability of surmounting the barrier $\Delta E^{\ddagger}$. The denominator omits the single imaginary frequency of the saddle point.

This formulation highlights two contributions: an entropic prefactor determined by the ratio of vibrational frequencies, and an energetic Boltzmann factor for barrier crossing. In practice, barrier shifts dominate rate variations, while prefactors change more modestly. For multiple competing channels, individual rate constants add, and half-lives follow as $t_{1/2} = \ln 2/k$. Frequency analyses also serve as diagnostics: minima exhibit no imaginary frequencies, whereas first-order saddles have exactly one.

4.2 Minimum-Energy Paths: NEB, CI-NEB, and NEB-TS

Understanding kinetics requires not only energies at stationary points but also the path connecting them. The Minimum Energy Path (MEP) is defined as the steepest-descent trajectory linking reactants, transition states, and products, and it necessarily passes through the first-order saddle that determines the activation barrier.

The NEB method provides a practical strategy to approximate the MEP [56, 57]. A discrete set of “images” of the system is distributed between two minima and connected by harmonic springs to emulate an elastic band. The total force on image i is written as

$$\mathbf{F}_i = -\nabla V(\mathbf{R}_i) + \mathbf{F}_i^{\mathrm{spring}}, \tag{11}$$

with $\nabla V(\mathbf{R}_i)$ the interatomic force and

$$\mathbf{F}_i^{\mathrm{spring}} = k_{i+1}(\mathbf{R}_{i+1} - \mathbf{R}_i) - k_i(\mathbf{R}_i - \mathbf{R}_{i-1}) \tag{12}$$

the spring contribution. To avoid artifacts such as “corner cutting” or “sliding” into minima, forces are projected onto components parallel and perpendicular to the local tangent $\hat{\tau}_i$. The nudged force then becomes

$$\mathbf{F}_i^0 = -\nabla V(\mathbf{R}_i)\big|_\perp + \left(\mathbf{F}_i^{\text{spring}} \cdot \hat{\tau}_i\right) \hat{\tau}_i, \tag{13}$$

so that only the perpendicular component of the true force drives relaxation, while the parallel spring term maintains image distribution. At convergence, the perpendicular force vanishes,

$$\nabla V(\mathbf{R}_i)\big|_\perp = 0, \tag{14}$$

and the band coincides with the MEP (Fig. 4.1).

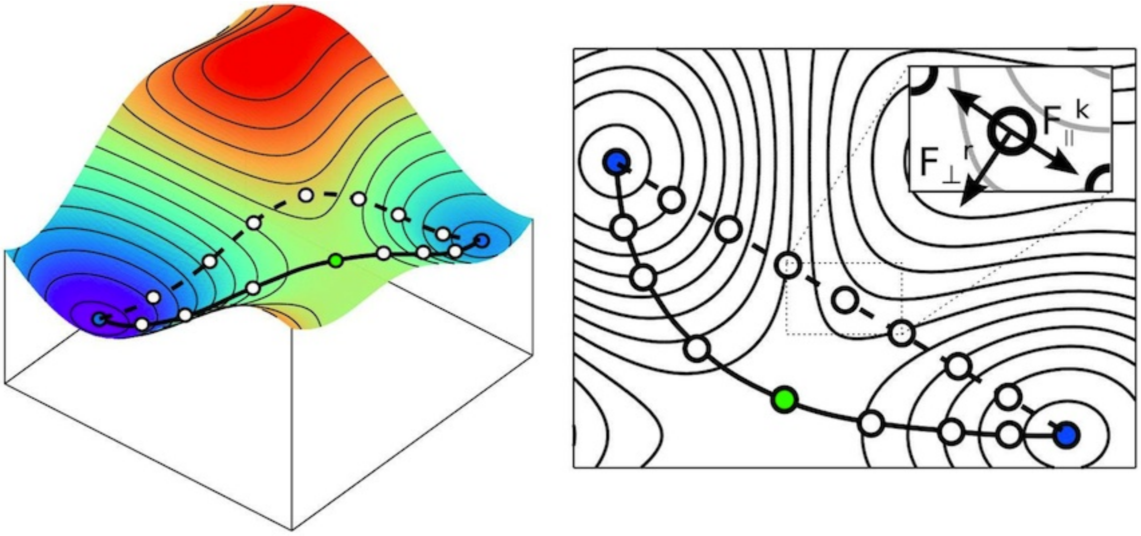

Figure 4.1. Principle of the NEB method. The dashed line shows the path corresponding to the initial guess for intermediate states. After NEB optimization, the images relax onto the minimum-energy path (solid line). The green dot marks the transition state (saddle point). Reproduced from Ref. [58].

The Climbing-Image Nudged Elastic Band (CI-NEB) refines the method by driving the highest-energy image uphill along the tangent while relaxing perpendicular degrees of freedom [59]. This ensures direct convergence onto the saddle point without prior knowledge of its location. For quantitative kinetics, a further refinement (NEB-TS) is typically performed [60], enforcing strict stationarity and yielding vibrational spectra suitable for HTST.

In practice, the quality of the initial geometries of the images strongly affects convergence speed and robustness. Rather than relying on simple linear interpolation, this work employs the Sequential-Image Dependent Pair Potential (S-IDPP) scheme [61], which constructs initial paths by minimizing an auxiliary potential based on interatomic distances. The resulting initial bands follow chemically reasonable rearrangements from the outset, significantly reducing the number of iterations required for NEB convergence and improving overall stability.

5 Methods for Calculating Excited Electronic States

While ground-state DFT provides access to equilibrium structures and energetics, many photophysical and photochemical phenomena, like the operation of molecular motors, require explicit treatment of electronically excited states. This chapter reviews computational methods based on DFT for accessing these higher-energy states, covering both the widely used TDDFT approach and alternative orbital-optimized methods that target excited states directly as stationary points on the electronic energy surface.

5.1 Time-Dependent Density Functional Theory

TDDFT extends the ground-state DFT formalism to describe systems evolving in time, particularly under the influence of a time-dependent external electrical field.

5.1.1 General Framework

The theoretical foundation is the Runge-Gross theorem [62], which states that for a given initial state, the time-dependent electron density $\rho(\mathbf{r},t)$ uniquely determines the time-dependent external potential $v_{\text{ext}}(\mathbf{r},t)$ (up to a time-dependent constant). This implies that $\rho(\mathbf{r},t)$ contains all information about the system's time evolution.

In the KS formulation of TDDFT, the system is mapped onto an auxiliary non-interacting system evolving under an effective time-dependent potential. The time-dependent KS orbitals $\phi_i(\mathbf{r},t)$ satisfy the time-dependent KS equations:

$$i\frac{\partial}{\partial t}\phi_i(\mathbf{r},t) = \hat{h}_{KS}[\rho](\mathbf{r},t)\phi_i(\mathbf{r},t) = \left[-\tfrac{1}{2}\nabla^2 + v_{\text{ext}}(\mathbf{r},t) + v_H[\rho](\mathbf{r},t) + v_{xc}[\rho](\mathbf{r},t)\right]\phi_i(\mathbf{r},t) \quad (15)$$

The main challenge lies in approximating the time-dependent exchange-correlation potential $v_{xc}[\rho](\mathbf{r},t)$. Most applications employ the adiabatic approximation, where v_{xc} at time t is approximated using a ground-state XC functional evaluated at the instantaneous density $\rho(\mathbf{r},t)$. This neglects memory effects but makes calculations feasible with standard ground-state functionals.

5.1.2 Linear-Response TDDFT and its Limitations

For calculating vertical excitation energies and oscillator strengths (absorption intensities), the most common approach is Linear Response Time-Dependent Density Functional Theory (LR-TDDFT) [63]. It analyzes the first-order change (linear response) of the ground-state density to a weak, oscillating external field perturbation. This leads to a frequency-dependent eigenvalue problem whose solutions yield the vertical excitation energies and oscillator strengths. LR-TDDFT is the workhorse for calculating UV-Vis absorption spectra in computational chemistry.

Despite its success, adiabatic LR-TDDFT has significant limitations: It cannot properly describe states with significant double-excitation character due to the linear response formalism and the adiabatic approximation [64]. Furthermore, standard local (LDA) and semi-local (GGA) XC functionals often fail dramatically for long-range Charge-Transfer (CT) excitations [65] and Rydberg states [66]. This is because the XC part of their potential decays too rapidly, failing to correctly cancel the long-range self-interaction from the Hartree term [66]. The resulting effective potential is too repulsive at long range, which leads to a severe underestimation of these excitation energies [65, 66]. Hybrid functionals (mixing in exact exchange), and especially range-separated hybrids, often improve results but increase computational cost. The description of the topography around conical intersections, particularly between the ground state (S_0) and the first excited state (S_1), can also be qualitatively incorrect [64], which is problematic for modeling photochemistry. Finally, the accuracy is highly dependent on the chosen XC functional.

Nevertheless, for the valence $\pi \rightarrow \pi^*$ excitations typical in overcrowded-alkene molecular motors, LR-TDDFT with a suitable hybrid functional (like B3LYP or PBE0) often provides chemically reasonable trends in excitation energies and spectral shifts upon substitution, even if absolute energies are not perfect [52, 67]. Errors in absolute excitation energies tend to cancel when comparing substituted scaffolds, so relative shifts between stable and metastable states are predicted reliably. These relative trends are precisely what is required to assess selective photoaddressability in molecular motors.

In summary, although LR-TDDFT has intrinsic limitations, it remains a practical and widely validated approach for calculating excitation spectra in the present context. Its computational efficiency enables systematic screening of substitution effects, while its accuracy is sufficient to capture the spectral shifts that underpin the design rules discussed in this thesis.

5.2 Orbital-Optimized DFT for Excited States

An alternative strategy, referred to as Orbital-Optimized (OO) DFT, avoids the time-dependence and response theory altogether, seeking excited states directly as higher-energy stationary solutions to the time-independent KS equations. These solutions correspond to optimizing a single Slater determinant with a specific non-Aufbau electron configuration (i.e., not filling the lowest energy orbitals first) [68].

These higher-energy stationary points are typically saddle points on the electronic energy surface (energy as a function of orbital variations), whereas the ground state is the global minimum. The order of the saddle point, which is the number of negative eigenvalues of the electronic Hessian, loosely relates to how many states lie below it, although this relationship is not always strictly monotonic for approximate functionals.

This state-specific approach significantly benefits from including orbital relaxation effects tailored for the target excited state, an effect often missing or approximated in LR-TDDFT. This makes variational methods particularly promising for states involving substantial electron density rearrangement, such as CT or core excitations, where LR-TDDFT often struggles.

5.2.1 Challenges: Variational Collapse and Saddle Point Finding

The primary challenge in orbital-optimized calculations is converging to the desired higher-energy saddle point without suffering variational collapse, where the optimization falls back to the ground state or a lower-energy solution.

Several strategies have been developed to locate the desired saddle points. These include extending the standard SCF procedure with a Maximum Overlap Method (MOM) to guide convergence [69, 70]. To improve robustness, MOM can be combined with more stable Direct Optimization (DO) techniques [70]. More targeted approaches are also available, such as Generalized Mode Following (GMF), which is specifically designed to converge onto a saddle point of a predetermined order [71]. For particularly difficult cases like CT states, a two-step Freeze-and-Release Direct Optimization (FR-DO) strategy provides a robust path to the correct solution by first relaxing the orbitals while keeping the hole and excited electron orbitals frozen before a full, unconstrained optimization [72].

5.2.2 Spin Contamination and Purification

A nuance arises when using unrestricted DFT (allowing different spatial orbitals for α and β spins) to calculate open-shell singlet states, which commonly result from single electronic excitations. The resulting single Slater determinant wavefunction is not an eigenfunction of the total spin operator $\hat{S}^2$; it is spin-contaminated, typically representing a mixture of the desired singlet state and the corresponding triplet state. While this affects properties sensitive to spin density, the energy can often be approximately corrected using spin purification (or approximate spin projection) techniques. A widely used formula estimates the pure singlet energy (E_S) based on the energy computed for the mixed state (E_{mix}) and the energy of the corresponding pure triplet state (E_T), calculated separately [73]:

$$E_S \approx 2E_{mix} - E_T \tag{16}$$

This approximation assumes a 50/50 mix of singlet and triplet character, which is often a reasonable starting point for states derived from single excitations.

5.3 Limitations of TDDFT: The BODIPY/Motor Case

While LR-TDDFT has proven to be a robust and efficient method for predicting the absorption spectra of the single-chromophore molecular motors analyzed throughout this thesis, its limitations become apparent when applied to more complex, multi-chromophoric systems. A prominent example of such a challenging case is the BODIPY/Motor hybrid that chemically links a second-generation rotary motor to a highly photoluminescent BODIPY dye [74].

This molecule is designed to have two distinct photo-addressable functions: rotation (driven by the motor) and luminescence (from the dye). These functions correspond to two distinct low-energy electronic excitations: one localized on the motor moiety (experimentally at ∼390 nm) and one on the BODIPY moiety (experimentally at ∼500 nm) [74]. The experimental separation between these peaks is therefore approximately 110 nm. The challenge for TDDFT arises from the moderate electronic interaction between these two parts. As shown in Figure 5.1, the frontier orbitals are spatially segregated: the HOMO and LUMO are localized on the BODIPY part of the molecule, while the HOMO-1 and LUMO+1 are localized on the motor.

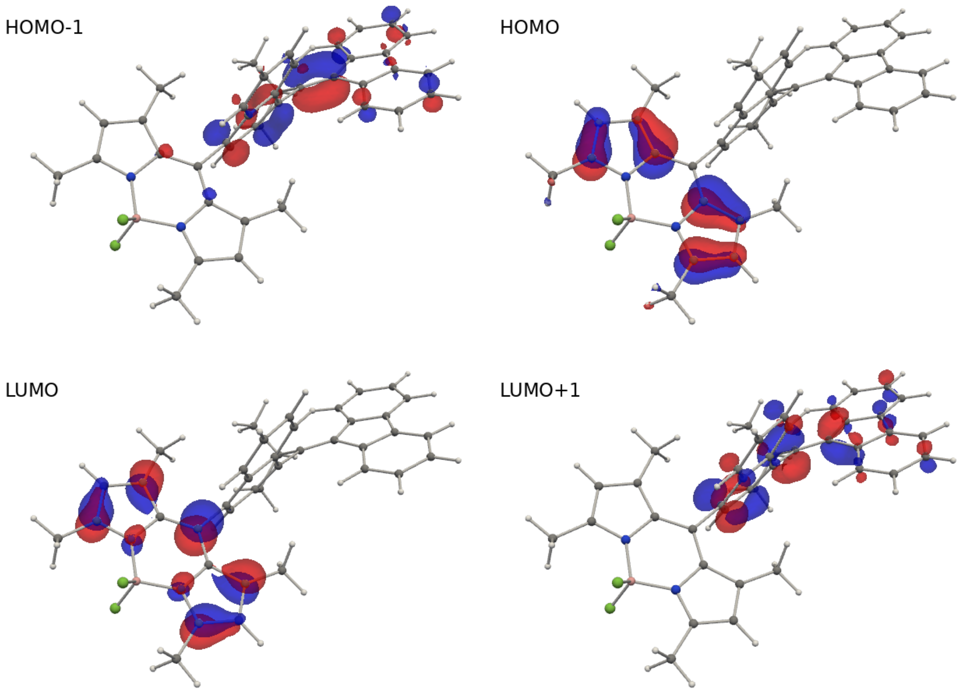

Figure 5.1. Two highest occupied and two lowest unoccupied orbitals in the BODIPY/Motor ground state singlet, HOMO and LUMO orbitals are localized in the BODIPY part of the molecule, HOMO-1 and LUMO+1 are localized in the Motor part of the molecule

The challenges for response-based methods in modeling this system are illustrated in Figure 5.2. This includes not only standard LR-TDDFT but also Spin-Flip Time-Dependent Density Functional Theory (SF-TDDFT). SF-TDDFT is an alternative response-based approach that obtains excited states (like singlets) by applying a spin-flipping excitation operator to a high-spin triplet reference state [75]. While SF-TDDFT can sometimes improve the description of states with double-excitation character or near-degeneracies where LR-TDDFT fails, its shortcomings are also apparent here.

Figure 5.2 demonstrates how these methods fail to reproduce the experimental spectrum (gray dashed line). A TDDFT calculation using the B3LYP functional (top-left) incorrectly switches the order of the motor and BODIPY excitations, while SF-TDDFT with B3LYP functional (bottom-left) fails to locate the motor transition. The TDDFT method with BHandHLYP functional (top-right) gives results that differ strongly from the experimental measurements, and while SF-TDDFT with BHandHLYP functional (bottom-right) was used in the original paper [74], it still produces a large error of 90 nm for the lowest excitation.

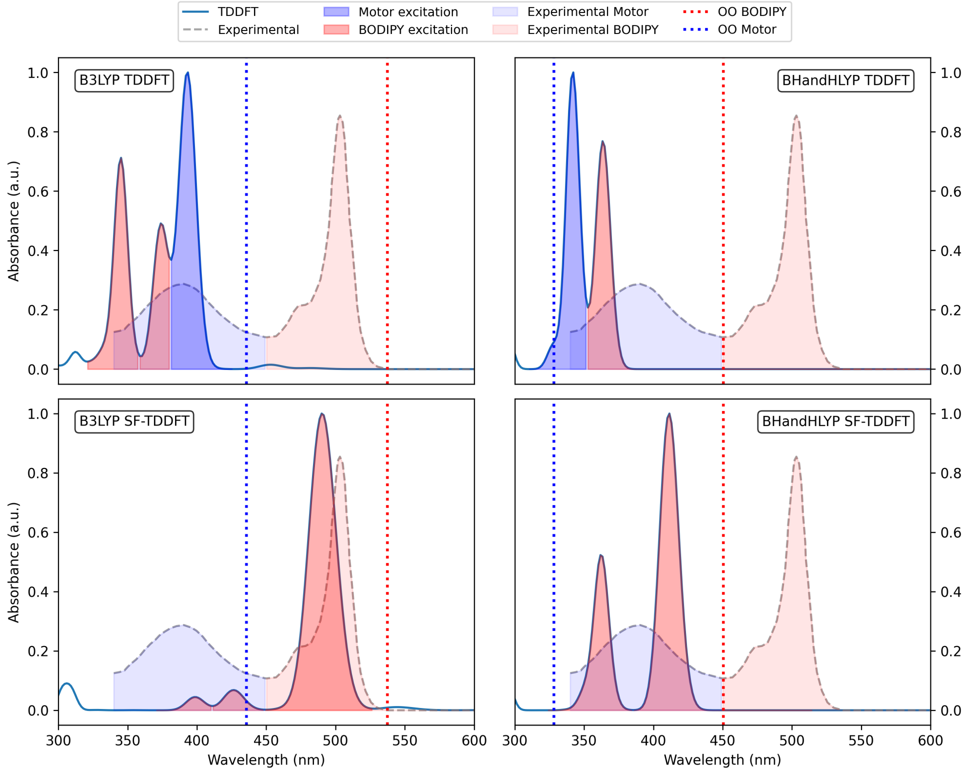

Figure 5.2. TDDFT and SF-TDDFT absorption spectrum calculations for the BODIPY/Motor molecule, wavelength of Orbital Optimized Spin-Purified energies corresponding to the lowest energy local excitations in Motor and BODIPY parts of the molecule, and the experimental absorption spectra of the molecule (experimental data from Ref. [74])

.

Given the failure of these response-based methods, the variational, time-independent DFT approach (OO-SP), discussed previously, was employed. This approach represents a significant improvement. As shown in Tables 5.1 and 5.2, the OO-SP method successfully locates both the motor and BODIPY excited states for all functionals tested.

Crucially, the OO-SP method is consistent. The calculated separation between the two peaks, derived from Table 5.1, is ∼100-120 nm for all three functionals. This is in good qualitative agreement with the experimental value of ∼110 nm, a result that outperforms the standard response methods. While the absolute peak positions remain sensitive to the choice of functional - B3LYP underestimates the energies, while BHandHLYP and CAM-B3LYP overestimate them, a known issue for BODIPY dyes [76] - the OO-SP method provides a physically sound and

Table 5.1. Calculated wavelengths (in nm) from Orbital Optimized Spin-Purified energies for the two main localized excitations, showing strong functional dependence. $\Delta\lambda$ is the shift from the experimental peaks (BODIPY ≈ 500.0 nm, Motor ≈ 390.0 nm [74]). The BODIPY transition corresponds to HOMO $\rightarrow$ LUMO and the Motor transition to HOMO-1 $\rightarrow$ LUMO+1.

Functional	λ_{BODIPY} (nm)	$\Delta\lambda_{\text{BODIPY}}$ (nm)	λ_{Motor} (nm)	$\Delta\lambda_{\text{Motor}}$ (nm)
B3LYP	537	$+37$	435	$+45$
BHandHLYP	450	-50	328	-62
CAM-B3LYP	436	-64	339	-52

Table 5.2. Calculated excitation energies (in eV) from Orbital Optimized Spin-Purified calculations. ΔE is the error relative to experimental peak energies (BODIPY ≈ 2.48 eV, Motor ≈ 3.18 eV [74]).

Functional	E_{BODIPY} (eV)	ΔE_{BODIPY} (eV)	E_{Motor} (eV)	ΔE_{Motor} (eV)
B3LYP	2.31	-0.17	2.85	-0.33
BHandHLYP	2.75	$+0.27$	3.78	$+0.60$
CAM-B3LYP	2.84	$+0.36$	3.66	$+0.49$

qualitatively correct description. This case study thus serves as a confirmation for the limitations of standard TDDFT, confirming that while TDDFT is a reliable tool for the primary motor systems in this work, its application to complex, multi-chromophoric hybrids like BODIPY/Motor is not reliable.

6 Molecular Motors: Generations and Design Principles

The development of synthetic molecular motors reflects a progressive refinement of chemical strategies for producing controlled, unidirectional motion at the nanoscale. OCA architectures pioneered by Feringa and co-workers established the blueprint: a central C=C bond connects rotor and stator fragments, and a four-step cycle of photochemical and thermal events converts photons into mechanical work of directional rotation [15, 77, 78, 79].

6.1 First Generation: Overcrowded Alkenes with Two Stereocenters

First-generation OCA motors combine two stereocenters with helical chirality around an overcrowded C=C bond [15]. Photoisomerization produces a metastable isomer which relaxes via THI to a new stable state. Two photoisomerizations and two THI steps complete a 360° rotation. Directionality arises from the asymmetry introduced by multiple stereocenters and the helical twist, which bias the system to proceed in one rotational direction rather than oscillating back and forth [80].

6.2 Second Generation: Single Stereocenter, Fjord Control, and Robust Cycling

Second-generation designs achieve unidirectionality with a single stereogenic center, simplifying the energy landscape [81, 82]. A crucial focus of this dissertation is on motors with a symmetric stator, a design choice that significantly clarifies the analysis of their rotational cycle. A complete 360° rotation is driven by two consecutive sequences, each consisting of a photochemical and a thermal step. In a general, asymmetric motor, the second sequence is chemically distinct from the first, resulting in a total of four unique steps. For the symmetric motors studied here, however, this second sequence is identical to the first. This repetition reduces the entire process to just two unique steps. This allows the kinetic performance to be fully characterized by the ground-state competition between a single forward THI step and the competing TI process [80].

As highlighted in Fig. 1.1b, steric and electronic effects localized in the narrow fjord region - the sterically congested pocket between rotor and stator near the stereocenter - play a decisive role in shaping the THI transition structure and thereby the overall rotation rate [83]. Substitution in this region provides a powerful tuning handle: replacing H by F tends to raise the THI saddle via steric/electrostatic crowding [83]. As shown in Fig. 6.1, there are a wide variety of second-generation motors, with the rotation times ranging from nanoseconds to thousands of years.

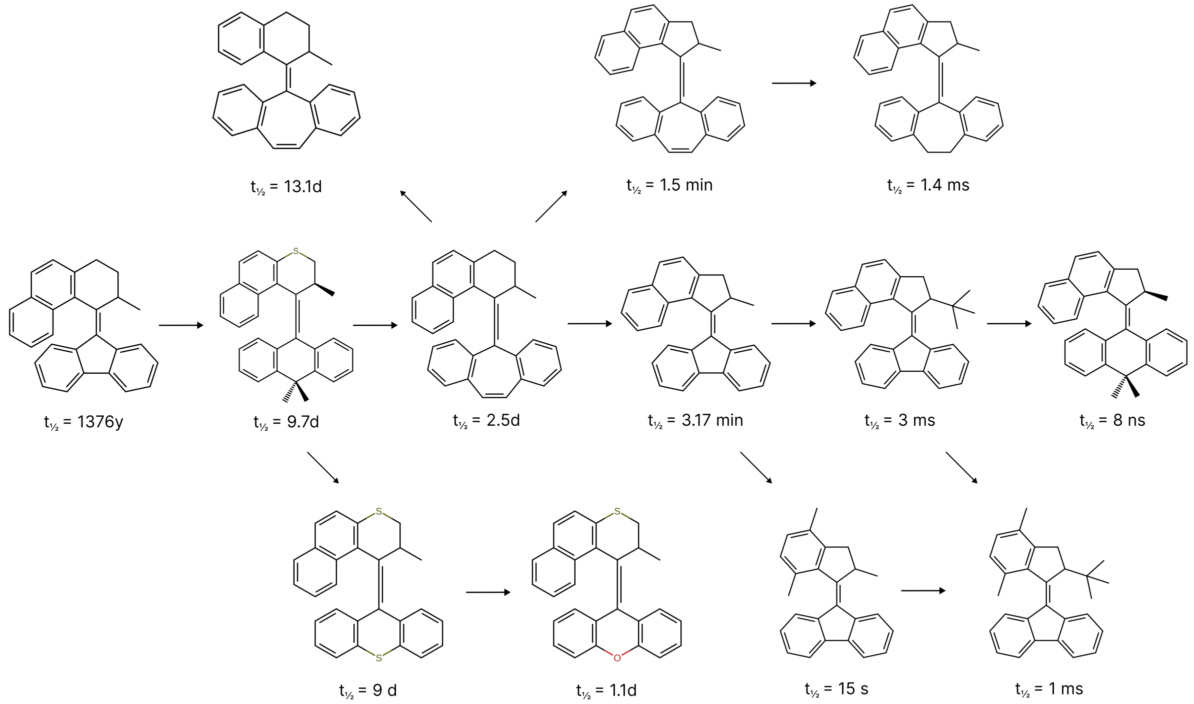

Figure 6.1. Conceptual map of second-generation overcrowded-alkene motors and their substituent-dependent relationships. The diagram highlights how modifications change the rotation speed of the molecules. Adapted from Ref. [84].

6.3 Competitive Ground-State Kinetics and Directionality

As shown in Fig. 6.2, after photoexcitation to the metastable state, relaxation on the ground-state surface proceeds through two competing first-order channels: forward and backward, to the original state, with the corresponding rates k_{THI} and k_{TI} [80, 79, 78]. The total depletion rate of the metastable population is

$$k_{\mathrm{tot}} = k_{\mathrm{THI}} + k_{\mathrm{TI}}, \qquad \tau_{1/2} = \frac{\ln 2}{k_{\mathrm{tot}}}. \tag{17}$$

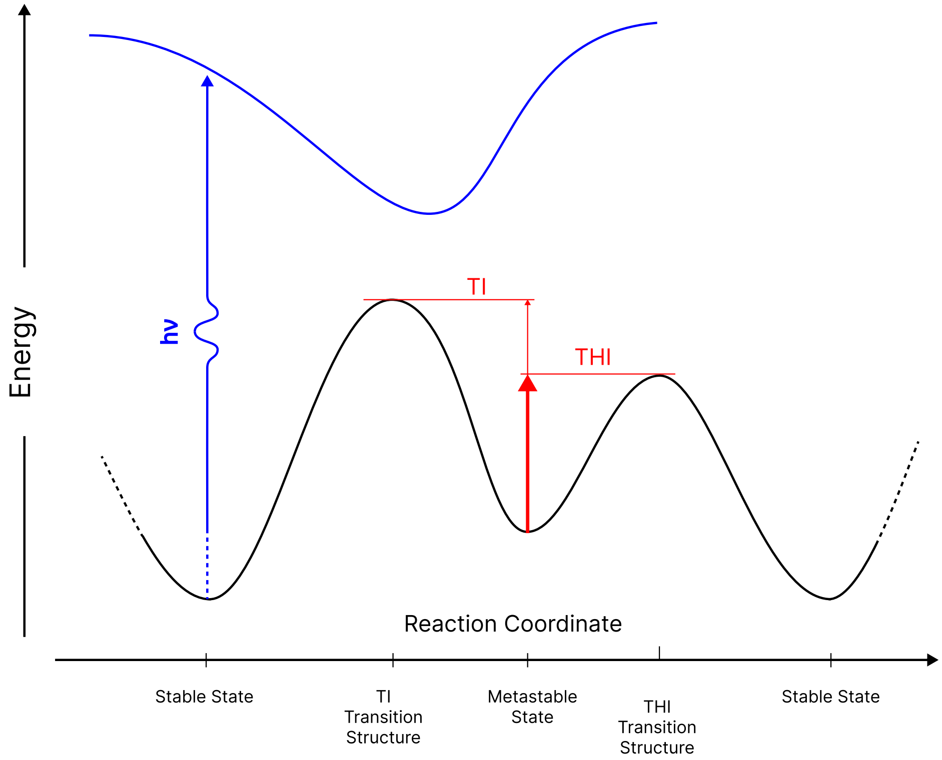

Figure 6.2. Schematic PESs for symmetric second-generation overcrowded-alkene motors. The ground-state surface (black) connects the initial stable state on the left with either the forward stable state (right) or back to the original state. Photoexcitation (blue arrow) promotes the system to the excited-state surface (blue), from which relaxation with geometric reorganization leads to the metastable minimum. Thermal activation then proceeds via one of two red-barrier pathways: THI drives forward rotation to the new stable state, while TI returns the system to the original state. For symmetric motors, the two stable states are chemically identical but rotated by 180°, ensuring unidirectional motion when the cycle is repeated. Adapted from Ref. [78].

While the potential energy surface in Fig. 6.2 provides a schematic overview, it is instructive to visualize the specific molecular geometries at these key stationary points. Figure 6.3 shows the structures for a representative motor, MPF, corresponding to the stable isomer, the higher-energy metastable isomer, and the distinct transition states for the forward THI and backward TI pathways. These structures highlight the significant conformational changes the molecule undergoes during its rotary cycle. Notably, in the transition state for thermal isomerization ($\mathrm{TS_{TI}}$), the rotor and stator fragments are nearly perpendicular, indicating a momentary breaking of the central C=C π-bond to allow for rotation around the remaining sigma bond.

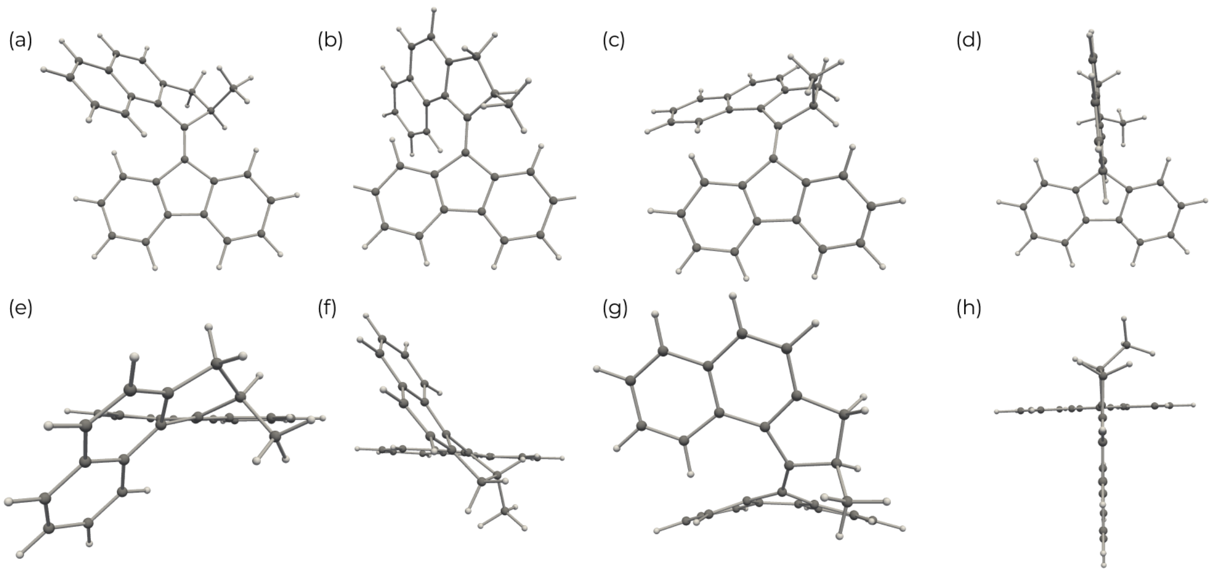

Figure 6.3. Front and top views of the optimized geometries for the key states of MPF molecule. (a,e) The stable P isomer. (b,f) The metastable M isomer. (c,g) The transition state for the forward thermal helix inversion (TS_{THI}). (d,h) The transition state for the backward thermal isomerization (TS_{TI}).

For comparison across scaffolds and substitutions, the forward-step half-life

$$t_{1/2}^{\mathrm{THI}} = \frac{\ln 2}{k_{\mathrm{THI}}}, \tag{18}$$

isolates the kinetics of the THI channel itself, independent of TI. In the symmetric motors studied in this thesis, the two stable states are equivalent and thus give rise to a single representative cycle; it is sufficient to characterize one THI and one TI barrier to capture the full dynamics. By contrast, in asymmetric scaffolds the two stable states are chemically distinct, each associated with a different absorption wavelength, and the two rotary cycles must be analyzed separately to fully describe their kinetics and photodynamics.

6.4 Beyond the Second Generation

The limitations of first- and second-generation motors, such as their reliance on high-energy UV light and a single point of chirality, have prompted the development of more advanced systems. Third-generation motors expand the design principles by moving beyond the concept of a distinct rotor-stator architecture with a single stereocenter. A major architectural shift is to incorporate two identical overcrowded alkene moieties, both of which function as rotors. In these systems, unidirectionality is enforced not by a classical stereogenic center but by a pseudo-asymmetric center located within a central bridging unit. While achiral overall, this bridge imparts a localized chiral environment that biases the rotational cycle of each rotor in the same direction [53]. This elegant design creates a system where multiple rotating elements are intrinsically synchronized.

A crucial advancement has been the development of motors that operate using lower-energy, visible light. Hemithioindigo (HTI) motors are a prominent example, featuring a chromophore with a smaller HOMO-LUMO gap that shifts its absorption into the visible spectrum. The complete operational cycle of an HTI motor has been meticulously characterized, revealing a four-step rotation through four distinct ground-state intermediates [85]. A key finding from these studies is a paradigm shift in motor design: once the thermal steps are sufficiently fast, the overall rotational frequency is not limited by the thermal barrier height but by the efficiency of the photochemical step. This highlights the critical importance of engineering excited-state dynamics to maximize the photoisomerization quantum yield.

Beyond bond isomerization, an entirely different class of molecular motors is built on the principle of rectifying random Brownian motion (which involves guiding the inherent, random thermal jiggling of molecules to produce net directional movement). These systems utilize Mechanically Interlocked Molecules (MIMs), such as rotaxanes and catenanes, where components are linked by topology rather than covalent bonds. The motion of these motors is achieved by dynamically manipulating the system's potential energy landscape. By using an external fuel to cyclically and asymmetrically lower kinetic barriers or alter binding affinities, these systems operate as Brownian ratchets, biasing random thermal fluctuations to produce net unidirectional motion [86]. This probabilistic mechanism, while generally slower than that of isomerization-based motors, offers remarkable versatility for performing complex tasks like linear pumping or templated synthesis.

7 Continuum Model for Light-Controlled Chiral Media

To bridge the gap between the single-molecule kinetics of the motor and the collective, mesoscale response of the host material, a continuum-level model is necessary [87, 88]. This approach describes how the light-driven switching of individual motors translates into observable changes in the director field of a CLC.

The state of the motor-doped CLC at any point in space $\mathbf{r}$ is described by two key quantities: the normalized director field $\mathbf{n}(\mathbf{r})$, which represents the average local orientation, and the local concentrations of the motor's stable, $\rho_{\text{stable}}(\mathbf{r})$, and metastable, $\rho_{\text{meta}}(\mathbf{r})$, isomers.

The coupling between the molecular motors and the CLC host is captured by the Frank-Oseen free energy density, which describes the energetic cost of deforming the director field from its uniform ground state [87]. In the one-constant approximation, it can be expressed as:

$$\mathscr{F} = \frac{K}{2}\left[(\nabla\cdot\mathbf{n})^2 + (\mathbf{n}\cdot\nabla\times\mathbf{n}+q)^2 + (\mathbf{n}\times\nabla\times\mathbf{n})^2\right]$$

Here, K is an effective elastic constant, and the terms represent the energetic penalties for splay, twist, and bend deformations, respectively.

The crucial link between the molecular and mesoscale is the helical wave number, q, which is inversely proportional to the CLC's pitch ($P = 2\pi/q$). In a motor-doped system, q is not a constant but a function of the local isomer concentrations:

$$q(\mathbf{r}) = q_{\text{host}} + HTP_{\text{stable}}\cdot\rho_{\text{stable}}(\mathbf{r}) + HTP_{\text{meta}}\cdot\rho_{\text{meta}}(\mathbf{r})$$

where q_{host} is the intrinsic wave number of the CLC and HTP is the helical twisting power of each motor isomer. Since the stable and metastable isomers typically have different shapes and chiralities, their HTP values differ significantly. Consequently, a light-induced change in local concentrations ($\rho_{\text{stable}} \leftrightarrow \rho_{\text{meta}}$) creates a local gradient in q, forcing the director field $\mathbf{n}$ to adopt a new, higher-energy configuration.

The system's evolution is then governed by a set of coupled partial differential equations. The director field evolves via a dissipative relaxation process, seeking to minimize the total free energy at each moment in time, as described by the Ericksen-Leslie theory [89]. Simultaneously, the concentrations of the motor isomers evolve according to a reaction-diffusion equation, which accounts for the photochemical switching driven by light intensity and the spatial diffusion of the molecules through the host. This theoretical framework establishes the mechanism by which light, acting on the nanoscale motors, can write, erase, and manipulate mesoscale topological textures in the liquid crystal, providing the foundation for understanding the phenomena explored in this dissertation.

8 Summary of Original Articles

8.1 Original Article I

8.1.1 Summary

The article *Fine Tuning of the Rotational Speed of Light-Driven, Second-Generation Molecular Motors by Fluorine Substitution* establishes and validates a predictive workflow for the ground-state thermal steps of second–generation overcrowded–alkene motors. The computational protocol combines B3LYP/6-31G(d,p) energetics, CI-NEB minimum–energy paths with energy-weighted springs, and HTST rate estimates. The calculated half-lives are benchmarked against experiment and the study dissects two targeted fluorine substitutions at the rotor stereocenter - H → F at position Y and $CH_3 \rightarrow CF_3$ at the position X (Fig. 8.1) - to tune the rate-limiting THI step [57, 59, 56, 60, 83, 90, 91, 92, 51, 93, 94, 95].

Operation follows the canonical four-step cycle of second-generation motors: photoinduced E→metastable Z, thermal inversion to stable Z, and repetition after a second photon [77, 78, 79, 15, 80]. Since productive rotation requires that the forward THI outcompetes the reverse TI, the study emphasizes accurate evaluation of barriers and prefactors for both processes. Rates are obtained via HTST [Eq. (10)] with vibrational analyses confirming the correct character of stationary points. CI-NEB paths between metastable-Z and stable-Z geometries yield converged transition structures and barrier heights under tight force criteria. Initial bands are generated by S-IDPP, providing smooth, chemically reasonable initial images that accelerate convergence [96].

The first set of results validates the methodology: calculated metastable half-lives correlate closely with experimental measurements across a diverse set of second-generation motors, including those with fluorine at the stereogenic center (Fig. 8.2a) [81, 97, 98, 83, 80, 82, 16, 18].

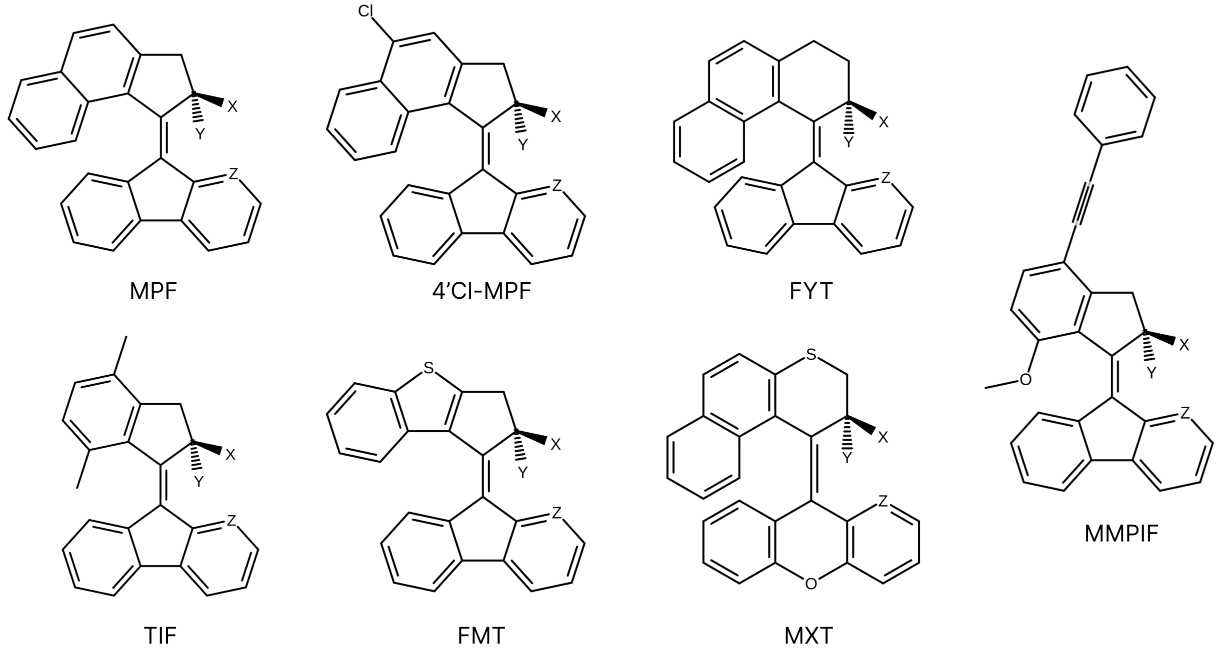

Figure 8.1. The molecular motors investigated in the present study to assess the effect of fluorine and nitrogen substitutions. The sites are labeled X, Y, and Z and they have a CH_3, H, and CH, respectively, in the base molecules, but CF_3, F, or N in the modified molecules.

With this benchmark established, the article dissects two substitutions. Replacing H by F at the stereogenic center decelerates THI, reproducing the experimental observations of Feringa and co-workers [83]. MEP profiles and aligned structures show that single fluorination predominantly raises the transition–state energy while leaving the minima largely unchanged; the steric and electrostatic crowding that limits the rotation is concentrated near the Transition State (TS) geometry. In contrast, substituting CH_3 by CF_3 at X accelerates THI by selectively destabilizing the metastable state with minimal change to the TS, thereby reducing the forward barrier. When both substitutions are introduced together, their opposing effects partially cancel, yielding intermediate half-lives and providing a practical dial for fine-tuned rate control (Fig. 8.2b). In some scaffolds - most notably CF_3-FYT and CF_3-MXT-the thermal backreaction becomes competitive or even dominant, consistent with the steric/electrostatic picture and earlier reports [83].

The structural origin of these opposing effects is further clarified by explicit overlays of pre- and post-substitution geometries aligned at the central C=C bond: $H \rightarrow F$ perturbs the TS the most (increasing rotor–stator crowding), whereas $CH_3 \rightarrow CF_3$ primarily perturbs the metastable state. Electron-density renderings highlight the increased local polarization at substituted sites, consistent with the observed crowding patterns. To make the dominant substitution effect visually explicit in path plots, the zero of energy is set at the structure with the smallest RMSD relative to the unsubstituted reference (TS for F-substituted molecules, metastable for CF_3-substituted molecules).

Spectral peaks were calculated with linear–response TDDFT (B3LYP). Across the series, substitution of CH_3 by CF_3 increases the separation between stable- and metastable-state absorption maxima (up to 26 nm in some cases), which is beneficial for selective photochemical addressing. By contrast, substitution of H by F tends to decrease this separation. In combined substitutions, the net effect generally favors an increased gap. As an additional probe, replacing the stator CH by N at position Z in two scaffolds (MPF and F-TIF) destabilizes the metastable minimum by $\sim$0.15 eV with minimal change to the TS, shortening the half-life while preserving the F and CF_3 substitution trends.

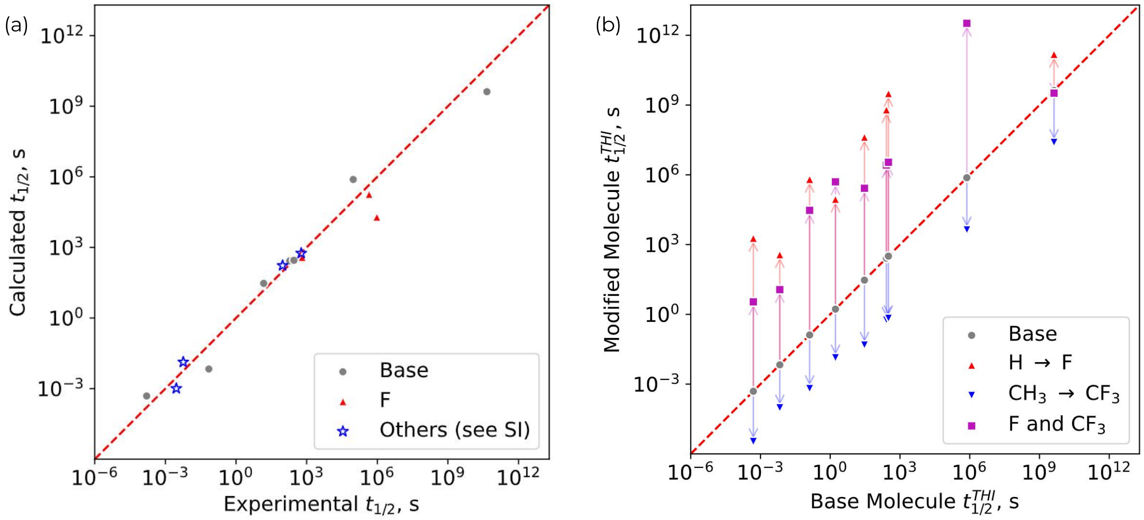

Figure 8.2. (a) Comparison of calculated and measured half-life of the metastable state of various second-generation molecular motors. Both the THI step and the backreaction are taken into account. Data corresponding to the base molecules (shown in Figure 8.1) is shown in gray, while red illustrates data for molecules where H has been replaced by F at site Y. Data on additional second-generation motors is marked with blue stars. The agreement between measured and calculated values is remarkably good, the red dashed line indicating perfect agreement. (b) Calculated half-life of the THI step and its change by substitution of CH_3 by CF_3 at site X (blue), substitution of H by F at site Y (red), and both substitutions combined (purple). The CF_3 substitution increases the rate of the THI step, whereas the F substitution decreases it, as indicated by the arrows. Taken from the original article [67].

In conclusion, the article delivers a quantitatively reliable CI-NEB/HTST protocol for predicting ground-state motor kinetics and establishes a clear design rule: substitution of H by F slows rotation by raising the THI transition state, whereas substitution of CH_3 by CF_3 accelerates by destabilizing the metastable state. Combined substitution affords monotonic and fine control of rotational speed, while often improving spectral addressability. These insights provide a chemically simple strategy for integrating second-generation motors into photonic and soft-matter platforms where tailored response times are essential [78, 99, 100, 22, 101, 102, 103].

8.1.2 Supporting Data and Analysis

The primary results of the study are the calculated half-lives, Arrhenius pre-exponential factors, and activation barriers for both THI and the competing TI pathways. The comprehensive data for the productive THI step are presented in Table 8.1.

Table 8.1. Calculated half-life ($t_{1/2}^{THI}$), pre-exponential factor (A^{THI}), and activation energy barrier (ΔE^{THI}) for the forward THI step, estimated using HTST.

Molecule	$t_{1/2}^{THI}, s$	A^{THI}, 10^{12}/s	ΔE^{THI}, eV
MPF	2.81×10^{2}	3.24	0.90
F−MPF	6.25×10^{8}	4.78	1.29
CF$_3$−MPF	5.67×10^{-1}	1.75	0.72
TIF	2.96×10^{1}	0.83	0.81
CF$_3$−TIF	4.80×10^{-2}	0.48	0.63
F−TIF	4.15×10^{7}	1.33	1.18
N−MPF	1.67×10^{0}	2.05	0.76
F, N−MPF	8.93×10^{4}	2.20	1.04
CF$_3$, N−MPF	1.35×10^{-2}	6.05	0.66
N−TIF	1.30×10^{-1}	1.20	0.68
F, N−TIF	6.37×10^{5}	0.51	1.05
CF$_3$, N−TIF	6.46×10^{-4}	2.12	0.55
FYT	4.22×10^{9}	2.03	1.32
F−FYT	1.52×10^{11}	2.24	1.41
CF$_3$−FYT	2.47×10^{7}	1.36	1.17
MMPIF	4.93×10^{-4}	0.82	0.52
F−MMPIF	1.86×10^{3}	2.74	0.94
CF$_3$−MMPIF	3.40×10^{-6}	0.59	0.38
MXT	7.50×10^{5}	4.26	1.11
F−MXT	1.82×10^{10}	2.10	1.30
CF$_3$−MXT	4.29×10^{3}	2.93	0.97
F−FMT	3.67×10^{2}	4.48	0.92
FMT	6.76×10^{-3}	2.31	0.62
CF$_3$−FMT	9.54×10^{-5}	1.32	0.49
4′Cl−MPF	2.95×10^{2}	2.97	0.90
F−4′Cl−MPF	3.14×10^{9}	1.42	1.30
CF$_3$−4′Cl−MPF	6.70×10^{-1}	1.44	0.72
CF$_3$, F−MPF	2.63×10^{6}	3.75	1.14
CF$_3$, F, N−MPF	5.00×10^{5}	2.30	1.08
CF$_3$, F−TIF	2.65×10^{5}	0.98	1.05
CF$_3$, F, N−TIF	2.95×10^{4}	0.90	0.99
CF$_3$, F−MMPIF	3.44×10^{0}	0.75	0.75
CF$_3$, F−FYT	3.26×10^{9}	1.37	1.30
CF$_3$, F−MXT	3.29×10^{12}	1.09	1.47
CF$_3$, F−FMT	1.15×10^{1}	2.20	0.81
CF$_3$, F−4′Cl−MPF	3.48×10^{6}	2.90	1.14
Ph−MPF	5.67×10^{2}	5.43	0.93
iPr−MPF	1.70×10^{2}	1.78	0.87
tBu−MPF	1.34×10^{-2}	3.88	0.65
tBu−TIF	1.01×10^{-3}	1.43	0.55

Beyond kinetics, the spectral separation between stable and metastable states is crucial for selective photochemical addressing. Table 8.2 summarizes the calculated absorption maxima (λ) and the spectral gap ($\Delta\lambda$) for all studied motors.

Table 8.2. Calculated absorption peaks for the stable and metastable isomers of the motors and the resulting spectral separation ($\Delta\lambda$).

Molecule	λ_{Stable}, nm	$\lambda_{\text{Metastable}}$, nm	$\Delta\lambda$, nm
MPF	379	410	31
F–MPF	384	414	30
CF_3–MPF	378	414	36
TIF	340	367	27
CF_3–TIF	340	375	35
F–TIF	343	375	31
N–MPF	376	406	30
F, N–MPF	388	401	14
CF_3, N–MPF	374	407	33
N–TIF	339	364	25
F, N–TIF	349	362	13
CF_3, N–TIF	336	371	36
FYT	360	396	36
F–FYT	370	408	38
CF_3–FYT	369	415	45
MMPIF	349	375	26
F–MMPIF	351	373	22
CF_3–MMPIF	345	375	30
MXT	350	414	64
F–MXT	362	443	81
CF_3–MXT	343	433	90
F–FMT	349	375	27
FMT	347	365	18
CF_3–FMT	350	368	18
$4'$Cl–MPF	388	419	32
F–$4'$Cl–MPF	393	422	29
CF_3–$4'$Cl–MPF	385	424	38
CF_3, F–MPF	385	423	39
CF_3, F, N–MPF	385	415	30
CF_3, F–TIF	346	383	37
CF_3, F, N–TIF	343	378	35
CF_3, F–MMPIF	350	380	30
CF_3, F–FYT	379	431	52
CF_3, F–MXT	352	491	139
CF_3, F–FMT	353	383	31
CF_3, F–$4'$Cl–MPF	392	430	38

To visualize the competition between the forward THI and backward TI thermal steps, the full minimum energy paths connecting the stable-E, metastable-Z, and stable-Z states were calculated for representative motors (Figure 8.3). These plots clearly show how substitution H → F raises the THI barrier, while substitution $CH_3 \rightarrow CF_3$ lowers it, without substantially altering the much larger TI barrier.

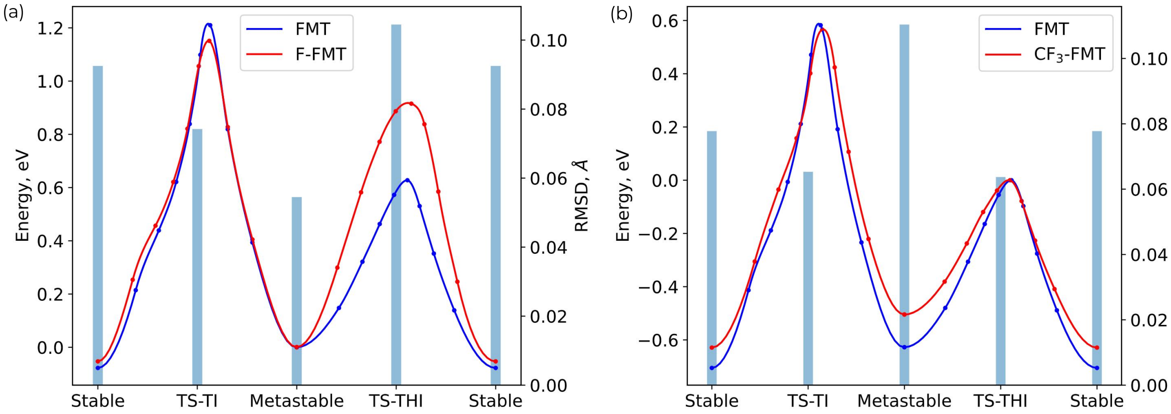

Figure 8.3. Variation of the energy along minimum energy paths connecting the stable-E, metastable-Z, and stable-Z states for base and fluorine-substituted molecules. (a) Comparison of FMT and F−FMT, showing the increase in the THI barrier upon Y-fluorination. (b) Comparison of FMT and CF_3−FMT, showing the decrease in the THI barrier upon X-fluorination.

The structural origin of these kinetic effects was investigated by analyzing the shortest distance between the stator (at site Z) and the rotor (at sites X or Y) along the reaction path (Figure 8.4). The analysis shows that H→F substitution primarily increases steric hindrance at the TS, raising its energy. In contrast, $CH_3 \rightarrow CF_3$ substitution mainly increases crowding in the metastable state, destabilizing it and thereby lowering the effective THI barrier.

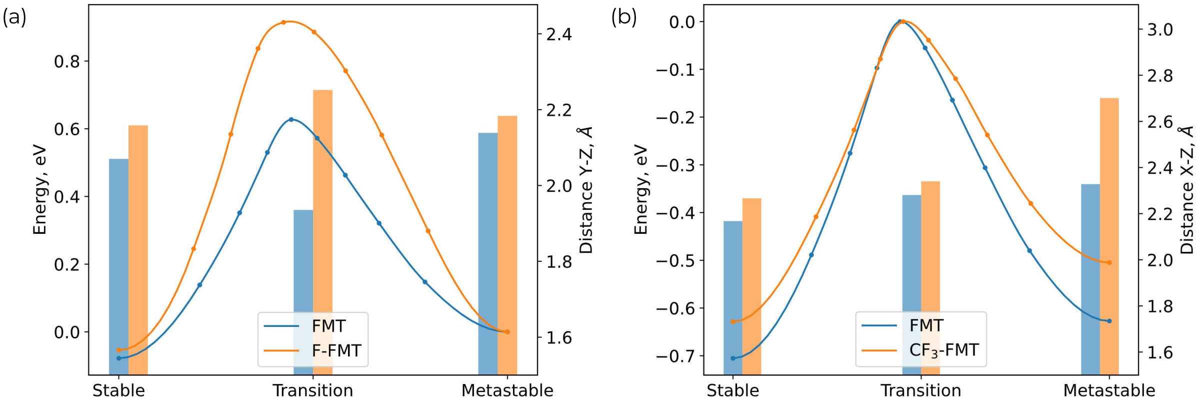

Figure 8.4. Shortest distances between the H atom at the Z site of the stator and the nearest atom at the rotor's X or Y site for the stable, transition, and metastable structures of FMT and its fluorinated analogues. The corresponding minimum energy path is also shown. (a) Effect of H→F substitution at site Y. (b) Effect of $CH_3 \rightarrow CF_3$ substitution at site X.

For a detailed quantitative analysis, the changes in relative energies and key interatomic distances upon fluorination are compiled in Tables 8.3 and 8.4. Finally, the experimental data used to benchmark the calculations are provided in Table 8.5.

Table 8.3. Detailed analysis of the effect of replacing H with F at site Y. ΔE denotes the energy difference (in eV) between the fluorinated and parent motor. Δd denotes the difference in the shortest Z-Y interatomic distance (in Å).

Pair	$\Delta E_{\text{Stable-TS}}$	$\Delta E_{\text{Stable-Metastable}}$	$\Delta E_{\text{Metastable-TS}}$	d_{Z-Y} Stable	Δd_{Z-Y} Stable	d_{Z-Y} TS	Δd_{Z-Y} TS	d_{Z-Y} Metastable	Δd_{Z-Y} Metastable
(MPF,F−MPF)	0.33	-0.06	0.39	2.08	0.10	1.87	0.32	2.30	-0.06
(TIF,F−TIF)	0.33	-0.05	0.38	2.11	0.09	1.87	0.35	2.38	-0.11
(FYT,F−FYT)	-0.01	-0.10	0.10	1.96	0.14	1.95	0.23	2.02	0.08
(MMPIF,F−MMPIF)	0.37	-0.05	0.42	2.07	0.09	1.90	0.07	2.20	0.00
(MXT,F−MXT)	0.05	-0.14	0.19	2.36	0.41	2.08	-0.11	1.94	-0.03
(FMT,F−FMT)	0.28	-0.02	0.30	2.07	0.09	1.94	0.32	2.14	0.04
(4′Cl−MPF,F−4′Cl−MPF)	0.33	-0.06	0.40	2.08	0.10	1.87	0.13	2.30	-0.05
(N−MPF,F, N−MPF)	0.29	0.01	0.28	2.42	0.36	2.02	0.53	2.77	0.68
(N−TIF,F, N−TIF)	0.38	0.01	0.38	2.46	0.34	2.00	0.50	3.02	0.42

Table 8.4. Detailed analysis of the effect of replacing CH_3 with CF_3 at site X. ΔE denotes the energy difference (in eV) between the substituted and parent motor. Δd denotes the difference in the shortest Z-X interatomic distance (in Å).

Pair	$\Delta E_{\text{Stable-TS}}$	$\Delta E_{\text{Stable-Metastable}}$	$\Delta E_{\text{Metastable-TS}}$	d_{Z-X} Stable	Δd_{Z-X} Stable	d_{Z-X} TS	Δd_{Z-X} TS	d_{Z-X} Metastable	Δd_{Z-X} Metastable
(MPF,CF_3−MPF)	-0.07	0.10	-0.18	2.18	0.04	2.41	0.04	2.27	0.54
(TIF,CF_3−TIF)	-0.06	0.12	-0.18	2.19	0.03	2.38	0.03	2.25	0.55
(FYT,CF_3−FYT)	0.04	0.18	-0.14	2.25	0.09	4.19	0.01	2.41	0.33
(MMPIF,CF_3−MMPIF)	-0.06	0.08	-0.14	2.19	0.05	2.28	0.11	2.31	0.41
(MXT,CF_3−MXT)	0.12	0.27	-0.14	2.23	0.03	3.00	-0.50	2.06	0.12
(FMT,CF_3−FMT)	-0.08	0.05	-0.12	2.17	0.10	2.28	0.06	2.33	0.37
(4′Cl−MPF,CF_3−4′Cl−MPF)	-0.07	0.10	-0.18	2.18	0.03	2.42	0.03	2.27	0.56
(N−MPF,CF_3, N−MPF)	-0.10	-0.00	-0.10	2.69	0.27	3.91	-0.12	2.35	0.60
(N−TIF,CF_3, N−TIF)	-0.10	0.03	-0.12	2.72	0.26	3.88	-0.20	2.30	0.59

Table 8.5. Full name and abbreviation used here for the various molecules as well as the experimentally measured half-life used in the comparison with the calculated results in Figure 8.2.

Acronym	**Full Name**	$t_{1/2}, s$
MPF [81]	9-(2-Methyl-2,3-dihydro-1H-cyclopenta[a]naphthalen -1-ylidene)-9H-fluorene	1.90×10^{2}
F-MPF [83]	9-{4-Fluoro-4-methyltricyclo[7.4.0.02,6]trideca -1(13),2(6),7,9,11-pentaen-3-ylidene}fluorene	9.59×10^{5}
TIF [97]	9-(2,4,7-Trimethyl-2,3-dihydro-1H-inden-1-ylidene)-9H-fluorene	1.50×10^{1}
F-TIF [83]	9-(2-Fluoro-2,4,7-trimethyl-1-indanylidene)fluorene	4.49×10^{5}
FYT [80]	(3R)-4-(9H-Fluoren-9-ylidene)-3-methyl-1,2,3,4-tetrahydrophenanthrene	4.52×10^{10}
MMPIF [82]	9-[7-Methoxy-2-methyl-4-(2-phenylethynyl) -1-indanylidene]fluorene	1.60×10^{-4}
MXT [104]	3-Methyl-4-(9H-xanthen-9-ylidene)-3,4-dihydro-2H-1-thiaphenanthrene	9.50×10^{4}
$4'$Cl−MPF [98]	9-(2-Methyl-2,3-dihydro-1H-cyclopenta[a]naphthalen -1-ylidene)-9H-fluorene	2.88×10^{2}
FMT [77]	3-(9-Fluorenylidene)-4-methyl-7-thiatricyclo[6.4.0.02,6] dodeca-1(8),2(6),9,11-tetraene	7.00×10^{-2}
F-FMT [83]	3-(9-Fluorenylidene)-4-fluoro-4-methyl-7-thiatricyclo[6.4.0.02,6] dodeca-1(8),2(6),9,11-tetraene	6.42×10^{2}
Ph-MPF [81]	9-{4-Phenyltricyclo[7.4.0.02,6] trideca-1(13),2(6),7,9,11-pentaen-3-ylidene}fluorene	5.87×10^{2}
iPr-MPF [81]	9-{4-Isopropyltricyclo[7.4.0.02,6] trideca-1(13),2(6),7,9,11-pentaen-3-ylidene} fluorene	9.47×10^{1}
tBu-MPF [81]	9-{4-tert-Butyltricyclo[7.4.0.02,6] trideca-1(13),2(6),7,9,11-pentaen-3-ylidene} fluorene	5.73×10^{-3}
tBu-TIF [18]	9-(2-tert-Butyl-4,7-dimethyl-1-indanylidene) fluorene	2.90×10^{-3}

8.2 Original Article II

8.2.1 Summary

The article *Tuning Molecular Motors with Tert-Butyl and Fluorinated Tert-Butyl Groups* investigates whether steric and electronic modifications at the rotor stereogenic center can systematically accelerate the rate-limiting THI in second-generation molecular motors. Building on earlier work where substitution of CH_3 by CF_3 was shown to accelerate rotation by destabilizing the metastable state [67], this study extends the strategy to the even bulkier *tert*-butyl (tBu) and fully fluorinated *tert*-butyl (FtBu) groups.

The computational framework combines density functional theory (B3LYP/6-31G(d,p)) with CI-NEB calculations to map MEPs for the competing THI and TI steps [57, 59, 56, 60, 61]. Rate constants are then estimated using HTST [54, 55].

Two clear kinetic trends emerge across all scaffolds. First, replacing CH_3 with tBu consistently accelerates the THI, in agreement with prior experimental reports [81, 105]. Second, the further substitution of tBu with FtBu produces an additional, significant acceleration in every case (Fig. 8.5a). The MEP analysis reveals that this speedup originates from steric effects: rotor–stator repulsion is most pronounced in the metastable state. Consequently, the bulky tBu and FtBu groups selectively raise the energy of this state relative to the transition structure, lowering the activation barrier for forward rotation (Fig. 8.5b).

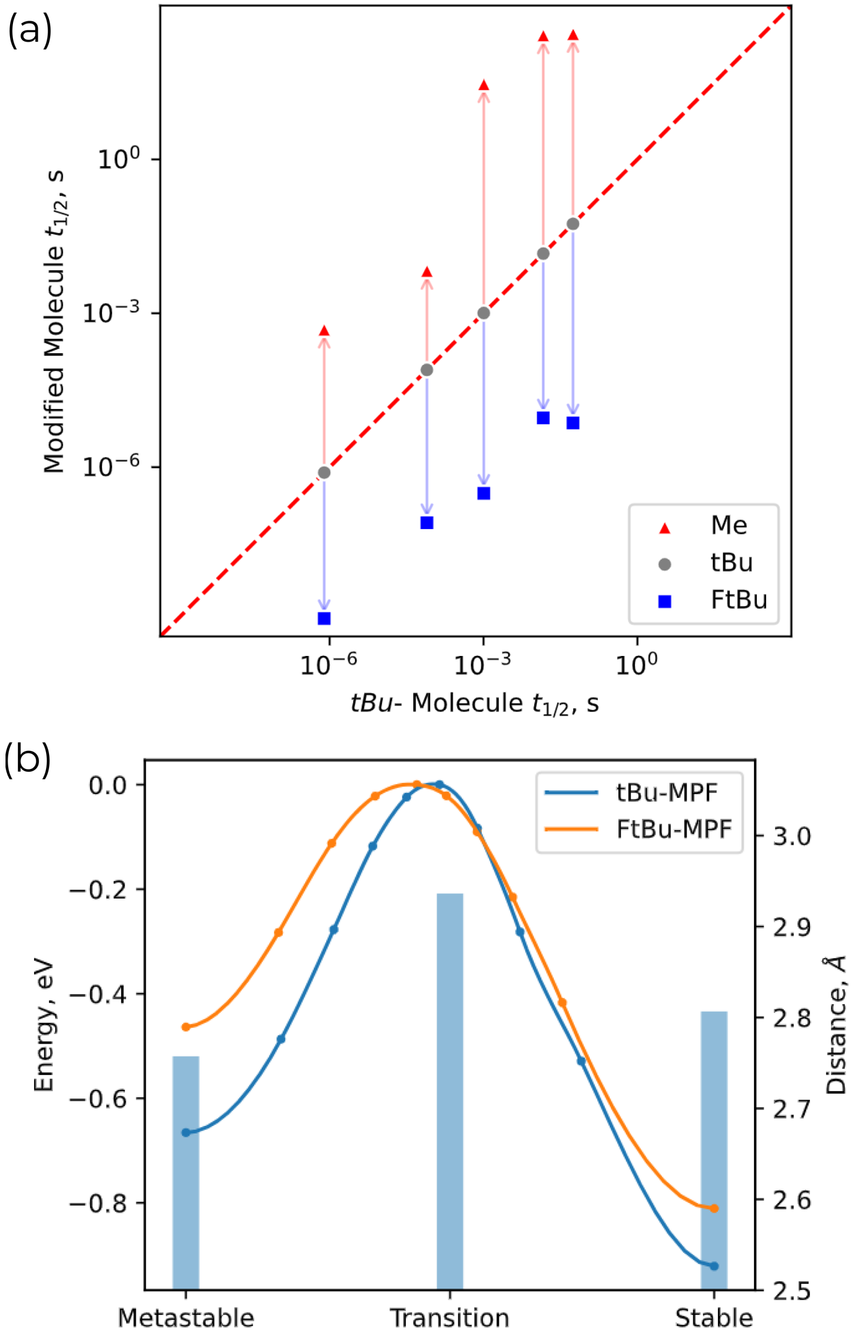

Figure 8.5. (a) Calculated half-lives of the molecular motors. The FtBu motor (blue) relaxes faster than the tBu motor (grey), which is faster than the original methyl-substituted motor. (b) Representative MEPs and rotor–stator proximity metric comparing tBu and FtBu, showing selective metastable destabilization upon full fluorination.

The substitutions also yield favorable spectroscopic shifts. TDDFT calculations show that replacing CH_3 with tBu, and subsequently tBu with FtBu, systematically enlarges the wavelength separation between the absorption maxima of the stable and metastable isomers (Fig. 8.6). This increased spectral gap is advantageous for practical applications, as it enhances selective photo-addressability and minimizes undesired backward photoreactions.

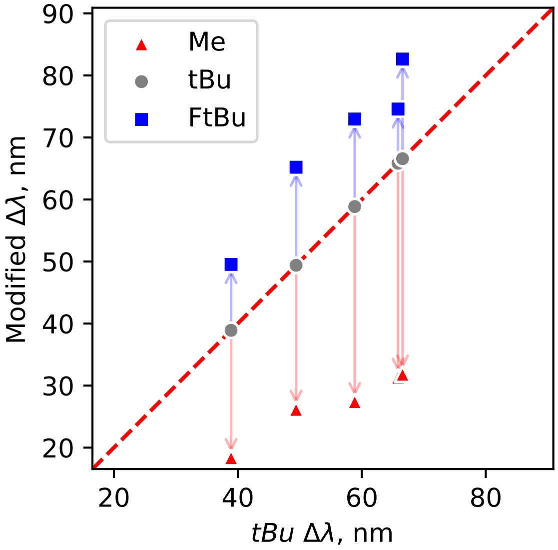

Figure 8.6. TDDFT-calculated spectral gaps between stable and metastable absorption maxima for Me, tBu, and FtBu. Me$\rightarrow$tBu enlarges the gap by $\sim$29 nm; FtBu adds another $\sim$13 nm.

The article establishes that substitution with tBu and FtBu groups is a robust strategy for accelerating second-generation molecular motors. The acceleration is driven by targeted steric destabilization of the metastable state, and it is accompanied by beneficial spectroscopic changes that improve optical control. These findings provide a practical design rule for tuning motor speeds for specific applications in responsive materials and molecular machines [99, 100, 22, 101, 103, 102, 23].

8.2.2 Supporting Information

Molecule	λ_{stable}, nm	λ_{meta}, nm	k^{THI}, s^{-1}	k^{TI}, s^{-1}	$t_{1/2}$, s	$t_{1/2}^{Exp}$, s
MPF	379	410	2.60×10^{-3}	8.34×10^{-4}	2.02×10^{2}	1.90×10^{2} [81]
tBu-MPF	371	437	4.75×10^{1}	7.99×10^{-3}	1.46×10^{-2}	5.73×10^{-3} [81]
FtBu-MPF	368	442	7.59×10^{4}	6.26×10^{4}	5.00×10^{-6}	-
TIF	340	367	2.32×10^{-2}	7.93×10^{-7}	2.99×10^{1}	1.50×10^{1} [97]
tBu-TIF	336	395	6.85×10^{2}	2.61×10^{-3}	1.01×10^{-3}	2.90×10^{-3} [18]
FtBu-TIF	332	405	2.24×10^{6}	1.09×10^{-1}	3.09×10^{-7}	-
4′Cl-MPF	388	419	2.44×10^{-3}	1.84×10^{-3}	1.62×10^{2}	2.88×10^{2} [98]
tBu-4′Cl-MPF	380	446	1.25×10^{1}	1.68×10^{-2}	5.54×10^{-2}	-
FtBu-4′Cl-MPF	372	454	9.52×10^{4}	4.39×10^{-1}	7.28×10^{-6}	-
MMPIF	349	389	1.42×10^{3}	8.78×10^{-6}	4.88×10^{-4}	1.60×10^{-4} [82]
tBu-MMPIF	345	394	8.83×10^{5}	5.54×10^{-5}	7.85×10^{-7}	-
FtBu-MMPIF	334	399	6.22×10^{8}	5.21×10^{-4}	1.11×10^{-9}	-
FMT	347	365	1.02×10^{2}	1.12×10^{-6}	6.80×10^{-3}	7.00×10^{-2} [77]
tBu-FMT	345	384	8.80×10^{3}	3.04×10^{-6}	7.88×10^{-5}	-
FtBu-FMT	347	397	8.39×10^{6}	2.18×10^{-3}	8.26×10^{-8}	-

Table 8.6. Absorption wavelengths for the stable and metastable isomers, calculated forward THI and backward TI thermal rate constants, and the resulting total half-life ($t_{1/2}$) of the metastable state. Experimental half-lives are included for comparison where available.

8.3 Original Article III

8.3.1 Summary

The article *The Effect of Chlorine Substitution on Rotational Speed and Light Absorption of Second Generation Molecular Motors* investigates targeted chlorination at the rotor's stereogenic center, revealing it to be a dichotomous design tool capable of either accelerating rotation or completely redesigning the molecule's function. The study uses a standard computational workflow combining density functional theory, CI-NEB paths, and HTST.

The primary finding is that the two types of chlorination yield fundamentally different outcomes. First, substituting a methyl group with a trichloromethyl group (CCl_3) acts as a powerful accelerator. It consistently lowers the barrier for the productive THI step, resulting in motors that are even faster than trifluoromethyl analogues.

In contrast, replacing the hydrogen at the same stereogenic center by chlorine (H→Cl) triggers a qualitative redesign of the ground-state energy landscape. While this substitution may be synthetically challenging (and is therefore treated primarily as a mechanistic probe in this work), it provides a clear demonstration of how sensitively the motor profile depends on substitution at the stereogenic center. The calculated MEP in Figure 8.7 provide a clear picture of this change. While the CCl_3 systems (red curves) maintain the standard motor energy profile, the Cl systems (green curves) exhibit an inversion of isomer stability, . . . where the energetic ordering of the P/M geometries inverts (the M geometry becomes the lower-energy minimum) and thermal relaxation becomes dominated by TI rather than productive forward THI.

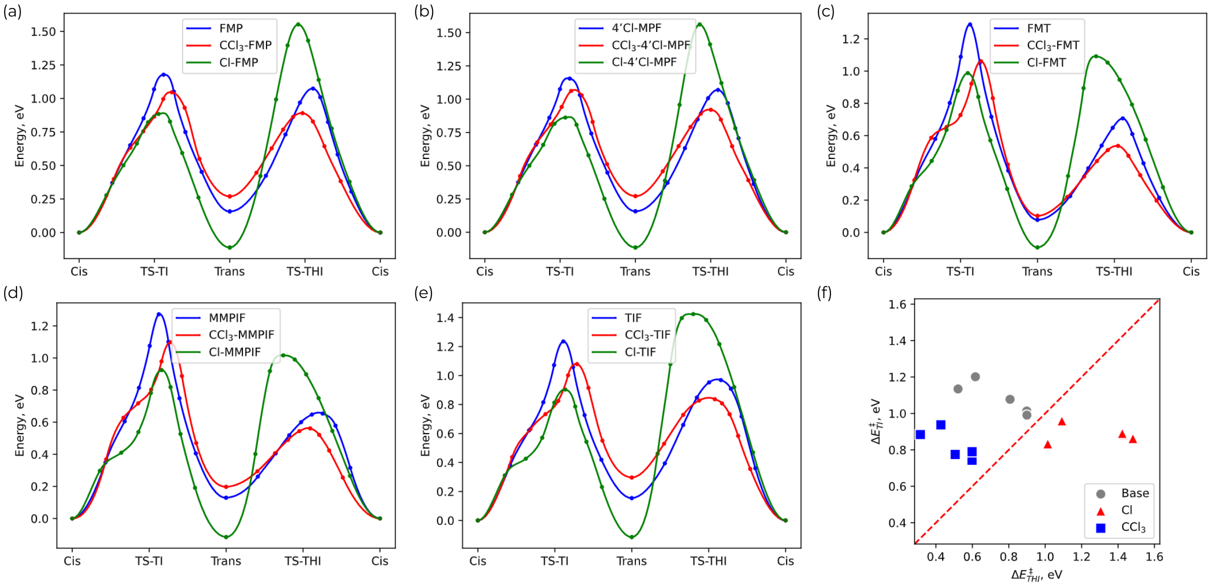

Figure 8.7. Calculated Minimum Energy Paths illustrating the dichotomous effect of chlorination. The paths for the parent (Me, blue) and CCl_3-substituted (red) systems show a typical motor profile with a metastable M state. In contrast, the paths for the Cl-substituted systems (green) reveal an inversion of stability, where the M state becomes the new ground state, fundamentally altering the molecule's function. Panel (f) directly compares the activation barriers from the respective metastable states, highlighting the kinetic dominance of TI for the Cl systems.

The kinetic consequences of this divergence are quantified in Figure 8.8. The calculated half-lives confirm that CCl_3 substitution produces the fastest motors in the series. CCl_3 substitution also increases the spectral separation between the stable and metastable isomers.

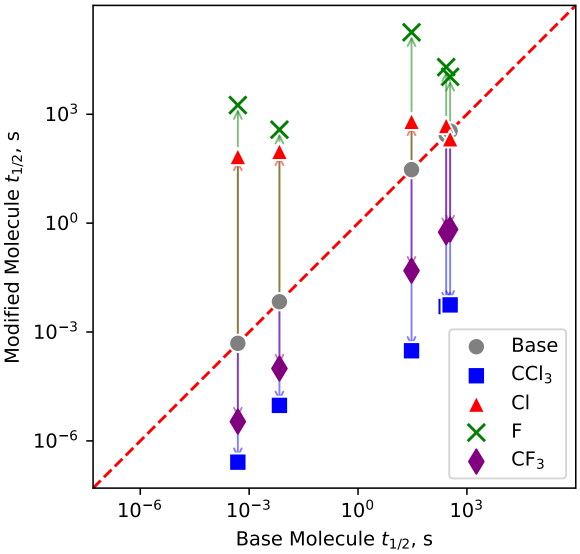

Figure 8.8. Calculated half-lives of the metastable state. The CCl_3 substitution yields the fastest rotating motor. Data for F and CF_3 substitutions are included for comparison.

In conclusion, the study establishes chlorination as a powerful and versatile tool for functional molecular design. CCl_3 substitution is a robust strategy for creating exceptionally fast rotary motors, while single Cl substitution exposes a new behavior of inverting the relative isomer stability, fundamentally altering the molecule's energy landscape.

8.3.2 Supporting Information

Molecule	λ_P	λ_M	k^{THI}	k^{TI}
MPF	379	410	2.58×10^{-3}	8.23×10^{-4}
CCl_3-MPF	381	436	1.38×10^{2}	7.07×10^{0}
4′Cl-MPF	388	420	2.01×10^{-3}	1.74×10^{-3}
CCl_3-4′Cl-MPF	386	443	1.24×10^{2}	5.38×10^{-2}
FMT	347	365	1.01×10^{2}	1.13×10^{-6}
CCl_3-FMT	362	393	7.28×10^{4}	5.85×10^{-3}
MMPIF	349	389	1.42×10^{3}	8.78×10^{-6}
CCl_3-MMPIF	347	426	2.67×10^{6}	3.68×10^{-2}
TIF	340	367	2.32×10^{-2}	7.93×10^{-7}
CCl_3-TIF	346	398	2.28×10^{3}	3.53×10^{0}
Cl-MPF	399	416	1.18×10^{-12}	5.57×10^{-1}
Cl-4′Cl-MPF	408	422	3.55×10^{-13}	9.21×10^{-1}
Cl-FMT	361	385	1.73×10^{-6}	7.28×10^{-3}
Cl-MMPIF	365	376	3.76×10^{-5}	2.94×10^{-2}
Cl-TIF	359	378	1.24×10^{-12}	1.09×10^{-3}

Table 8.7. Calculated spectroscopic and kinetic data for chlorinated motors. Absorption wavelengths for the P and M geometries are provided, along with the rate constants for the forward (THI) and backward (TI) thermal reactions at 298.15 K. All rate constants refer to transitions out of the metastable geometry: from M for the unsubstituted and CCl_3 cases, and from P for the H→Cl cases.

8.4 Original Article IV

8.4.1 Summary

The article *Pair interaction of localized topological structures in confined chiral media* shifts the focus from the molecular motor to the environment it is designed to operate within: a confined CLC. Such chiral media are known to host a variety of localized, particle-like topological solitons, including skyrmion tubes, torons, and leeches [106, 107, 108]. Understanding the interaction forces between these structures is critical for predicting how they can be manipulated by an embedded actuator. This study employs a lattice-based model to numerically calculate the effective pairwise interaction potentials for these solitons within a CLC cell with homeotropic anchoring.

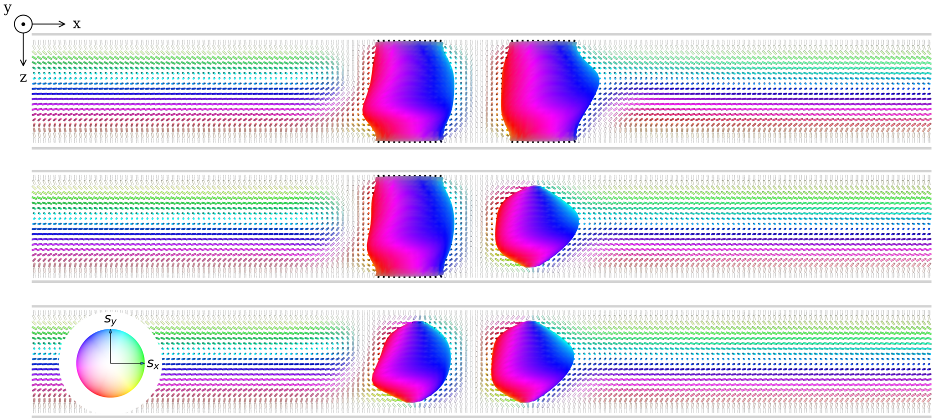

Figure 8.9. Calculated equilibrium configurations for two-soliton structures in a chiral medium. From top to bottom: a pair of skyrmion tubes, a skyrmion-toron pair, and a pair of torons. These structures correspond to the minima of their respective interaction potentials.

The analysis reveals that skyrmions and torons exhibit largely isotropic, attractive interactions at long distances, which leads to the formation of stable, ordered clusters. Figure 8.9 visualizes the calculated equilibrium configurations for pairs of these solitons, which correspond to the minima of their respective interaction potentials. For clusters of three solitons, both triangular and linear chain configurations were found to be stable, as shown for skyrmions in Figure 8.10. In contrast, the interaction between leech structures - which are attached to one of the confining surfaces - is found to be highly anisotropic, with the potential becoming repulsive at long distances for certain orientations. All interactions feature a short-range repulsive part that defines a stable equilibrium separation. These findings provide a fundamental map of the forces governing the mesoscale organization of CLCs, establishing a physical framework for the future design of motor-driven reconfigurable photonic materials.

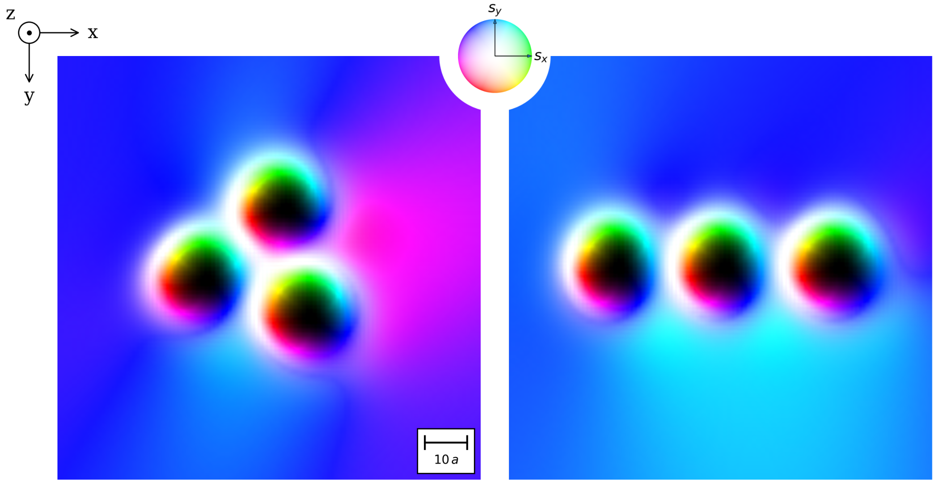

Figure 8.10. Equilibrium configurations for three-skyrmion clusters, forming a stable triangular structure (left) and a linear chain (right). These ordered structures arise from the attractive pairwise interaction potentials.

8.4.2 Supporting Information

Table 8.8. Binding energies of two-soliton and three-soliton structures. Percentages in brackets indicate the relative difference between the three-soliton binding energy and the sum of pair interaction energies.

	Two-soliton structure	Triangular structure	Linear chain
Skyrmion	-11.46	-32.33 (6%)	-22.46 (2%)
Toron	-7.14	-17.34 (19%)	-14.28 (<1%)

9 Conclusions and Outlook

This dissertation applies established electronic-structure tools to quantify and tune photophysical properties and the ground-state rotational kinetics of light-driven second-generation molecular motors. Their absorption spectra are characterized using TDDFT. The limitations of standard TDDFT for complex multi-chromophoric systems are also probed, which serves to validate a time-independent orbital-optimized approach for challenging cases featuring coupled chromophores and spatially-segregated excitations. MEPs are obtained with NEB and rate constants are estimated from harmonic transition state theory. The goal has been to extract simple, transferable rules that map targeted chemical substitution to changes in rotation speed and optical addressability.

Two robust substitution patterns emerge across representative overcrowded-alkene scaffolds. First, replacing the methyl group at the stereogenic center by bulkier or more electronegative substituents - such as CF_3, CCl_3, *tert*-butyl, or fully fluorinated *tert*-butyl - consistently increases the rotation speed. These substitutions often also enlarge the spectral separation between stable and metastable states, improving selective photoaddressability. Second, replacing hydrogen at the stereogenic center by fluorine slows the rotation and tends to narrow the spectral gap. In a more profound change, substitution by a single chlorine atom was found to invert the relative stability of the isomers, fundamentally redesigning the molecule's function.

The three papers underpinning these conclusions address complementary parts of this picture. Paper I examines fluorine substitution and establishes the computational protocol against experiment. Paper II shows that *tert*-butyl and, especially, its fully fluorinated analogue provide additional acceleration while preserving ground-state geometries and offering beneficial spectral shifts. Paper III analyzes chlorination at the stereogenic center, revealing a stark dichotomy: it demonstrates that CCl_3 substitution is a powerful accelerator, whereas single-chloro substitution completely redesigns the molecule's energy landscape, making the state that was metastable for other studied molecules stable.

Complementing the focus on the molecular actuator, Paper IV shifts the perspective to the chiral medium. This work provides a fundamental understanding of the mesoscale environment the motors are designed to control. By mapping the pairwise interaction potentials of topological solitons within a confined cholesteric liquid crystal, it reveals the forces governing their organization. The study establishes that skyrmions and torons exhibit attractive, largely isotropic interactions, leading to the formation of ordered clusters, whereas leech structures show highly anisotropic and even repulsive behavior. These findings are valuable, as they provide the physical framework for predicting how a local perturbation from a molecular motor can propagate to create, annihilate, or transport the very textures essential for device function.

These results provide straightforward guidelines for setting motor half-lives and spectral properties by design. While the calculations emphasize relative barrier changes under gas-phase conditions and harmonic approximations, the observed trends are systematic across scaffolds and substitution patterns. Incorporating explicit environments will be a natural next step toward quantitative predictions in condensed phases.

Beyond motor–motor comparisons, the guidelines are intended to support integration into functional media. In particular, tuning rotation timescales and spectral separation is directly relevant for motor-doped cholesteric liquid crystals, where light-controlled actuation, reconfigurable photonics, and transport of chiral textures rely on the interplay between molecular kinetics and mesoscale response. The same logic can be applied to other soft-matter hosts in which controlled response times and optical addressability are essential.

In summary, combining targeted syntheses (e.g., CF_3, CCl_3, *t*Bu, fully fluorinated *t*Bu at the stereogenic center; cautious use of F on hydrogen sites) with measurements of half-lives and spectra in relevant hosts will further calibrate and expand these rules. Beyond single-site modifications, combining different accelerator groups (such as CF_3) with other halogen substitutions offers a route to intermediate kinetics and additional fine-tuning of motor behavior. Adding explicit solvent or host models and computing free-energy barriers, alongside improved descriptions of photoisomerization, will refine the link between chemical substitution and device-level performance. Together, these advances will tighten the connection between quantum-chemical design and light-responsive soft-matter function.

References

[1] Richard Feynman. “There’s Plenty of Room at the Bottom.” *Feynman And Computation*. 2002.

[2] Wolfgang Göpel. “Nanosystems: Molecular Machinery, Manufacturing and Computation. By K. Eric Drexler, J. Wiley and Sons, Chichester, UK 1992, 556 Pp.” *Advanced Materials* 5 (1993), pp. 865–866.

[3] George M. Whitesides and Bartosz Grzybowski. “Self-Assembly at All Scales.” *Science* 295 (2002), pp. 2418–2421.

[4] Nadrian C. Seeman and Philip S. Lukeman. “Nucleic Acid Nanostructures: Bottom-Up Control of Geometry on the Nanoscale.” *Reports on progress in physics. Physical Society (Great Britain)* 68 (2005), pp. 237–270.

[5] Marek Grzelczak et al. “Directed Self-Assembly of Nanoparticles.” *ACS Nano* 4 (2010), pp. 3591–3605.

[6] Vincenzo Balzani, Alberto Credi, and Margherita Venturi. “Light Powered Molecular Machines.” *Chemical Society Reviews* 38 (2009), pp. 1542–1550.

[7] Vincenzo Balzani, Margherita Venturi, and Alberto Credi. *Molecular Devices and Machines: Concepts and Perspectives for the Nanoworld*. 2008.

[8] Wesley R Browne and Ben L Feringa. “Making Molecular Machines Work.” *Nanoscience and Technology: A Collection of Reviews from Nature Journals* (2010), pp. 79–89.

[9] Anouk S. Lubbe et al. “Designing Dynamic Functional Molecular Systems.” *Tetrahedron* 73 (2017), pp. 4837–4848.

[10] Salma Kassem et al. “Artificial Molecular Motors.” *Chemical Society Reviews* 46 (2017), pp. 2592–2621.

[11] Rainer Herges. “Molecular Assemblers: Molecular Machines Performing Chemical Synthesis.” *Chemical Science* 11 (2020), pp. 9048–9055.

[12] Ben L. Feringa. “The Art of Building Small: From Molecular Switches to Motors (Nobel Lecture).” *Angewandte Chemie International Edition* 56 (2017), pp. 11060–11078.

[13] Jean Pierre Sauvage and Michael Ward. “A Bis(Terpyridine)Ruthenium(II) Catenate.” *Inorganic Chemistry* 30 (1991), pp. 3869–3874.

[14] Peter R. Ashton et al. “The Template-Directed Synthesis of a [2]Rotaxane.” *Tetrahedron Letters* 32 (1991), pp. 6235–6238.

[15] Nagatoshi Koumura et al. “Light-Driven Monodirectional Molecular Rotor.” *Nature* 401 (1999), pp. 152–155.

[16] Ben L. Feringa. “In Control of Motion: From Molecular Switches to Molecular Motors.” *Accounts of Chemical Research* 34 (2001), pp. 504–513.

[17] Jos C. M. Kistemaker et al. “Unidirectional Rotary Motion in Achiral Molecular Motors.” *Nature Chemistry* 7 (2015), pp. 890–896.

[18] Jurica Bauer et al. “Tuning the Rotation Rate of Light-Driven Molecular Motors.” *The Journal of Organic Chemistry* 79 (2014), pp. 4446–4455.

[19] Sander J. Wezenberg, Kuang-Yen Chen, and Ben L. Feringa. “Visible-Light-Driven Photoisomerization and Increased Rotation Speed of a Molecular Motor Acting as a Ligand in a Ruthenium(II) Complex.” *Angewandte Chemie International Edition* 54 (2015), pp. 11457–11461.

[20] Yanping Deng et al. “Photo-Responsive Functional Materials Based on Light-Driven Molecular Motors.” *Light: Science and Applications* 13 (2024), p. 63.

[21] Qi Zhang et al. “Bottom-Up: Can Supramolecular Tools Deliver Responsiveness from Molecular Motors to Macroscopic Materials?” *Matter* 3 (2020), pp. 355–370.

[22] Jiaxin Hou et al. “Photo-Responsive Helical Motion by Light-Driven Molecular Motors in a Liquid-Crystal Network.” *Angewandte Chemie International Edition* 60 (2021), pp. 8251–8257.

[23] Tetiana Orlova et al. “Revolving Supramolecular Chiral Structures Powered by Light in Nanomotor-Doped Liquid Crystals.” *Nature Nanotechnology* 13 (2018), pp. 304–308.

[24] Nicolas Brouckaert et al. “Nanoparticle-Induced Property Changes in Nematic Liquid Crystals.” *Nanomaterials* 12 (2022), p. 341.

[25] He Huang et al. “Long-Lived Supramolecular Helices Promoted by Fluorinated Photoswitches.” *Macromolecular Rapid Communications* 39 (2018), p. 1700387.

[26] Tetiana N. Orlova, Roman I. Iegorov, and Alexei D. Kiselev. “Light-Induced Pitch Transitions in Photosensitive Cholesteric Liquid Crystals: Effects of Anchoring Energy.” *Physical Review E* 89 (2014), p. 012503.

[27] Jiaqin Li et al. “Dynamic Control of Multiple Optical Patterns of Cholesteric Liquid Crystal Microdroplets by Light-Driven Molecular Motors.” *CCS Chemistry* 0 (2023), pp. 1–29.

[28] E. Schrödinger. “An Undulatory Theory of the Mechanics of Atoms and Molecules.” *Physical Review* 28 (1926), pp. 1049–1070.

[29] M. Born and W. Heisenberg. “Zur Quantentheorie der Molekeln.” *Original Scientific Papers Wissenschaftliche Originalarbeiten*. Ed. by Walter Blum, Helmut Rechenberg, and Hans-Peter Dürr. 1985, pp. 216–246.

[30] D. R. Hartree. “The Wave Mechanics of an Atom with a Non-Coulomb Central Field. Part I. Theory and Methods.” *Mathematical Proceedings of the Cambridge Philosophical Society* 24 (1928), pp. 89–110.

[31] J. C. Slater. “The Theory of Complex Spectra.” *Physical Review* 34 (1929), pp. 1293–1322.

[32] V. Fock. “Näherungsmethode zur Lösung des quantenmechanischen Mehrkörperproblems.” *Zeitschrift für Physik* 61 (1930), pp. 126–148.

[33] David Maurice and Martin Head-Gordon. “Analytical Second Derivatives for Excited Electronic States Using the Single Excitation Configuration Interaction Method: Theory and Application to Benzo[a]Pyrene and Chalcone.” *Molecular Physics* 96 (1999), pp. 1533–1541.

[34] Martin Head-Gordon, David Maurice, and Manabu Oumi. “A Perturbative Correction to Restricted Open Shell Configuration Interaction with Single Substitutions for Excited States of Radicals.” *Chemical Physics Letters* 246 (1995), pp. 114–121.

[35] George D. Purvis III and Rodney J. Bartlett. “A Full Coupled-cluster Singles and Doubles Model: The Inclusion of Disconnected Triples.” *The Journal of Chemical Physics* 76 (1982), pp. 1910–1918.

[36] P. Hohenberg and W. Kohn. “Inhomogeneous Electron Gas.” *Physical Review* 136 (1964), B864–B871.

[37] Diola Bagayoko. “Understanding Density Functional Theory (DFT) and Completing It in Practice.” *AIP Advances* 4 (2014), p. 127104.

[38] Cottenier, S. *Density Functional Theory and the Family of (L)APW-methods: A Step-by-Step Introduction*. 2013.

[39] W. Kohn and L. J. Sham. “Self-Consistent Equations Including Exchange and Correlation Effects.” *Physical Review* 140 (1965), A1133–A1138.

[40] Kieron Burke and Lucas O. Wagner. “DFT in a Nutshell.” *International Journal of Quantum Chemistry* 113 (2013), pp. 96–101.

[41] Paul Dirac. “Note on Exchange Phenomena in the Thomas Atom.” *Mathematical Proceedings of the Cambridge Philosophical Society* 26 (1930), pp. 376–385.

[42] S. H. Vosko and L. Wilk. “Influence of an Improved Local-Spin-Density Correlation-Energy Functional on the Cohesive Energy of Alkali Metals.” *Physical Review B* 22 (1980), pp. 3812–3815.

[43] John P. Perdew et al. “Atoms, Molecules, Solids, and Surfaces: Applications of the Generalized Gradient Approximation for Exchange and Correlation.” *Physical Review B* 46 (1992), pp. 6671–6687.

[44] John P. Perdew, Kieron Burke, and Matthias Ernzerhof. “Generalized Gradient Approximation Made Simple.” *Physical Review Letters* 77 (1996), pp. 3865–3868.

[45] Axel D. Becke. “A New Mixing of Hartree–Fock and Local Density-functional Theories.” *The Journal of Chemical Physics* 98 (1993), pp. 1372–1377.

[46] P. J. Stephens et al. “Ab Initio Calculation of Vibrational Absorption and Circular Dichroism Spectra Using Density Functional Force Fields.” *The Journal of Physical Chemistry* 98 (1994), pp. 11623–11627.

[47] Jochen Heyd, Gustavo E. Scuseria, and Matthias Ernzerhof. “Hybrid Functionals Based on a Screened Coulomb Potential.” *The Journal of Chemical Physics* 118 (2003), pp. 8207–8215.

[48] Stefan Grimme. “Semiempirical Hybrid Density Functional with Perturbative Second-Order Correlation.” *The Journal of Chemical Physics* 124 (2006), p. 034108.

[49] S. F. Boys. “Electronic Wave Functions - I. A General Method of Calculation for the Stationary States of Any Molecular System.” *Proceedings of the Royal Society of London. Series A. Mathematical and Physical Sciences* 200 (1950), pp. 542–554.

[50] J. C. Slater. “Atomic Shielding Constants.” *Physical Review* 36 (1930), pp. 57–64.

[51] W. J. Hehre, R. Ditchfield, and J. A. Pople. “Self—Consistent Molecular Orbital Methods. XII. Further Extensions of Gaussian—Type Basis Sets for Use in Molecular Orbital Studies of Organic Molecules.” *The Journal of Chemical Physics* 56 (2003), pp. 2257–2261.

[52] Raoul Carfora et al. “A Cost-Effective Computational Strategy for the Electronic Layout Characterization of a Second Generation Light-Driven Molecular Rotary Motor in Solution.” *Journal of Computational Chemistry* 46 (2025), e70023.

[53] Jos C. M. Kistemaker et al. “Third-Generation Light-Driven Symmetric Molecular Motors.” *Journal of the American Chemical Society* 139 (2017), pp. 9650–9661.

[54] E. Wigner. “The Transition State Method.” *Transactions of the Faraday Society* 34 (1938), pp. 29–41.

[55] George H. Vineyard. “Frequency Factors and Isotope Effects in Solid State Rate Processes.” *Journal of Physics and Chemistry of Solids* 3 (1957), pp. 121–127.

[56] Graeme Henkelman and Hannes Jónsson. “Improved Tangent Estimate in the Nudged Elastic Band Method for Finding Minimum Energy Paths and Saddle Points.” *The Journal of Chemical Physics* 113 (2000), pp. 9978–9985.

[57] Gregory Mills, Hannes Jónsson, and Gregory K. Schenter. “Reversible Work Transition State Theory: Application to Dissociative Adsorption of Hydrogen.” *Surface Science* 324 (1995), pp. 305–337.

[58] *RheoMan - Nudged Elastic Band*. https://umet.univ-lille.fr/Projets/RheoMan/en/to-learn-more-about/nudged-elastic-band.php.html.

[59] Graeme Henkelman, Blas P. Uberuaga, and Hannes Jónsson. “A Climbing Image Nudged Elastic Band Method for Finding Saddle Points and Minimum Energy Paths.” *The Journal of Chemical Physics* 113 (2000), pp. 9901–9904.

[60] Vilhjálmur Ásgeirsson et al. “Nudged Elastic Band Method for Molecular Reactions Using Energy-Weighted Springs Combined with Eigenvector Following.” *Journal of Chemical Theory and Computation* 17 (2021), pp. 4929–4945.

[61] Yorick L. A. Schmerwitz, Vilhjálmur Ásgeirsson, and Hannes Jónsson. “Improved Initialization of Optimal Path Calculations Using Sequential Traversal over the Image-Dependent Pair Potential Surface.” *Journal of Chemical Theory and Computation* 20 (2024), pp. 155–163.

[62] Erich Runge and E. K. U. Gross. “Density-Functional Theory for Time-Dependent Systems.” *Physical Review Letters* 52 (1984), pp. 997–1000.

[63] Mark E. Casida. “Time-Dependent Density Functional Response Theory of Molecular Systems: Theory, Computational Methods, and Functionals.” *Theoretical and Computational Chemistry*. Vol. 4. 1996, pp. 391–439.

[64] Yorick LA Schmerwitz et al. “Variational Density Functional Calculations of Excited States: Conical Intersection and Avoided Crossing in Ethylene Bond Twisting.” *The Journal of Physical Chemistry Letters* 13 (2022), pp. 3990–3999.

[65] Elli Selenius et al. “Orbital-Optimized Versus Time-Dependent Density Functional Calculations of Intramolecular Charge Transfer Excited States.” *Journal of Chemical Theory and Computation* 20 (2024), pp. 3809–3822.

[66] Alec E. Sigurdarson et al. “Orbital-Optimized Density Functional Calculations of Molecular Rydberg Excited States with Real Space Grid Representation and Self-Interaction Correction.” *The Journal of Chemical Physics* 159 (2023), p. 214109.

[67] Ivan Tambovtsev et al. “Fine Tuning of the Rotational Speed of Light-Driven, Second-Generation Molecular Motors by Fluorine Substitution.” *The Journal of Physical Chemistry Letters* (2025), pp. 4014–4020.

[68] Aleksei V Ivanov et al. “Method for Calculating Excited Electronic States Using Density Functionals and Direct Orbital Optimization with Real Space Grid or Plane-Wave Basis Set.” *Journal of Chemical Theory and Computation* 17 (2021), pp. 5034–5049.

[69] Giuseppe M. J. Barca, Andrew T. B. Gilbert, and Peter M. W. Gill. “Simple Models for Difficult Electronic Excitations.” *Journal of Chemical Theory and Computation* 14 (2018), pp. 1501–1509.

[70] Gianluca Levi, Aleksei V Ivanov, and Hannes Jónsson. “Variational Density Functional Calculations of Excited States via Direct Optimization.” *Journal of Chemical Theory and Computation* 16 (2020), pp. 6968–6982.

[71] Yorick L. A. Schmerwitz, Gianluca Levi, and Hannes Jónsson. “Calculations of Excited Electronic States by Converging on Saddle Points Using Generalized Mode Following.” *Journal of Chemical Theory and Computation* 19 (2023), pp. 3634–3651.

[72] Yorick L. A. Schmerwitz, Elli Selenius, and Gianluca Levi. “Freeze-and-Release Direct Optimization Method for Variational Calculations of Excited Electronic States” (2025). arXiv: `2501.18568`.

[73] Tom Ziegler, Arvi Rauk, and Evert J. Baerends. “On the Calculation of Multiplet Energies by the Hartree-Fock-Slater Method.” *Theoretica Chimica Acta* 43 (1977), pp. 261–271.

[74] Ryojun Toyoda et al. “Synergistic Interplay between Photoisomerization and Photoluminescence in a Light-Driven Rotary Molecular Motor.” *Nature Communications* 13 (2022), p. 5765.

[75] Yihan Shao, Martin Head-Gordon, and Anna I. Krylov. “The Spin–Flip Approach within Time-Dependent Density Functional Theory: Theory and Applications to Diradicals.” *The Journal of Chemical Physics* 118 (2003), pp. 4807–4818.

[76] Daniele Toffoli et al. “Accurate Vertical Excitation Energies of BODIPY/Aza-BODIPY Derivatives from Excited-State Mean-Field Calculations.” *The Journal of Physical Chemistry A* 126 (2022), pp. 7137–7146.

[77] Víctor García-López, Dongdong Liu, and James M. Tour. “Light-Activated Organic Molecular Motors and Their Applications.” *Chemical Reviews* 120 (2020), pp. 79–124.

[78] Daisy R. S. Pooler et al. “Designing Light-Driven Rotary Molecular Motors.” *Chemical Science* 12 (2021), pp. 14964–14986.

[79] Diederik Roke, Sander J. Wezenberg, and Ben L. Feringa. “Molecular Rotary Motors: Unidirectional Motion around Double Bonds.” *Proceedings of the National Academy of Sciences of the United States of America* 115 (2018), pp. 9423–9431.

[80] Javier Vicario, Auke Meetsma, and Ben L. Feringa. “Controlling the Speed of Rotation in Molecular Motors. Dramatic Acceleration of the Rotary Motion by Structural Modification.” *Chemical Communications* (2005), pp. 5910–5912.

[81] Javier Vicario et al. “Fine Tuning of the Rotary Motion by Structural Modification in Light-Driven Unidirectional Molecular Motors.” *Journal of the American Chemical Society* 128 (2006), pp. 5127–5135.

[82] Arjen Cnossen et al. “A Trimer of Ultrafast Nanomotors: Synthesis, Photochemistry and Self-Assembly on Graphite.” *Chemistry* 15 (2009), pp. 2768–2772.

[83] Peter Štacko, Jos C. M. Kistemaker, and Ben L. Feringa. “Fluorine-Substituted Molecular Motors with a Quaternary Stereogenic Center.” *Chemistry – A European Journal* 23 (2017), pp. 6643–6653.

[84] Anouk S. Lubbe, Cosima L.G. Stähler, and Ben L. Feringa. “Light-driven Rotary Molecular Motors for Out-of-Equilibrium Systems.” *Out-of-Equilibrium (Supra)Molecular*

Systems and Materials. Ed. by Nicolas Giuseppone and Andreas Walther. 2021, pp. 337–377.

[85] Roland Wilcken et al. "Complete Mechanism of Hemithioindigo Motor Rotation." *Journal of the American Chemical Society* 140 (2018), pp. 5311–5318.

[86] Euan R. Kay and David A. Leigh. "Beyond Switches: Rotaxane- and Catenane-Based Synthetic Molecular Motors." *Pure and Applied Chemistry* 80 (2008), pp. 17–29.

[87] P. G. de Gennes et al. *The Physics of Liquid Crystals*. International Series of Monographs on Physics. 1995.

[88] Iain W. Stewart. "Continuum Theory for Liquid Crystals." *Handbook of Liquid Crystals*. Ed. by John W Goodby et al. 2014, pp. 1–36.

[89] F.M. Leslie. "Theory of Flow Phenomena in Liquid Crystals." *Advances in Liquid Crystals*. Vol. 4. 1979, pp. 1–81.

[90] Chengteh Lee, Weitao Yang, and Robert G. Parr. "Development of the Colle-Salvetti Correlation-Energy Formula into a Functional of the Electron Density." *Physical Review B* 37 (1988), pp. 785–789.

[91] A. D. Becke. "Density-Functional Exchange-Energy Approximation with Correct Asymptotic Behavior." *Physical Review A* 38 (1988), pp. 3098–3100.

[92] Axel D. Becke. "Density-functional Thermochemistry. III. The Role of Exact Exchange." *The Journal of Chemical Physics* 98 (1993), pp. 5648–5652.

[93] Florian Weigend. "Accurate Coulomb-fitting Basis Sets for H to Rn." *Physical Chemistry Chemical Physics* 8 (2006), pp. 1057–1065.

[94] Frank Neese. "The ORCA Program System." *WIREs Computational Molecular Science* 2 (2012), pp. 73–78.

[95] Frank Neese. "Software Update: The ORCA Program System—Version 5.0." *WIREs Computational Molecular Science* 12 (2022), e1606.

[96] Yorick Leonard Adrian Schmerwitz et al. "Saddle Point Search Algorithms for Variational Density Functional Calculations of Excited Electronic States with Self-Interaction Correction." *Proceedings of the Platform for Advanced Scientific Computing Conference*. 2024, pp. 1–11.

[97] Michael M. Pollard, Auke Meetsma, and Ben L. Feringa. "A Redesign of Light-Driven Rotary Molecular Motors." *Organic and Biomolecular Chemistry* 6 (2008), pp. 507–512.

[98] Michael M. Pollard et al. "On the Effect of Donor and Acceptor Substituents on the Behaviour of Light-Driven Rotary Molecular Motors." *Organic and Biomolecular Chemistry* 6 (2008), pp. 1605–1612.

[99] Jiaxin Hou et al. "Phototriggered Complex Motion by Programmable Construction of Light-Driven Molecular Motors in Liquid Crystal Networks." *Journal of the American Chemical Society* 144 (2022), pp. 6851–6860.

[100] Ruochen Lan et al. "Amplifying Molecular Scale Rotary Motion: The Marriage of Overcrowded Alkene Molecular Motor with Liquid Crystals." *Advanced Materials* 34 (2022), p. 2109800.

[101] Jian Sun et al. "Light-Driven Self-Oscillating Behavior of Liquid-Crystalline Networks Triggered by Dynamic Isomerization of Molecular Motors." *Advanced Functional Materials* 31 (2021), p. 2103311.

[102] Yuna Kim and Nobuyuki Tamaoki. “Photoresponsive Chiral Dopants: Light-Driven Helicity Manipulation in Cholesteric Liquid Crystals for Optical and Mechanical Functions.” *ChemPhotoChem* 3 (2019), pp. 284–303.

[103] Fan Yang, Bingbing Yue, and Liangliang Zhu. “Light-Triggered Modulation of Supramolecular Chirality.” *Chemistry – A European Journal* 29 (2023), e202203794.

[104] Nagatoshi Koumura et al. “Second Generation Light-Driven Molecular Motors. Unidirectional Rotation Controlled by a Single Stereogenic Center with Near-Perfect Photoequilibria and Acceleration of the Speed of Rotation by Structural Modification.” *Journal of the American Chemical Society* 124 (2002), pp. 5037–5051.

[105] M. M. Pollard et al. “Rate Acceleration of Light-Driven Rotary Molecular Motors.” *Advanced Functional Materials* 17 (2007), pp. 718–729.

[106] Ivan I Smalyukh. “Review: Knots and Other New Topological Effects in Liquid Crystals and Colloids.” *Reports on Progress in Physics* 83 (2020), p. 106601.

[107] Jin-Sheng Wu and Ivan I. Smalyukh. “Hopfions, Heliknotons, Skyrmions, Torons and Both Abelian and Nonabelian Vortices in Chiral Liquid Crystals.” *Liquid Crystals Reviews* 10 (2022), pp. 34–68.

[108] I.M. Tambovtsev et al. “Topological Structures in Chiral Media: Effects of Confined Geometry.” *Physical Review E* 105 (2022), p. 034701.

Appendix A: Publications

Paper I

Fine Tuning of the Rotational Speed of Light-Driven, Second-Generation Molecular Motors by Fluorine Substitution

Ivan Tambovtsev et al.

J. Phys. Chem. Lett. 16, 4014-4020 (2025)

Performed DFT/NEB/HTST; wrote and edited.

THE JOURNAL OF
PHYSICAL CHEMISTRY
LETTERS
A JOURNAL OF THE AMERICAN CHEMICAL SOCIETY

pubs.acs.org/JPCL Letter

Fine Tuning of the Rotational Speed of Light-Driven, Second-Generation Molecular Motors by Fluorine Substitution

Ivan Tambovtsev,* Yorick L. A. Schmerwitz, Gianluca Levi, Darina D. Darmoroz, Pavel V. Nesterov, Tetiana Orlova, and Hannes Jónsson*

Cite This: J. Phys. Chem. Lett. 2025, 16, 4014−4020 Read Online

ACCESS | Metrics & More | Article Recommendations | Supporting Information

ABSTRACT: The elementary steps in the rotation of several second-generation molecular motors are analyzed by finding the minimum energy path between the metastable and stable states and evaluating the transition rate within harmonic transition state theory based on energetics obtained from density functional theory. Comparison with published experimental data shows remarkably good agreement and demonstrates the predictive capability of this approach. While previous measurements by Feringa and co-workers have shown that a replacement of the hydrogen atom at the stereogenic center by a fluorine atom can slow down the rate-limiting thermal helix inversion (THI) step by raising the energy of the transition state, even to the extent that the backreaction in the ground state becomes preferred in some cases, we find that a replacement of a CH_3 group by CF_3 at the same site accelerates the THI by elevating the energy of the metastable state without affecting the transition state significantly. Since these two fluorine substitutions have an opposite effect on the rate of the THI, the combination of both can provide ways to fine-tune the rotational speed of molecular motors.

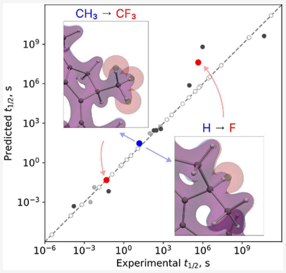

The development of light-powered molecular motors, where one part of a molecule rotates a full cycle with respect to the other, has been an active field of research in the past two decades, driven by their applications in a wide range of fields, such as optics, photonics and light-driven soft materials, to name a few. Several such molecular motors have therefore been developed.[1−3] Most contain a C═C double bond with one side of the bond referred to as the "rotor" and the other referred to as the "stator". The absorption of a photon leads to a ca. 90° rotation of the double bond in the excited electronic state and, after relaxation to the ground electronic state, further rotation to a metastable state. From there, a thermally induced transition, the so-called thermal helix inversion (THI), to a more stable state can occur, corresponding to a rotation by 180°. The stage is then set for the absorption of another photon and analogous steps as before to complete the 360° rotational cycle. The absorbed energy from the photons is thereby converted into repeatable and controllable molecular motion.[4−7] If, however, the rate of the THI is lower than the rate of thermally activated return to the original state on the ground state energy surface, the molecule is not likely to perform a full rotation. The energy landscape corresponding to the ground electronic state therefore plays an important role in addition to that of the electronically excited state. An example molecule that has been shown to be an efficient rotor[8] is shown in Figure 1 with an illustration of the various states, and the transitions between them.

A great deal of effort has focused on various structural modifications of the molecules to tune both the wavelength of light capable of inducing the photochemical step of the rotation and the rate of the subsequent THI step.[5,8] This has led to the development of three generations of molecular motors. A particularly interesting and promising one is the second generation where only a single stereogenic center in the molecular structure is sufficient to ensure unidirectional rotation. There, the energy barriers for the two THI steps in the rotary cycle are similar, unlike the first generation of rotors.[6,9−11] Moreover, when the stator part of a second-generation molecular motor is symmetric, the third and fourth steps that take place after absorption of the second photon are essentially the same as the first and second steps.

This makes second-generation molecular motors particularly suitable for the development of light-controllable materials where molecular-scale rotational motion is amplified to a macroscopic level due to a cooperative effect on the environment. Molecular motors can be used to create continuous unidirectional movement of a macroscopic motor, where the rotation speed is determined indirectly by

Received: February 9, 2025
Revised: April 4, 2025
Accepted: April 8, 2025

https://doi.org/10.1021/acs.jpclett.5c00408
J. Phys. Chem. Lett. 2025, 16, 4014−4020

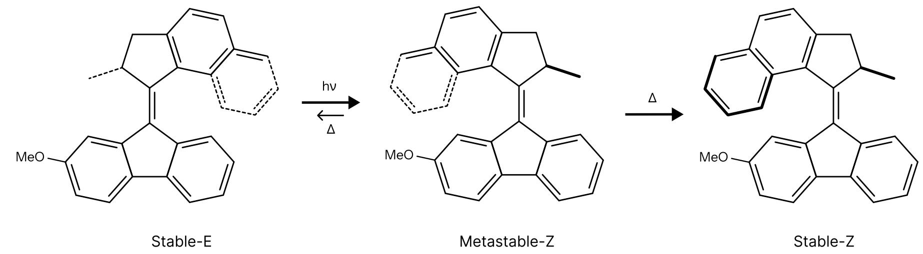

Figure 1. Illustration of the first two steps in the rotation of a second-generation molecular motor developed by Feringa and co-workers.[8] After photoabsorption, the structure evolves from the stable E state to the metastable Z state, first a ca. 90° rotation in the excited electronic state and then further rotation after returning to the ground state. From there, a thermally activated transition, the thermal helix inversion (THI), can bring the molecule to the stable Z state thereby completing a ca. 180° rotation. For an efficient rotor, the transition back to the E state should have significantly lower probability than the THI. Absorption of a second photon in the stable Z state and a repeat of a THI step then completes a full circle.

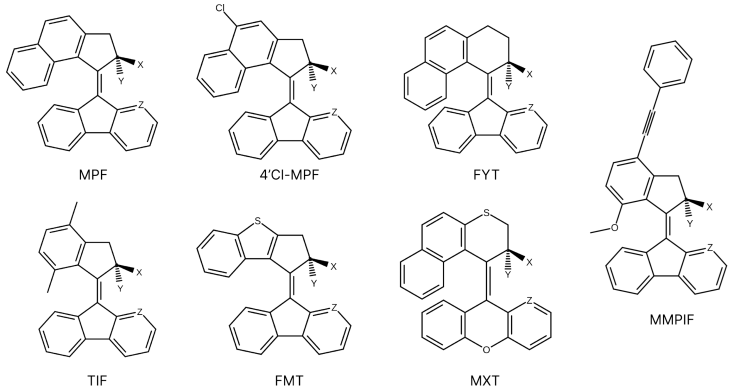

Figure 2. Molecular motors investigated in the present study to assess the effect of fluorine and nitrogen substitutions. The sites are labeled X, Y, and Z and they have a CH_3, H, and CH, respectively, in the base molecules, but CF_3, F, or N in the modified molecules.

that of the molecular motors used as dopants.[12] Moreover, since the photoisomerization of second-generation motors is accompanied by a change in molecular chirality that is amplified to the supramolecular level, a variety of optical and photonic elements can also be developed.[13,14] For example, by doping a liquid crystal (LC) or a liquid crystalline network with molecular motors, new prospects for soft robotics and multifunctional soft actuators have been opened.[15−18]

The optimal rotation rate depends on the application and is different, for example, for liquid crystal mixtures, LC-based elastomers and polymers. Slow rotation is suitable for data storage and information technology while fast rotation is appropriate for switchable optical elements such as liquid crystal displays, sensors and optical gates. If the characteristic elastic relaxation time of a chiral nematic liquid crystal significantly exceeds the photoisomer relaxation time, then the switching time is controlled by the rotational viscosity and elastic constants of the liquid crystal host.

The THI is typically the rate-limiting step in the rotation. Various ways of tuning its rate have therefore been explored, mainly by modifying the structure of the molecular skeleton. One approach for tuning molecular properties that has been used in several various contexts is fluorination, i.e. the replacement of one or more hydrogen atoms with fluorine. Fluorination has, for example, been used to adjust the half-life of the helical LC state of chiral azobenzenes with almost no effect on the photoabsorption properties.[19,20] Fluorination of second-generation molecular motors has been explored by Feringa and co-workers,[21] who found that a replacement of a hydrogen atom by a fluorine atom at the stereogenic center, i.e. the rotor's carbon atom next to the double bond, slows down the THI. Their analysis of experimentally measured rates and density functional theory (DFT) calculations of energy barriers led to the conclusion that the main effect of this fluorine substitution is an increase in the energy of the transition state due to steric effects while the relative free energy of the stable and metastable states is not significantly affected.[21] They also found that for some of the fluorinated molecules, the thermally activated transition from the metastable state back to the initial state becomes faster than the THI, thereby inhibiting rotation.

In the present theoretical study, another hydrogen to fluorine substitution is explored, namely the replacement of a CH_3 group by a CF_3 group at the stereogenic center. We find this to have the opposite effect, namely an increase of the THI rate and thereby increased rotational speed. The reason for this is an increase in the energy of the metastable state while the transition state turns out not to be affected significantly. Harmonic transition state theory (HTST) is used to estimate the transition rate of the thermally activated steps, with both the pre-exponential factor in the Arrhenius rate expression as well as the energy barrier obtained from density functional calculations with a hybrid density functional. To test this approach, we compare the calculated half-life for a wide range of previously investigated second-generation molecular motors with experimentally measured values and find remarkably close agreement. Calculations are also performed to assess the effect of fluorine substitution on the wavelength of light absorbed by the stable and metastable states. In addition to fluorination, we study the effect of placing an N atom instead of a CH in the stator where steric hindrance occurs during the THI.

The second-generation motors studied here are shown in Figure 2. The sites are labeled by X, Y, Z, and have CH_3, H, and CH, respectively, in the base molecule while the substitutions introduce CF_3, F, or N. If Z is CH, the stator is symmetric and the state after THI is equivalent to the initial state.

We first address the accuracy of the theoretical approach used here for estimating the rate of the thermally activated steps, the THI and the backreaction in the ground electronic state. Figure 3(a) compares the calculated half-life of the metastable state of the various rotors with experimentally measured values. Both the THI and backreaction steps are taken into account. Results for the base molecules as well as molecules where H has been replaced by F at site Y, and several other second-generation motors for which experimental data is available are shown. The experimental data is taken from refs 8, 11, and 21−25 (see the Supporting Information (SI)). Five molecules with an alkane group at site X different from the methyl group are included in the comparison, as experimental data for them is available.[11,23,26] The close agreement between measured and calculated values lends support for the theoretical methodology used here and thereby also the predictions we make for new modifications of the rotors. For molecules F−MPF and F−TIF the calculated rate of the backreaction turns out to be larger than the rate of the THI step, in agreement with experimental measurements.[21]

Figure 3(b) shows predicted changes in the rate of the THI step for the various molecular motors by introducing CF_3 at site X and/or F at site Y. In all cases, the F substitution decreases the rate, consistent with the measurements for four of these molecules by Feringa and co-workers.[21] The introduction of CF_3 is, however, predicted to increase the rate. The reason for the decrease in the rate by the F substitution is higher energy barrier for the THI step, while the increase in the rate by the CF_3 substitution is due to elevated energy of the metastable state. The pre-exponential factor in the Arrhenius rate expression is typically increased by the former and reduced by the latter, but the changes are within a factor 2, so the changes in activation energy dominate. When both substitutions are made, the half-life is in general increased, but less than for the H to F substitution alone. The combination of the two, therefore, enables finer tuning of the rate. The changes in the pre-exponential factor and the activation energy are tabulated in the SI. In most cases, the rate of the THI is greater than that of the backreaction, and since it is the rate-limiting step in the rotation, it defines the overall rotational speed. Only for CF_3−FYT and CF_3−MXT is the backreaction faster than the THI.

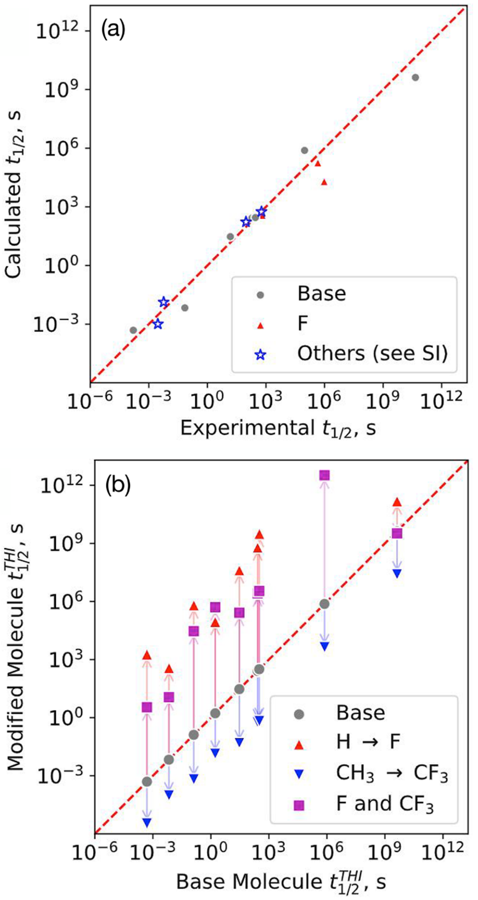

Figure 3. (a) Comparison of calculated and measured half-life of the metastable state of various second-generation molecular motors. Both the THI step and the backreaction are taken into account. Data corresponding to the base molecules (shown in Figure 1) is shown in gray, while red illustrates data for molecules where H has been replaced by F at site Y. Data on additional second-generation motors is marked with blue stars. The experimental data is obtained from refs8, 11, 21−25. (see the SI). The agreement between measured and calculated values is remarkably good, the red dashed line indicating perfect agreement. (b) Calculated half-life of the THI step and its change by substitution of CH_3 by CF_3 at site X (blue), substitution of H by F at site Y (red), and both substitutions combined (purple). The CF_3 substitution increases the rate of the THI step, whereas the F substitution decreases it, as indicated by the arrows.

As can be seen in Figure 3, the rate of THI varies over a wide range, nearly 15 orders of magnitude. Figure 4(a-h) shows an analysis of the effect of the two fluorine substitutions on the atomic structure of the FMT molecule in the stable and metastable states, characterized by the two local minima, as well as in the transition state characterized by the saddle point on the energy surface, i.e. the transition structure, for the THI

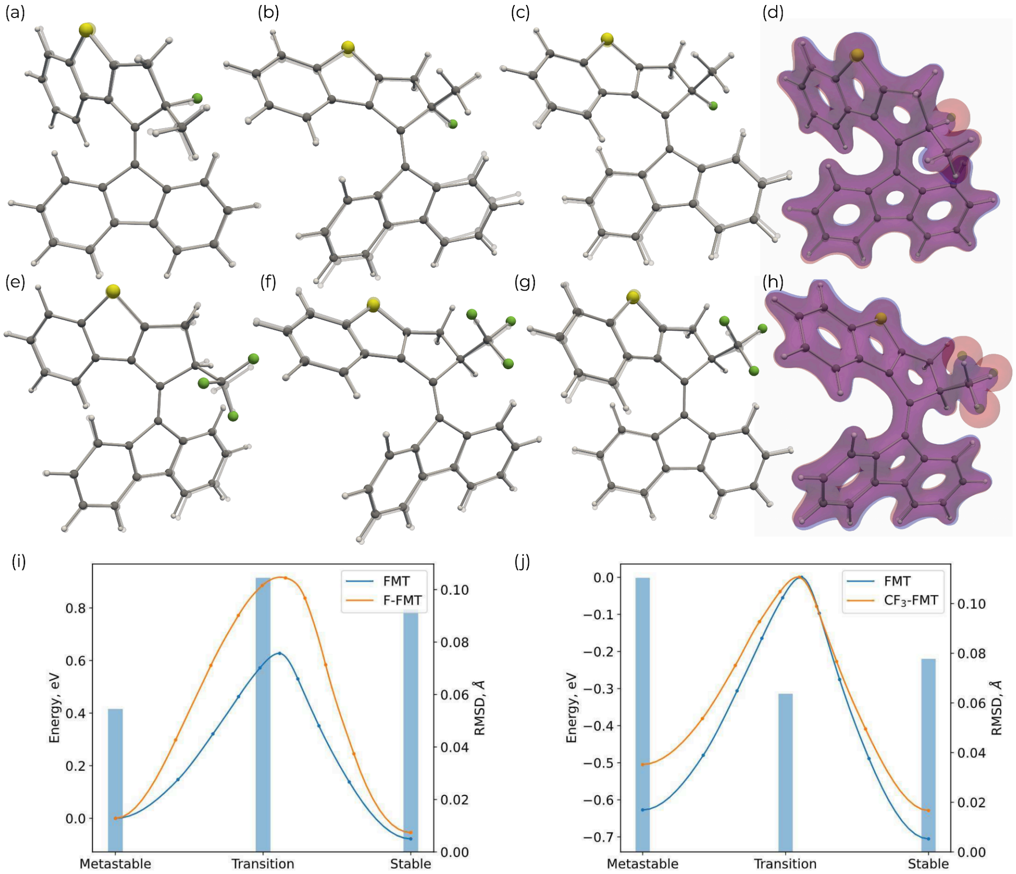

Figure 4. Effect of the H to F substitution at site Y, and the CH_3 to CF_3 substitution at site X of the FMT molecule. The F atoms are shown in green. (a,b,c): Change in the metastable state, transition structure, and stable state due to the H to F substitution (F−FMT). The structures are aligned at the C═C bond. (e,f,g): Analogous change due to the CH_3 to CF_3 substitution (CF_3−FMT). The electron density rendered at 0.1 Bohr^{-3} is shown for the metastable state of F−FMT in (d), and for the transition structure of CF_3−FMT in (h). Blue: original molecule, FMT. Red: Modified molecule. (i) and (j): Minimum energy path between the metastable and stable states for the base and modified molecules. The blue bars indicate the RMSD between the structure of the base and modified molecule. The zero of energy is chosen to be the energy of the state with the smallest RMSD. The H to F substitution mainly affects the transition structure and reduces the rate of THI, but the CH_3 to CF_3 substitution mainly affects the metastable state and increases the rate.

step. The molecular structure before and after substitution is compared by aligning them at the C═C bond. When F is introduced at the Y site, the largest change in structure occurs for the transition structure, while the metastable state is changed most when CF_3 is introduced into site X. The figure also shows the increase in electron density at the X and Y sites when the fluorine atoms are introduced. The steric hindrance in the transition state for the THI step is increased when fluorine is introduced into site Y, but the main effect of introducing CF_3 at site X is in the metastable state.

The change in the minimum energy path for the THI step, calculated using the climbing-image nudged elastic band method (CI-NEB),[27−29] is shown in Figure 4(i,j). The zero of energy in each case is chosen to be the energy of the state for which the atomic structure changes the least as indicated by the smallest root-mean-square deviation (RMSD). For the fluorine substitution at site Y, this is the transition structure, while for the substitution at site X, it is the metastable state. This illustrates clearly that the main effect of the former is to raise the energy barrier, while the energy of the metastable state with respect to the stable state is not affected much, in agreement with the conclusions reached earlier by Feringa and co-workers.[21]

However, the CH_3 to CF_3 substitution at site X has a different effect, namely an increase in the energy of the metastable state, while the energy of the transition structure is not changed significantly. As a result, the substitution at site X increases the rotational speed of the molecule, whereas the substitution at site Y slows it down. The analysis of these effects for FMT shown in Figure 4 is representative for the other molecules studied here (see the SI).

The increase in the electron density at site Y when the H atom is replaced by an F atom, is illustrated in Figure 4(d). This leads to greater steric hindrance with the stator during the rotation as is evident from the changes in the transition structure and the height of the energy barrier. The distance between the F atom and the H atom in the Z site of the stator is 0.3 Å larger than the distance between the two corresponding H atoms of the base molecule in the transition structure (see the SI).

The substitution of CH_3 by CF_3 at site X also increases the electron density at that site, as shown in Figure 4(h), but this turns out to introduce an increase in steric hindrance in the metastable state, as can be deduced from the atomic structure changes illustrated in Figure 4(e-g) and the change in energy along the minimum energy path shown in Figure 4(j). The increase in distance between the H atom in the Z site of the stator and the closest F atom at site X as compared to the distance between the two corresponding H atoms in the base molecule is evident mainly in the metastable state, where it is more than 0.5 Å, while there is little increase in this distance in the transition structure (see Figure S1). The energy of the transition structure for the backreaction is not affected significantly by the fluorine substitutions (see Figure S2).

Further analysis of the steric effect of all the molecules studied here is shown in Figure S3. The average distance between the H atom at site Y of the rotor and atoms of the stator that are within 2.9 Å (the sum of van der Waals radii of C and H atoms) in either of the two states is shorter in the transition structure than in the metastable state structure, consistent with steric hindrance being larger for the transition state. Conversely, the average distance between the three H atoms of the CH_3 group at site X and atoms of the stator that are within 2.9 Å is shorter in the metastable state structure than in the transition structure, so there the steric hindrance is larger for the metastable state. The substitution of H by F at site Y therefore affects the transition state more strongly, while the substitution of CH_3 by CF_3 at site X has a greater impact on the metastable state.

An important aspect in the design of molecular motors is the difference in wavelength of absorbed light by the stable and metastable states. A larger difference is better as it reduces the likelihood of exciting the metastable state and thereby a photoinduced backreaction. Calculations of spectra for the molecules studied here reveal that this difference increases when the CH_3 to CF_3 substitution at site X is made, up to 26 nm for MXT. However, it decreases when H is substituted by F at site Y. When both substitutions are made, the difference in absorption wavelength tends to increase (see Table S1).

Since the steric hindrance of the rotor with the Z site of the stator appears to be an important aspect for determining the rate of the THI, another substitution has been studied where the CH at site Z is replaced by an N atom. This has been tested for two of the molecules, MPF and TIF. In both cases, an increase in the energy of the metastable state by ca. 0.15 eV is found, with little effect on the transition structure. As a result, the half-life of the metastable state is predicted to decrease. However, as only two molecules have been studied, further investigation is required to see how general this effect is. This replacement of CH by N at site Z is also not found to significantly affect the way the fluorine substitution at site X or Y changes the rate of the THI step.

In summary, the rate-limiting step in the rotation of a variety of second-generation molecular motors, the metastable to stable state transition, i.e. THI step, as well as the competing backreaction have been studied theoretically using HTST to evaluate the transition rate based on energy and atomic forces obtained from DFT with the B3LYP hybrid functional. Remarkably good agreement is obtained between the calculated and experimentally measured lifetime of the metastable state establishing the validity of this approach and providing support for predictions made regarding new variants. A CH_3 to CF_3 substitution at the stereogenic center of the rotor is proposed as a way to increase the rotational speed, opposite to the effect of the H to F substitution which has previously been studied by Feringa and co-workers.[21] By analyzing the minimum energy path of the transitions, calculated using the CI-NEB method, the effect of these fluorine substitutions can be explained. The CF_3 substitution turns out to raise the energy of the metastable state, while it has little effect on the transition structure. The H to F substitution, however, raises the energy of the transition structure, while the metastable state is barely affected. When both the F and the CF_3 substitutions are made, the rate of the THI step, and thereby the rotational speed, is higher than if only the F substitution is made, but lower than that of the original molecule, thereby providing an opportunity for fine-tuning. Furthermore, the calculated wavelength of light absorbed indicates that CF_3 substitution increases the separation between the absorption peaks of the stable state and the metastable state. This makes it easier to selectively excite the stable state by an appropriate choice of the wavelength of the incident light. The photoisomerization quantum yield is another important factor, but is not addressed here.

■ METHODS

The rate constants for the thermally activated transitions in the ground electronic state are calculated using the harmonic approximation to transition state theory[30,31]

$$k_{\mathrm{HTST}} = \frac{\prod_i^{3N} \nu_i^{\min}}{\prod_i^{3N-1} \nu_i^{\ddagger}} \exp[-(E^{\ddagger} - E^{\min})/k_{\mathrm{B}}T] \tag{1}$$

where $\nu_i^{\min}$ and $\nu_i^{\ddagger}$ refer to vibrational frequency, and $E^{\min}$ and $E^{\ddagger}$ refer to the energy of the initial state minimum and first-order saddle point, respectively. A vibrational analysis is, furthermore, used to confirm that the stable and metastable structures are local minima on the energy surface and the transition structures correspond to first-order saddle points. The calculated values of the pre-exponential factor, activation energy and rate constant are given in the SI. The half-life of the metastable state shown in Figure 3(a) is obtained from the THI and backreaction (thermal inversion, TI) rate constants as $\tau = \ln 2/(k_{\mathrm{THI}} + k_{\mathrm{TI}})$. The half-life of the THI step shown in Figure 3(b) is $t_{1/2}^{\mathrm{THI}} = \ln 2/k_{\mathrm{THI}}$.

The transition structure for the thermally activated steps is determined by calculating the minimum energy path between the metastable-Z state and the stable-Z state. The configuration of maximal energy along the path corresponds to the saddle point that is used in HTST to represent the transition state. The climbing-image nudged elastic band (CI-NEB) method[27−29] is used as implemented in the ORCA software[32,33] with energy weighted springs[34] starting from an initial guess obtained by the sequential image depended pair potential (S-IDPP) method.[35] The location of the images of the molecule along the path are converged to a tolerance of 2.5 × 10^{-3} a.u. and 5 × 10^{-3} a.u. in the root-mean-square (RMS) and maximum component (MAX) of the force perpendicular to the image tangents, respectively, with 1 order of magnitude tighter tolerance on the CI. CI-NEB is followed by a first-order saddle point search with the CI as the initial guess[34] and is converged to a tolerance of 5 × 10^{-6} a.u., 3 × 10^{-4} a.u., 10^{-4} a.u., 4 × 10^{-3} a.u., and 2 × 10^{-3} a.u. for the two-step energy change, the MAX and RMS of the gradient, and the MAX and RMS of the optimization step, respectively.

The energy of the system and atomic forces are estimated using density functional theory (DFT) calculations with the B3LYP hybrid functional approximation.[36−38] The orbitals are expressed as linear combinations of atomic orbitals using the 6−31G(d,p) basis set.[39,40] The electronic structure calculations are converged to thresholds of 10^{-8} a.u., 10^{-7} a.u., 5 × 10^{-9} a.u., and 5 × 10^{-7} a.u. for the two-step energy change, the MAX and RMS of the two-step density change, and the error of the direct inversion in the iterative subspace (DIIS), respectively. The structures of the stable and metastable states of all molecular motors are optimized to a tolerance of 10^{-4} a.u., 3 × 10^{-4} a.u., 2 × 10^{-3} a.u., and 4 × 10^{-3} a.u. for the RMS and MAX of the gradient and the RMS and MAX of the optimization step, respectively. The DFT calculations are performed with version 5.0.4 of the ORCA software.[32,33,41−43]

While the agreement between calculated and measured values of the lifetime of the metastable state is remarkably good, as illustrated in Figure 3(a), our theoretical approach involves several approximations. The calculations are carried out for isolated molecules while the measurements are carried out on solvated molecules. Also the use of the harmonic approximation to TST rather than full free energy calculations are used, and the energetics are approximated with the B3LYP density functional. The remarkably close agreement between calculated and measured values of the half-life for a wide range of molecular motors using this approach is likely a result of some cancellation of errors.

The optical spectra are obtained with linear-response time-dependent density functional theory[44,45] (TDDFT) using the B3LYP functional in the adiabatic approximation. This approach has previously been found to provide results in agreement with experimental measurements for the base MPF molecular rotor.[46]

Data from the calculations is extracted using the ChemParse software.

■ ASSOCIATED CONTENT

Data Availability Statement

The data supporting the findings of this work are available for download at Zenodo.[47]

Supporting Information

The Supporting Information is available free of charge at https://pubs.acs.org/doi/10.1021/acs.jpclett.5c00408.

> Results on analysis of the changes in atomic distances, minimum energy paths, calculated wavelength of light absorbed, and calculated rates (PDF)
>
> Transparent Peer Review report available (PDF)

■ AUTHOR INFORMATION

Corresponding Authors

Ivan Tambovtsev − *Science Institute and Faculty of Physical Sciences, University of Iceland, 107 Reykjavík, Iceland*; Email: ivt3@hi.is

Hannes Jónsson − *Science Institute and Faculty of Physical Sciences, University of Iceland, 107 Reykjavík, Iceland*; orcid.org/0000-0001-8285-5421; Email: hj@hi.is

Authors

Yorick L. A. Schmerwitz − *Science Institute and Faculty of Physical Sciences, University of Iceland, 107 Reykjavík, Iceland; Max-Planck-Institut für Kohlenforschung, 45470 Mülheim an der Ruhr, Germany*; orcid.org/0000-0001-6277-0359

Gianluca Levi − *Science Institute and Faculty of Physical Sciences, University of Iceland, 107 Reykjavík, Iceland*; orcid.org/0000-0002-4542-0653

Darina D. Darmoroz − *Infochemistry Scientific Center, ITMO University, Saint-Petersburg 191002, Russia*

Pavel V. Nesterov − *Infochemistry Scientific Center, ITMO University, Saint-Petersburg 191002, Russia*

Tetiana Orlova − *Infochemistry Scientific Center, ITMO University, Saint-Petersburg 191002, Russia*

Complete contact information is available at: https://pubs.acs.org/10.1021/acs.jpclett.5c00408

Notes

The authors declare no competing financial interest.

■ ACKNOWLEDGMENTS

This work was funded by the Icelandic Research Fund (grant nos. 239970, 217751 and 2511544) and the University of Iceland Research Fund. Y.L.A.S. acknowledges support by the Max Planck Society. The calculations were carried out at the IREI computer facility located at the University of Iceland.

■ REFERENCES

(1) Corra, S.; Curcio, M.; Credi, A. Photoactivated Artificial Molecular Motors. *JACS Au* **2023**, *3*, 1301−1313.

(2) Baroncini, M.; Silvi, S.; Credi, A. Photo- and Redox-Driven Artificial Molecular Motors. *Chem. Rev.* **2020**, *120*, 200−268.

(3) Jeong, M.; Park, J.; Kwon, S. Molecular Switches and Motors Powered by Orthogonal Stimuli. *Eur. J. Org. Chem.* **2020**, *2020*, 7254−7283.

(4) García-López, V.; Liu, D.; Tour, J. M. Light-Activated Organic Molecular Motors and Their Applications. *Chem. Rev.* **2020**, *120*, 79−124.

(5) Pooler, D. R. S.; Lubbe, A. S.; Crespi, S.; Feringa, B. L. Designing Light-Driven Rotary Molecular Motors. *Chemical Science* **2021**, *12*, 14964−14986.

(6) Roke, D.; Wezenberg, S. J.; Feringa, B. L. Molecular Rotary Motors: Unidirectional Motion around Double Bonds. *Proc. Natl. Acad. Sci. U.S.A.* **2018**, *115*, 9423−9431.

(7) Koumura, N.; Zijlstra, R. W. J.; van Delden, R. A.; Harada, N.; Feringa, B. L. Light-Driven Monodirectional Molecular Rotor. *Nature* **1999**, *401*, 152−155.

(8) Vicario, J.; Meetsma, A.; Feringa, B. L. Controlling the Speed of Rotation in Molecular Motors. Dramatic Acceleration of the Rotary Motion by Structural Modification. *Chem. Commun.* **2005**, 5910−5912.

(9) Koumura, N.; Geertsema, E. M.; van Gelder, M. B.; Meetsma, A.; Feringa, B. L. Second Generation Light-Driven Molecular Motors. Unidirectional Rotation Controlled by a Single Stereogenic Center with Near-Perfect Photoequilibria and Acceleration of the Speed of

Rotation by Structural Modification. *J. Am. Chem. Soc.* **2002**, *124*, 5037−5051.

(10) Conyard, J.; Cnossen, A.; Browne, W. R.; Feringa, B. L.; Meech, S. R. Chemically Optimizing Operational Efficiency of Molecular Rotary Motors. *J. Am. Chem. Soc.* **2014**, *136*, 9692−9700.

(11) Vicario, J.; Walko, M.; Meetsma, A.; Feringa, B. L. Fine Tuning of the Rotary Motion by Structural Modification in Light-Driven Unidirectional Molecular Motors. *J. Am. Chem. Soc.* **2006**, *128*, 5127−5135.

(12) Orlova, T.; Lancia, F.; Loussert, C.; Iamsaard, S.; Katsonis, N.; Brasselet, E. Revolving Supramolecular Chiral Structures Powered by Light in Nanomotor-Doped Liquid Crystals. *Nat. Nanotechnol.* **2018**, *13*, 304−308.

(13) Yang, F.; Yue, B.; Zhu, L. Light-Triggered Modulation of Supramolecular Chirality. *Chemistry A European Journal* **2023**, *29*, e202203794.

(14) Kim, Y.; Tamaoki, N. Photoresponsive Chiral Dopants: Light-Driven Helicity Manipulation in Cholesteric Liquid Crystals for Optical and Mechanical Functions. *ChemPhotoChem.* **2019**, *3*, 284−303.

(15) Hou, J.; Long, G.; Zhao, W.; Zhou, G.; Liu, D.; Broer, D. J.; Feringa, B. L.; Chen, J. Phototriggered Complex Motion by Programmable Construction of Light-Driven Molecular Motors in Liquid Crystal Networks. *J. Am. Chem. Soc.* **2022**, *144*, 6851−6860.

(16) Lan, R.; Bao, J.; Huang, R.; Wang, Z.; Zhang, L.; Shen, C.; Wang, Q.; Yang, H. Amplifying Molecular Scale Rotary Motion: The Marriage of Overcrowded Alkene Molecular Motor with Liquid Crystals. *Adv. Mater.* **2022**, *34*, 2109800.

(17) Hou, J.; Mondal, A.; Long, G.; de Haan, L.; Zhao, W.; Zhou, G.; Liu, D.; Broer, D. J.; Chen, J.; Feringa, B. L. Photo-Responsive Helical Motion by Light-Driven Molecular Motors in a Liquid-Crystal Network. *Angew. Chem., Int. Ed.* **2021**, *60*, 8251−8257.

(18) Sun, J.; Hu, W.; Zhang, L.; Lan, R.; Yang, H.; Yang, D.-K. Light-Driven Self-Oscillating Behavior of Liquid-Crystalline Networks Triggered by Dynamic Isomerization of Molecular Motors. *Adv. Funct. Mater.* **2021**, *31*, 2103311.

(19) Huang, H.; Orlova, T.; Matt, B.; Katsonis, N. Long-Lived Supramolecular Helices Promoted by Fluorinated Photoswitches. *Macromol. Rapid Commun.* **2018**, *39*, 1700387.

(20) Bléger, D.; Schwarz, J.; Brouwer, A. M.; Hecht, S. O-Fluoroazobenzenes as Readily Synthesized Photoswitches Offering Nearly Quantitative Two-Way Isomerization with Visible Light. *J. Am. Chem. Soc.* **2012**, *134*, 20597−20600.

(21) Štacko, P.; Kistemaker, J. C. M.; Feringa, B. L. Fluorine-Substituted Molecular Motors with a Quaternary Stereogenic Center. *Chemistry A European Journal* **2017**, *23*, 6643−6653.

(22) Pollard, M. M.; Meetsma, A.; Feringa, B. L. A Redesign of Light-Driven Rotary Molecular Motors. *Organic & Biomolecular Chemistry* **2008**, *6*, 507−512.

(23) Pollard, M. M.; Wesenhagen, P. V.; Pijper, D.; Feringa, B. L. On the Effect of Donor and Acceptor Substituents on the Behaviour of Light-Driven Rotary Molecular Motors. *Organic & Biomolecular Chemistry* **2008**, *6*, 1605−1612.

(24) Cnossen, A.; Pijper, D.; Kudernac, T.; Pollard, M. M.; Katsonis, N.; Feringa, B. L. A Trimer of Ultrafast Nanomotors: Synthesis, Photochemistry and Self-Assembly on Graphite. *Chemistry (Weinheim an Der Bergstrasse, Germany)* **2009**, *15*, 2768−2772.

(25) Feringa, B. L. In Control of Motion: From Molecular Switches to Molecular Motors. *Acc. Chem. Res.* **2001**, *34*, 504−513.

(26) Bauer, J.; Hou, L.; Kistemaker, J. C. M.; Feringa, B. L. Tuning the Rotation Rate of Light-Driven Molecular Motors. *Journal of Organic Chemistry* **2014**, *79*, 4446−4455.

(27) Mills, G.; Jónsson, H.; Schenter, G. K. Reversible Work Transition State Theory: Application to Dissociative Adsorption of Hydrogen. *Surf. Sci.* **1995**, *324*, 305−337.

(28) Henkelman, G.; Uberuaga, B. P.; Jónsson, H. A Climbing Image Nudged Elastic Band Method for Finding Saddle Points and Minimum Energy Paths. *J. Chem. Phys.* **2000**, *113*, 9901−9904.

(29) Henkelman, G.; Jónsson, H. Improved Tangent Estimate in the Nudged Elastic Band Method for Finding Minimum Energy Paths and Saddle Points. *J. Chem. Phys.* **2000**, *113*, 9978−9985.

(30) Wigner, E. The Transition State Method. *Trans. Faraday Soc.* **1938**, *34*, 29−41.

(31) Vineyard, G. H. Frequency Factors and Isotope Effects in Solid State Rate Processes. *J. Phys. Chem. Solids* **1957**, *3*, 121−127.

(32) Neese, F. The ORCA Program System. *WIREs Computational Molecular Science* **2012**, *2*, 73−78.

(33) Neese, F. Software Update: The ORCA Program System—Version 5.0. *WIREs Computational Molecular Science* **2022**, *12*, e1606.

(34) Ásgeirsson, V.; Birgisson, B. O.; Bjornsson, R.; Becker, U.; Neese, F.; Riplinger, C.; Jónsson, H. Nudged Elastic Band Method for Molecular Reactions Using Energy-Weighted Springs Combined with Eigenvector Following. *J. Chem. Theory Comput.* **2021**, *17*, 4929−4945.

(35) Schmerwitz, Y. L.; Ásgeirsson, V.; Jónsson, H. Improved Initialization of Optimal Path Calculations Using Sequential Traversal over the Image-Dependent Pair Potential Surface. *J. Chem. Theory Comput.* **2024**, *20*, 155−163.

(36) Lee, C.; Yang, W.; Parr, R. G. Development of the Colle-Salvetti Correlation-Energy Formula into a Functional of the Electron Density. *Phys. Rev. B* **1988**, *37*, 785−789.

(37) Becke, A. D. Density-Functional Exchange-Energy Approximation with Correct Asymptotic Behavior. *Phys. Rev. A* **1988**, *38*, 3098−3100.

(38) Becke, A. D. Density-functional Thermochemistry. III. The Role of Exact Exchange. *J. Chem. Phys.* **1993**, *98*, 5648−5652.

(39) Hehre, W. J.; Ditchfield, R.; Pople, J. A. Self-Consistent Molecular Orbital Methods. XII. Further Extensions of Gaussian-Type Basis Sets for Use in Molecular Orbital Studies of Organic Molecules. *J. Chem. Phys.* **1972**, *56*, 2257−2261.

(40) Weigend, F. Accurate Coulomb-fitting Basis Sets for H to Rn. *Phys. Chem. Chem. Phys.* **2006**, *8*, 1057−1065.

(41) Neese, F. An Improvement of the Resolution of the Identity Approximation for the Formation of the Coulomb Matrix. *J. Comput. Chem.* **2003**, *24*, 1740−1747.

(42) Neese, F. The SHARK integral generation and digestion system. *J. Comput. Chem.* **2023**, *44*, 381−396.

(43) Helmich-Paris, B.; de Souza, B.; Neese, F.; Izsák, R. An improved chain of spheres for exchange algorithm. *J. Chem. Phys.* **2021**, *155*, 104109.

(44) Runge, E.; Gross, E. K. U. Density-functional theory for time-dependent systems. *Phys. Rev. Lett.* **1984**, *52*, 997−1000.

(45) Casida, M. *Recent developments and applications of modern density functional theory*; Elsevier: 1996; Vol. *4*; p 391.

(46) Carfora, R.; Coppola, F.; Cimino, P.; Petrone, A.; Rega, N. A Cost-Effective Computational Strategy for the Electronic Layout Characterization of a Second Generation Light-Driven Molecular Rotary Motor in Solution. *J. Comput. Chem.* **2025**, *46*, e70023.

(47) Tambovtsev, I.; Schmerwitz, Y. L. A.; Levi, G.; Darmoroz, D.; Nesterov, P.; Orlova, T.; Jónsson, H. Dataset for the article "Fine Tuning of the Rotational Speed of Light-Driven, Second-generation Molecular Motors by Fluorine Substitution". 2025. DOI: 10.5281/zenodo.10576518.

Paper II

Tuning Molecular Motors with Tert-Butyl and Fluorinated Tert-Butyl Groups

Ivan Tambovtsev and Hannes Jónsson

Accepted for publication in *J. Phys. Chem. A* (in press, 2025). *arXiv:2509.14572*.

Conceived FtBu strategy; performed DFT/NEB/HTST computations and analysis; wrote manuscript draft.

Tuning Molecular Motors with Tert-Butyl and Fluorinated Tert-Butyl Groups

Ivan Tambovtsev* and Hannes Jónsson*

Science Institute and Faculty of Physical Sciences, University of Iceland, 107 Reykjavík, Iceland

E-mail: ivt3@hi.is; hj@hi.is

Abstract

The effect of modifying substituents in the rotor group of five second generation molecular motors is estimated by theoretical calculations. The rotational speed is estimated by calculating the rate limiting step, the thermal helix inversion, as well as the competing backward transition using harmonic transition state theory with energy and atomic forces obtained from density functional theory. First, a methyl group at the stereogenic center is replaced with a tert-butyl (tBu) group and the rotational speed is found to increase due to reduced lifetime of the metastable state. For two of the rotors, comparison can be made with experimental measurements and the calculated half-life is in close agreement. Secondly, the effect of substituting the nine hydrogen atoms in the tBu group with fluorine atoms is studied and this is found to increase the rotational rate further without significantly altering the molecular structure. The excitation wavelength of both the stable and metastable states is calculated and the separation of the absorption peaks is found to increase by the tBu substitution and even more so by the fluorinated tBu substitution, up to 40 nm. These findings can help develop a strategy for designing molecular motors with a rotational speed that best fits a given application.

TOC Graphic

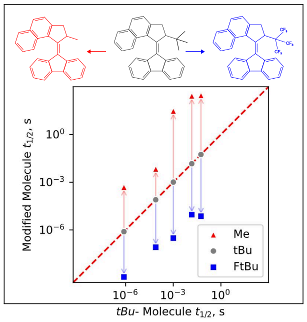

INTRODUCTION

The development of light-powered molecular motors where a part of a molecule undergoes a full rotation relative to the rest has gained significant attention in recent years, with numerous designs demonstrating efficient and directed molecular motion.[1–3] These molecules typically feature a C=C double bond with one side designated as the "rotor" and the other as the "stator". Upon photon absorption, the molecule undergoes an initial 90° rotation in the excited state. Upon relaxation back to the ground state, steric effects drive further rotation to a metastable state. A thermally activated transition, the thermal helix inversion (THI), then drives the molecule to a second stable state corresponding to a rotation of half a circle. Upon absorption of a second photon followed by THI, the full 360° rotation is completed.[4–7]

For efficient unidirectional operation, the rate of the forward THI must be greater than that of the reverse transition back to the stable state, which is referred to as thermal isomerization (TI). When the stator is symmetric, the stable states are structurally equivalent and the directionality is determined solely by the asymmetry of the energy landscape.

Tuning of the rotational rate to an optimal value is important for various applications, for example systems where rotation at the nanoscale is translated into macroscopic actuation, such as in liquid crystalline networks or photonic materials.[8–11] Furthermore, the efficiency is reduced if the metastable state absorbs a photon so a sufficient spacing between the absorption peaks of the stable and metastable states is needed. Extensive efforts have focused on structural modifications that optimize light absorption and enhance the rate of the THI while still ensuring the TI is slow enough.[5,12] Among such modifications is the replacement of hydrogen atoms by fluorine to adjust electronic and steric properties.[13,14]

It has been demonstrated experimentally that fluorination can have contrasting effects: a CF_3 substitution can make rotation faster, while substitution of H by F at the stereogenic center can have the opposite effect, raising the energy barrier for the THI and thereby slowing down the rotation.[15] In a previous computational study, we demonstrated that calculations of minimum energy paths (MEPs) and application of harmonic transition state theory (HTST) with energetics obtained from density functional theory (DFT) give estimates of the thermal rate constants that are in close agreement with experimental data for a wide range of motors.[16] For several rotors we found that substitution of a CH_3 group by a CF_3 group at the stereogenic center accelerates the THI by raising the energy of the metastable state without significantly affecting the transition structure (TS). Targeted fluorination strategies can significantly enhance performance of molecular motors and thereby extend their utility in the various possible applications such as soft robotics, responsive materials, and chiral optics.[17–19]

In the present study, we calculate the effect of substituting a methyl group by a tert-butyl group or a fully fluorinated tert-butyl group. Such structural modifications, examples of which are shown in figure 1, can give control over the rotational speed. The absorption wavelengths of the stable and metastable states are also estimated and the substitutions are found to increase the separation between the absorption peaks, thereby improving efficiency.

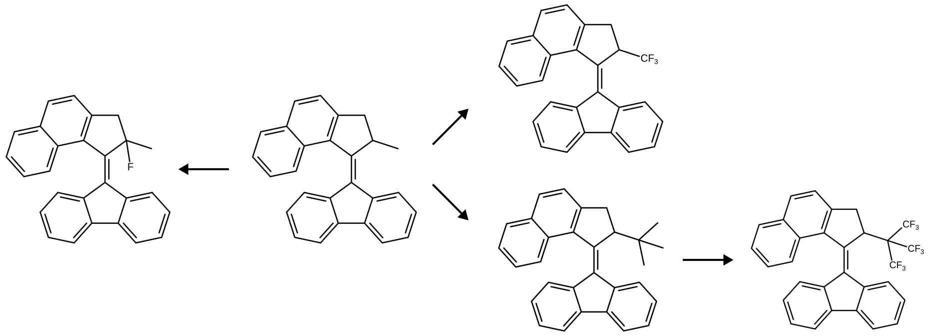

Figure 1: Examples of structural modifications of a second generation molecular motor. Starting from the methyl-substituted rotor (center), the molecule is modified either by fluorination of the stereogenic center (left), substitution of the methyl group with a trifluoromethyl group (top), replacement of the methyl group with a tert-butyl group (bottom-left), and full fluorination of the tert-butyl group (bottom-right).

METHODS

The minimum energy path for the THI and TI transitions from the metastable state is calculated using the climbing image nudged elastic band (CI-NEB) method,[20–22] as implemented in the ORCA software[23,24] using energy weighted springs.[25] The initial path is generated using the sequential image dependent pair potential (S-IDPP) method.[26] The locations of the images along the path are converged to a tolerance of $2.5 \cdot 10^{-3}$ au and $5 \cdot 10^{-3}$ au in the RMS and MAX of the force perpendicular to the local tangent to the path, respectively, with one order of magnitude tighter tolerance on the climbing image. CI-NEB is followed by a first-order saddle point search (SPS) with the CI as the initial guess,[25] and is converged to a tolerance of $5 \cdot 10^{-6}$ au, $3 \cdot 10^{-4}$ au, 10^{-4} au, $4 \cdot 10^{-3}$ au, and $2 \cdot 10^{-3}$ au for the switch from CI-NEB to SPS, the MAX and RMS of the gradient, and the MAX and RMS of the optimization step, respectively.

The DFT calculations make use of the B3LYP hybrid functional approximation[27–29] and a linear combination of atomic orbitals with the 6-31G(d,p) basis set.[30,31] The B3LYP functional is chosen for its proven performance in a wide range of molecular systems, and the 6-31G(d,p) basis set is selected for its balance between computational efficiency and accuracy. The structure of the stable and metastable states of all molecular motors is optimized to a tolerance of 10^{-4} au, $3 \cdot 10^{-4}$ au, $2 \cdot 10^{-3}$ au, and $4 \cdot 10^{-3}$ au for the RMS and MAX of the gradient and the RMS and MAX of the optimization step, respectively. Atom coordinates of the local minima and TS as well as scripts specifying tolerances are provided in the data stored and openly provided on Zenodo.

The rate constants for the THI and TI are calculated using the harmonic approximation to transition state theory[32,33]

$$k_{\mathrm{HTST}} = \frac{\prod_i^{3N} \nu_i^{\mathrm{min}}}{\prod_i^{3N-1} \nu_i^{\ddagger}} \exp\left[-\left(E^{\ddagger} - E^{\mathrm{min}}\right)/k_{\mathrm{B}}T\right], \tag{1}$$

where ν_i^{min} and $\nu_i^{\ddagger}$ refer to vibrational frequency, and E^{min} and $E^{\ddagger}$ refer to the energy of the initial state minimum and first order saddle point, respectively. The vibrational analysis is furthermore used to confirm that the stable and metastable structures are local minima on the energy surface and the TSs correspond to first-order saddle points. The half-life of the metastable state is obtained from the THI rate constant as $\tau = \ln 2/k_{\mathrm{HTST}}$. Since the rate of the TI turns out to be so much smaller than the THI, its effect can be neglected in the half-life calculation.

The absorption wavelengths are obtained with linear-response TDDFT within the adiabatic approximation. All calculations are performed with the ORCA 5 software.[23,24] The data was extracted using ChemParse.

RESULTS AND DISCUSSION

To assess the impact of structural modifications on the rotational rate of second-generation molecular motors, we selected a set of five well-characterized base molecules, illustrated in figure 2. They are representative of the common second-generation motor designs, featuring a five-membered ring in the rotor connected to a fluorene stator by a C=C double bond. They have all been synthesized and experimentally studied,[4,34–37] and were chosen for this study because they exhibit a diverse range of structural features and rotational properties, providing a basis for evaluating systematic trends in the effect of modifications. For each of these five base molecules, illustrated in figure 2, three variants at the substitution site X were studied: the original methyl group (CH_3), a tert-butyl group (tBu), and a fully fluorinated tert-butyl group (FtBu).

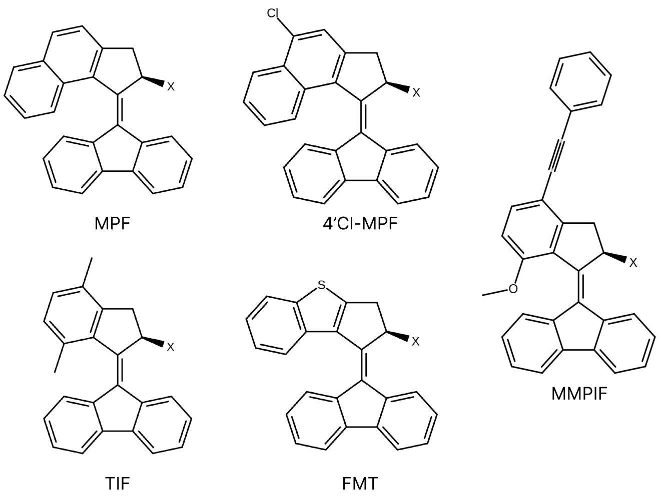

Figure 2: The molecular motors investigated in the present study to assess the effect of modifications at site X. In the base molecules, X is a CH_3 group (methyl), while in the modified molecules, X is replaced by a tert-butyl or fluorinated tert-butyl group.

Figure 3(a) illustrates the calculated half-life of the metastable state of the rotors with methyl, tBu and FtBu at site X. The changes in the half-life are presented in a way that the rotors start with tBu and this group is then replaced by methyl or FtBu. The effect of the substitutions is in the same direction for all five rotors. The methyl group gives the longest half-life and thereby slowest rotation, while the FtBu gives the shortest half-life and fastest rotation. In all cases, the back transition, TI, is slower than the THI. The calculated values of the half-life as well as the rate constants are given in table 1. For two of the tBu molecular motors, experimentally determined values of the half-life have been reported [34,38] and our calculated values are in close agreement, within a factor of three: 5.7×10^{-3} s vs. 1.46×10^{-2} s for tBu−MPF, and 2.6×10^{-3} s vs. 1.0×10^{-3} s for tBu−TIF.

Fluorination of the tBu group to form FtBu does not significantly alter the molecular structure compared to the tBu analogues. The acceleration of the rotation arises from increased steric hindrance by the fluorine atoms in the stable and metastable states. Figure 3(b) shows the calculated MEP for rotors tBu−MPF and FtBu−MPF. Clearly, the activation energy for the THI is reduced when tBu is replaced by FtBu and the rotational speed thereby increased.

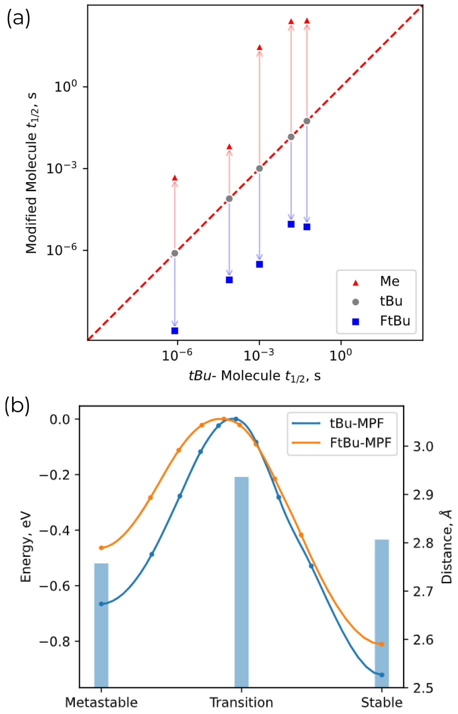

Figure 3: (a) Calculated half-life of the metastable state of the molecular motors and the effect of substituting the tert-butyl (tBu) group at site X with either a methyl group, Me (red) or a fully fluorinated tert-butyl group, FtBu (blue). The FtBu substitution consistently increases the forward rotation rate, while the Me substitution decreases it. (b) Minimum energy paths for the THI of tBu−MPF and FtBu−MPF. The zero of energy is set to that of the transition structure, TS. The bars and corresponding axis to the right show the average distance between the hydrogen atoms in the tBu group on the rotor of tBu−MPF to atoms in the stator that are within 2.9 Å in the stable, TS, and metastable state. This serves as a measure of the steric hindrance, which is smaller in the TS than in the stable and metastable states. The substitution of tBu by FtBu thereby reduces the energy barrier for the THI.

Table 1: Absorption wavelengths for the stable and metastable isomers, corresponding to the excitation that triggers photoinduced rotation, calculated rate constants for the forward (THI) and backward (TI) thermal reactions, and the corresponding theoretical and experimental half-lives.

Molecule	$\lambda_{\textbf{stable}}$, **nm**	$\lambda_{\textbf{meta}}$, **nm**	k^{THI}, s^{-1}	k^{TI}, s^{-1}	$t_{1/2}$, s	$t_{1/2}^{Exp}$, s
MPF	379	410	2.60×10^{-3}	8.34×10^{-4}	2.02×10^{2}	1.90×10^{2} [34]
tBu−MPF	371	437	4.75×10^{1}	7.99×10^{-3}	1.46×10^{-2}	5.73×10^{-3} [34]
FtBu−MPF	368	442	7.59×10^{4}	6.26×10^{4}	5.00×10^{-6}	-
TIF	340	367	2.32×10^{-2}	7.93×10^{-7}	2.99×10^{1}	1.50×10^{1} [35]
tBu−TIF	336	395	6.85×10^{2}	2.61×10^{-3}	1.01×10^{-3}	2.90×10^{-3} [39]
FtBu−TIF	332	405	2.24×10^{6}	1.09×10^{-1}	3.09×10^{-7}	-
4′Cl−MPF	388	419	2.44×10^{-3}	1.84×10^{-3}	1.62×10^{2}	2.88×10^{2} [36]
tBu−4′Cl−MPF	380	446	1.25×10^{1}	1.68×10^{-2}	5.54×10^{-2}	-
FtBu−4′Cl−MPF	372	454	9.52×10^{4}	4.39×10^{-1}	7.28×10^{-6}	-
MMPIF	349	389	1.42×10^{3}	8.78×10^{-6}	4.88×10^{-4}	1.60×10^{-4} [37]
tBu−MMPIF	345	394	8.83×10^{5}	5.54×10^{-5}	7.85×10^{-7}	-
FtBu−MMPIF	334	399	6.22×10^{8}	5.21×10^{-4}	1.11×10^{-9}	-
FMT	347	365	1.02×10^{2}	1.12×10^{-6}	6.80×10^{-3}	7.00×10^{-2} [4]
tBu−FMT	345	384	8.80×10^{3}	3.04×10^{-6}	7.88×10^{-5}	-
FtBu−FMT	347	397	8.39×10^{6}	2.18×10^{-3}	8.26×10^{-8}	-

To better understand the origin of this acceleration, the molecular structure along the MEPs is analyzed by focusing on the steric interactions between the rotor and stator. Specifically, we use the same metric as in our previous studies of fluorination:[16] the average distance between the hydrogen atoms of the rotor in the tBu group and the atoms of the stator that lie within 2.9 Å, which corresponds to the sum of the van der Waals radii for carbon and hydrogen atoms. This serves as an indicator of steric hindrance. Figure 3(b) illustrates the value of this average distance for the stable, TS and metastable states. The TS turns out to have the largest value and thereby smaller steric hindrance, while the metastable state has the smallest value and largest steric hindrance. The replacement of tBu with FtBu therefore raises the energy of the metastable state more than the TS, and thereby lowers the energy barrier for the THI.

Table 2: Average rotor–stator proximity (in Å) for tBu-substituted motors in stable state, transition structure and metastable state.

Molecule	$\bar{d}_{\text{stable}}$	$\bar{d}_{\text{TS}}$	$\bar{d}_{\text{meta}}$
tBu−MPF	2.81	2.94	2.76
tBu−TIF	2.82	2.89	2.74
tBu−4′Cl−MPF	2.82	2.91	2.75
tBu−MMPIF	2.78	2.83	2.78
tBu−FMT	2.61	2.84	2.73

Table 2 shows the value of this measure of steric hindrance for all five tBu-substituted molecules. The same trend is seen. This measure of the average rotor–stator distance is relatively larger in the TS and shortest in the metastable state, indicating that steric hindrance is more pronounced there. As a result, after the replacement of the hydrogen atoms in the tBu group with fluorine, the energy of the metastable state is increased relative to the TS.

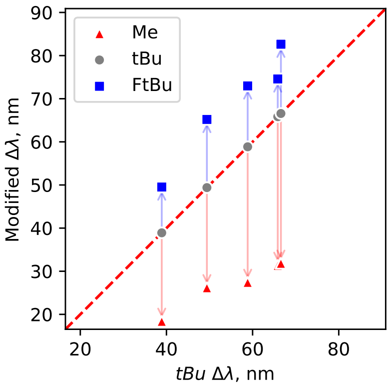

Figure 4: Calculated difference in the excitation wavelength of the stable and metastable states, $\Delta\lambda$, for the five motors with the various substituents. The methyl-substituted motors, Me, consistently give the smallest gaps (red), tert-butyl, tBu, increases the separation (gray), and fully fluorinated tert-butyl, FtBu, increases the gap even further (blue).

Figure 4 illustrates the difference in the absorption wavelength of the metastable and stable states, $\Delta\lambda$, when the tBu is replaced by methyl or FtBu. The results reveal a systematic trend: the rotors with the methyl group have the smallest gap, those with tBu have a larger gap by 20 to 30 nm, and the largest gap is obtained for the rotors with FtBu, increased by as much as 42 nm compared with rotors where a methyl group is at the X site. This increasing spectral separation enhances selective photoactivation by minimizing the risk of unwanted photoreversal that can occur if the metastable state is excited. The complete set of calculated absorption wavelengths is provided in Table 1).

CONCLUSIONS

The substitution of a methyl group with a tBu group or a FtBu group at the stereogenic center of five second generation molecular motors is found to increase the rotational speed as well as the separation of the absorption peaks for the stable and metastable states. The trend is the same for all the rotors and the FtBu substitution gives a larger effect than the tBu substitution. The reason for the increased rotational speed is larger steric hindrance in the metastable state than in the transition structure and thereby lower energy barrier for the THI. Where experimental data is available, the agreement with the calculations presented here based on calculations of the MEP and rates using HTST with energetics coming from DFT/B3LYP is good. The calculations are expected to have a predictive value and can be used to guide the fine tuning of rotor molecules.

Acknowledgement

This work was funded by the Icelandic Research Fund (grants 239970 and 2511544). We thank Gianluca Levi for helpful discussions. The calculations were carried out at the IREI HPC facility at the University of Iceland.

Data Availability Statement

The data supporting the findings of this work are available for download at Zenodo.

References

(1) Corra, S.; Curcio, M.; Credi, A. Photoactivated Artificial Molecular Motors. *JACS Au* **2023**, *3*, 1301–1313.

(2) Baroncini, M.; Silvi, S.; Credi, A. Photo- and Redox-Driven Artificial Molecular Motors. *Chemical Reviews* **2020**, *120*, 200–268.

(3) Jeong, M.; Park, J.; Kwon, S. Molecular Switches and Motors Powered by Orthogonal Stimuli. *European Journal of Organic Chemistry* **2020**, *2020*, 7254–7283.

(4) García-López, V.; Liu, D.; Tour, J. M. Light-Activated Organic Molecular Motors and Their Applications. *Chemical Reviews* **2020**, *120*, 79–124.

(5) Pooler, D. R. S.; Lubbe, A. S.; Crespi, S.; Feringa, B. L. Designing Light-Driven Rotary Molecular Motors. *Chemical Science* **2021**, *12*, 14964–14986.

(6) Roke, D.; Wezenberg, S. J.; Feringa, B. L. Molecular Rotary Motors: Unidirectional Motion around Double Bonds. *Proceedings of the National Academy of Sciences of the United States of America* **2018**, *115*, 9423–9431.

(7) Koumura, N.; Zijlstra, R. W. J.; van Delden, R. A.; Harada, N.; Feringa, B. L. Light-Driven Monodirectional Molecular Rotor. *Nature* **1999**, *401*, 152–155.

(8) Hou, J.; Long, G.; Zhao, W.; Zhou, G.; Liu, D.; Broer, D. J.; Feringa, B. L.; Chen, J. Phototriggered Complex Motion by Programmable Construction of Light-Driven Molecular Motors in Liquid Crystal Networks. *Journal of the American Chemical Society* **2022**, *144*, 6851–6860.

(9) Lan, R.; Bao, J.; Huang, R.; Wang, Z.; Zhang, L.; Shen, C.; Wang, Q.; Yang, H. Amplifying Molecular Scale Rotary Motion: The Marriage of Overcrowded Alkene Molecular Motor with Liquid Crystals. *Advanced Materials* **2022**, *34*, 2109800.

(10) Hou, J.; Mondal, A.; Long, G.; de Haan, L.; Zhao, W.; Zhou, G.; Liu, D.; Broer, D. J.; Chen, J.; Feringa, B. L. Photo-Responsive Helical Motion by Light-Driven Molecular Motors in a Liquid-Crystal Network. *Angewandte Chemie International Edition* **2021**, *60*, 8251–8257.

(11) Sun, J.; Hu, W.; Zhang, L.; Lan, R.; Yang, H.; Yang, D.-K. Light-Driven Self-Oscillating Behavior of Liquid-Crystalline Networks Triggered by Dynamic Isomerization of Molecular Motors. *Advanced Functional Materials* **2021**, *31*, 2103311.

(12) Vicario, J.; Meetsma, A.; Feringa, B. L. Controlling the Speed of Rotation in Molecular Motors. Dramatic Acceleration of the Rotary Motion by Structural Modification. *Chemical Communications* **2005**, 5910–5912.

(13) Huang, H.; Orlova, T.; Matt, B.; Katsonis, N. Long-Lived Supramolecular Helices Promoted by Fluorinated Photoswitches. *Macromolecular Rapid Communications* **2018**, *39*, 1700387.

(14) Bléger, D.; Schwarz, J.; Brouwer, A. M.; Hecht, S. O-Fluoroazobenzenes as Readily Synthesized Photoswitches Offering Nearly Quantitative Two-Way Isomerization with Visible Light. *Journal of the American Chemical Society* **2012**, *134*, 20597–20600.

(15) Štacko, P.; Kistemaker, J. C. M.; Feringa, B. L. Fluorine-Substituted Molecular Motors with a Quaternary Stereogenic Center. *Chemistry – A European Journal* **2017**, *23*, 6643–6653.

(16) Tambovtsev, I.; Schmerwitz, Y. L. A.; Levi, G.; Darmoroz, D. D.; Nesterov, P. V.; Orlova, T.; Jónsson, H. Fine Tuning of the Rotational Speed of Light-Driven, Second-Generation Molecular Motors by Fluorine Substitution. *The Journal of Physical Chemistry Letters* **2025**, 4014–4020.

(17) Yang, F.; Yue, B.; Zhu, L. Light-Triggered Modulation of Supramolecular Chirality. *Chemistry – A European Journal* **2023**, *29*, e202203794.

(18) Kim, Y.; Tamaoki, N. Photoresponsive Chiral Dopants: Light-Driven Helicity Manipulation in Cholesteric Liquid Crystals for Optical and Mechanical Functions. *ChemPhotoChem* **2019**, *3*, 284–303.

(19) Orlova, T.; Lancia, F.; Loussert, C.; Iamsaard, S.; Katsonis, N.; Brasselet, E. Revolving Supramolecular Chiral Structures Powered by Light in Nanomotor-Doped Liquid Crystals. *Nature Nanotechnology* **2018**, *13*, 304–308.

(20) Mills, G.; Jónsson, H.; Schenter, G. K. Reversible Work Transition State Theory: Application to Dissociative Adsorption of Hydrogen. *Surface Science* **1995**, *324*, 305–337.

(21) Henkelman, G.; Uberuaga, B. P.; Jónsson, H. A Climbing Image Nudged Elastic Band Method for Finding Saddle Points and Minimum Energy Paths. *The Journal of Chemical Physics* **2000**, *113*, 9901–9904.

(22) Henkelman, G.; Jónsson, H. Improved Tangent Estimate in the Nudged Elastic Band Method for Finding Minimum Energy Paths and Saddle Points. *The Journal of Chemical Physics* **2000**, *113*, 9978–9985.

(23) Neese, F. The ORCA Program System. *WIREs Computational Molecular Science* **2012**, *2*, 73–78.

(24) Neese, F. Software Update: The ORCA Program System—Version 5.0. *WIREs Computational Molecular Science* **2022**, *12*, e1606.

(25) Ásgeirsson, V.; Birgisson, B. O.; Bjornsson, R.; Becker, U.; Neese, F.; Riplinger, C.; Jónsson, H. Nudged Elastic Band Method for Molecular Reactions Using Energy-Weighted Springs Combined with Eigenvector Following. *Journal of Chemical Theory and Computation* **2021**, *17*, 4929–4945.

(26) Schmerwitz, Y. L. A.; Urgell Ollé, N.; Levi, G.; Jónsson, H. Saddle Point Search Algorithms for Variational Density Functional Calculations of Excited Electronic States

with Self-Interaction Correction. Proceedings of the Platform for Advanced Scientific Computing Conference. Zurich Switzerland, 2024; pp 1–11.

(27) Lee, C.; Yang, W.; Parr, R. G. Development of the Colle-Salvetti Correlation-Energy Formula into a Functional of the Electron Density. *Physical Review B* **1988**, *37*, 785–789.

(28) Becke, A. D. Density-Functional Exchange-Energy Approximation with Correct Asymptotic Behavior. *Physical Review A* **1988**, *38*, 3098–3100.

(29) Becke, A. D. Density-functional Thermochemistry. III. The Role of Exact Exchange. *The Journal of Chemical Physics* **1993**, *98*, 5648–5652.

(30) Hehre, W. J.; Ditchfield, R.; Pople, J. A. Self—Consistent Molecular Orbital Methods. XII. Further Extensions of Gaussian—Type Basis Sets for Use in Molecular Orbital Studies of Organic Molecules. *The Journal of Chemical Physics* **2003**, *56*, 2257–2261.

(31) Weigend, F. Accurate Coulomb-fitting Basis Sets for H to Rn. *Physical Chemistry Chemical Physics* **2006**, *8*, 1057–1065.

(32) Wigner, E. The Transition State Method. *Transactions of the Faraday Society* **1938**, *34*, 29–41.

(33) Vineyard, G. H. Frequency Factors and Isotope Effects in Solid State Rate Processes. *Journal of Physics and Chemistry of Solids* **1957**, *3*, 121–127.

(34) Vicario, J.; Walko, M.; Meetsma, A.; Feringa, B. L. Fine Tuning of the Rotary Motion by Structural Modification in Light-Driven Unidirectional Molecular Motors. *Journal of the American Chemical Society* **2006**, *128*, 5127–5135.

(35) Pollard, M. M.; Meetsma, A.; Feringa, B. L. A Redesign of Light-Driven Rotary Molecular Motors. *Organic & Biomolecular Chemistry* **2008**, *6*, 507–512.

(36) Pollard, M. M.; Wesenhagen, P. V.; Pijper, D.; Feringa, B. L. On the Effect of Donor and Acceptor Substituents on the Behaviour of Light-Driven Rotary Molecular Motors. *Organic & Biomolecular Chemistry* **2008**, *6*, 1605–1612.

(37) Cnossen, A.; Pijper, D.; Kudernac, T.; Pollard, M. M.; Katsonis, N.; Feringa, B. L. A Trimer of Ultrafast Nanomotors: Synthesis, Photochemistry and Self-Assembly on Graphite. *Chemistry (Weinheim an Der Bergstrasse, Germany)* **2009**, *15*, 2768–2772.

(38) Pollard, M. M.; Klok, M.; Pijper, D.; Feringa, B. L. Rate Acceleration of Light-Driven Rotary Molecular Motors. *Advanced Functional Materials* **2007**, *17*, 718–729.

(39) Bauer, J.; Hou, L.; Kistemaker, J. C. M.; Feringa, B. L. Tuning the Rotation Rate of Light-Driven Molecular Motors. *The Journal of Organic Chemistry* **2014**, *79*, 4446–4455.

Paper III

The Effect of Chlorine Substitution on Rotational Speed and Light Absorption of Second Generation Molecular Motors

Ivan Tambovtsev, Oskar Kristinsson, and Hannes Jónsson

Manuscript submitted, *arXiv:2510.08165* (2025)

Co-developed study; performed selected calculations; set up workflows and mentored O. Kristinsson; contributed analysis and writing.

The Effect of Chlorine Substitution on Rotational Speed and Light Absorption of Second Generation Molecular Motors

Ivan Tambovtsev,* Óskar Kristinsson,* and Hannes Jónsson*

Science Institute and Faculty of Physical Sciences, University of Iceland, 107 Reykjavík, Iceland

E-mail: ivt3@hi.is; oskarkristinsson@mailbox.org; hj@hi.is

Abstract

The effect of substituting a methyl group by a trichloromethyl (CCl_3) group at the stereogenic center of light-driven second generation molecular motors is calculated in order to assess the effect on rotational speed and the separation of the absorption peaks of the stable and metastable isomers. While experimental and theoretical studies have previously been carried out for fluorine substitution, this is the first study of chlorine substitution in the form of a CCl_3 group at this site. Five well-characterized base molecules are studied and the trends are compared with the effect of fluorine substitution. The trichloromethyl substitution is found to accelerate the rotation more than a trifluoromethyl (CF_3) substitution by reducing the life-time of the metastable state, due to larger steric hindrance in the metastable state than in the transition state for the thermal helix inversion (THI). A larger increase in the separation of the absorption peaks of the two isomers is also obtained.

Introduction

Nature's molecular motors, refined over millions of years of evolution, provide inspiration for the design of synthetic molecular machines, and this has been an active field of research in the past couple of decades.[1] Possible applications are in various fields, such as optics, photonics and light-driven soft materials. Second generation molecular motors are characterized by a central C=C double bond that connects a "rotor" part of the molecule to a "stator" part and rotates half a circle for each photon absorbed.

In the conventional operating cycle,[2] the molecule starts from the stable isomer and, upon absorption of a photon, undergoes a ca. 90° rotation in the excited state followed by a further rotation in the ground state to the higher-energy, metastable isomer.[3,4]

This photogenerated state is the crucial intermediate from which two competing thermally activated transitions determine the molecule's ultimate function. If the molecule undergoes a conformational change corresponding to completion of the first half of the rotation, the so-called thermal helix inversion (THI), a repeat of these steps after absorption of a second photon completes a full cycle of the motor. If, however, the preferred thermally activated transition from the metastable state is a backward transition to the original isomer, the so-called thermal isomerization (TI), the molecule does not rotate, but could function as a thermally reversible (T-type) molecular switch.[5] The ultimate performance and role of the molecule is, therefore, affected by the competition between the THI and TI transitions in the ground electronic state.

Optimization of the rotational speed is a critical aspect of molecular motor design, as the ideal frequency is highly application-dependent. High speeds are sought for soft actuators and drug delivery systems that rely on rapid mechanical work,[6–8] whereas slow rotation is required for applications such as catalysis, where a specific isomeric state may be used for stereochemical control.[9] In other systems, function emerges from a precisely controlled dynamic interplay, as seen in the formation of revolving structures in liquid crystals.[10] For second-generation motors, a wide variety of designs with different rotational speeds have been developed to meet these diverse demands.[11] The speed can be altered through major changes in the molecular geometry, such as replacing a six-membered ring in the rotor with a five-membered one,[12] but one way of fine-tuning that only weakly affects the molecular structure is, for example, fluorine substitution.[13–16]

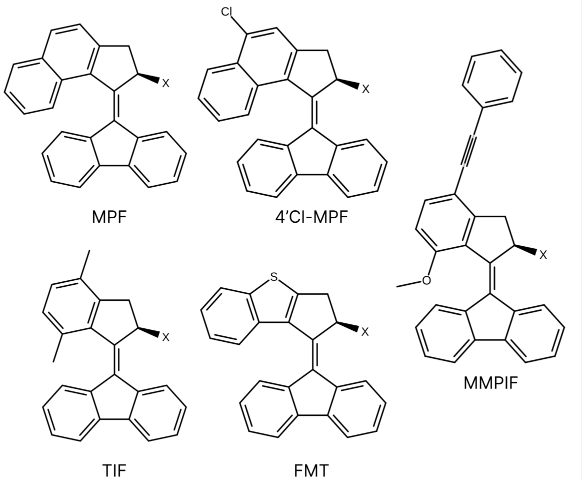

Figure 1: The second-generation molecular motors studied here with substitutional site marked with an X. The modification considered in the main text is Me → CCl_3 at site X (stereogenic center).

Here, we study the effect of substituting the methyl group at the stereogenic center by a CCl_3 group on the properties of the set of five second-generation molecular motors shown in Figure 1. These molecules are representative of the common second-generation motor designs, featuring a fluorene stator and a five-membered ring in the rotor connected by a central C=C double bond. They have been previously synthesized and experimentally studied,[17–21] and were chosen for this study because they exhibit a diverse range of structural features and rotational properties, providing a robust basis for evaluating the effect of modifications in a systematic way.

The effect of replacing the methyl group at site X with a trichloromethyl (CCl_3) group is calculated. The effect of replacing the hydrogen atom at the same stereogenic center by chlorine (H→Cl) is discussed in the Supporting Information.

The results are compared with previously reported effects of fluorine substitutions.[16] The separation between the absorption peaks of the two isomers is also calculated since a large enough gap is important for selectively driving the rotation.

Results and Discussion

Figure 2 shows the stable and metastable isomers as well as the THI and TI transition structures (corresponding to first order saddle points on the energy surface) for molecule CCl_3−MPF.

The steric interactions at the stereogenic center, in particular at the metastable isomer and the two transition structures, are critical in determining the rotational speed as discussed below.

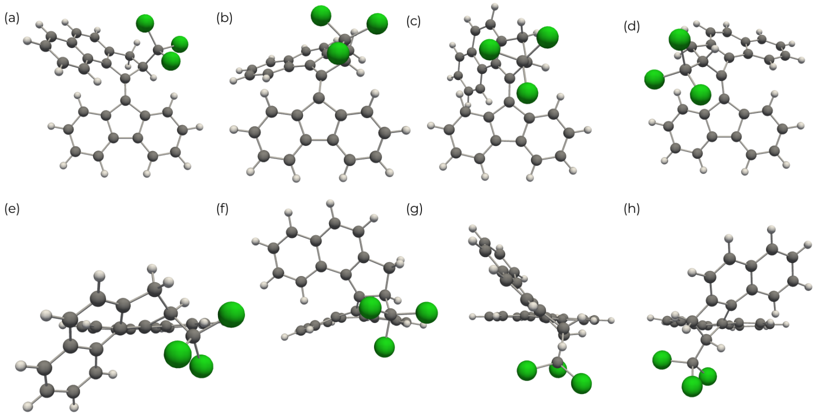

Figure 2: Front and top views of the optimized structures for the various states of molecule CCl_3−MPF. (a and e) The stable isomer. (b and f) The transition structure for the forward thermal helix inversion, THI. (c and g) The metastable isomer. (d and h) The transition structure for the backward thermal isomerization, TI.

Figure 3 shows the calculated minimum energy paths (MEPs) for the THI and TI transitions of the five base molecules as well as the CCl_3 substituted variants. The replacement of the methyl group by a CCl_3 group consistently lowers the energy barrier for both transitions. The calculated rate constants are changed accordingly, the one for THI increasing by two to five orders of magnitude (see Table 1). This translates to a significant shortening of the lifetime of the metastable state and a corresponding increase in the rotational speed. In all cases, the forward THI continues to have a lower energy barrier than TI so the molecules still function as molecular motors. Figure 4 illustrates the change in the calculated half-life of the metastable state.

Table 1: Absorption wavelengths (in nm) for the two isomers and calculated rate constants (in s^{-1}) for the forward (THI) and backward (TI) thermal transitions at 298 K. Note that the rate constants are for transitions from the higher energy, metastable isomer in each case.

Molecule	$\lambda_{\textbf{Stable}}$	$\lambda_{\textbf{Metastable}}$	k^{THI}	k^{TI}
MPF	379	410	2.58×10^{-3}	8.23×10^{-4}
CCl_3−MPF	381	436	1.38×10^{2}	7.07×10^{0}
4'Cl−MPF	388	420	2.01×10^{-3}	1.74×10^{-3}
CCl_3−4'Cl−MPF	386	443	1.24×10^{2}	5.38×10^{-2}
FMT	347	365	1.01×10^{2}	1.13×10^{-6}
CCl_3−FMT	362	393	7.28×10^{4}	5.85×10^{-3}
MMPIF	349	389	1.42×10^{3}	8.78×10^{-6}
CCl_3−MMPIF	347	426	2.67×10^{6}	3.68×10^{-2}
TIF	340	367	2.32×10^{-2}	7.93×10^{-7}
CCl_3−TIF	346	398	2.28×10^{3}	3.53×10^{0}

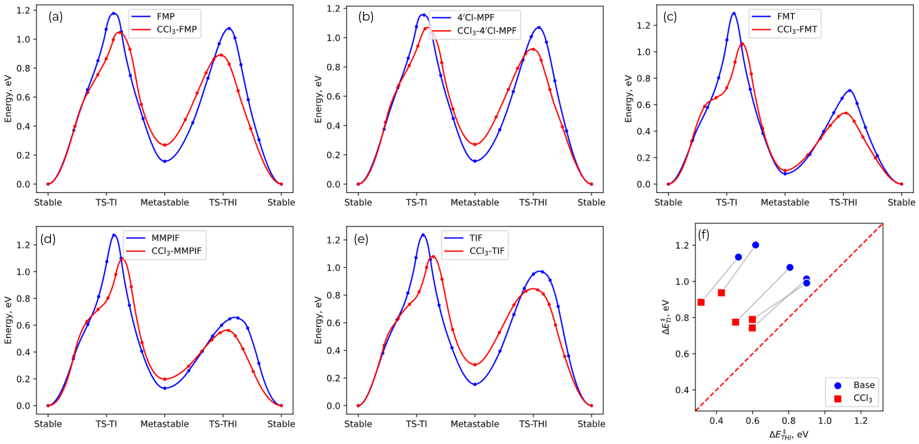

Figure 3: (a-e) Minimum energy paths between the stable and metastable isomers of the five base molecules where a methyl group and a hydrogen atom are at the X site (blue), as well as the corresponding molecules with the methyl group substituted for a CCl_3 group (red). Energies are referenced to the stable isomer in each case. The energy maxima correspond to first order saddle points, i.e. transition structures, for the TI (left) and THI (right) transitions. For the CCl_3 substitution, both energy barriers decrease and the THI barrier continues to be lower than that for TI. (f) Activation energy for the TI and THI transitions from the metastable state for the base (blue) and CCl_3 substituted (red) molecules (corresponding pairs are connected).

Figure 4 illustrates the calculated half-life of the metastable state of the molecules that can function as molecular motors (with Me, F, CF_3, or CCl_3 at the X site). The half-life is dominated by the rate of the forward THI step. The shorter the half-life is, the faster the rotation. The CCl_3 substitution leads to a dramatic shortening of the half-life, in a more pronounced way than was previously reported for CF_3 substitution.[16] The calculated rate constants, listed in Table 1, show that the forward THI process continues to be the dominant thermal pathway, faster than TI, and thus leading to unidirectional rotation.

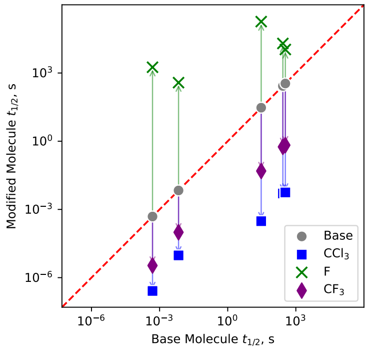

Figure 4: Comparison of the half-life of the metastable isomer of the molecules. The substitution of the methyl group for a CCl_3 group (blue) shortens the half-life and thereby increases the rotational speed, more so than the previously reported substitution by a CF_3 group. Data on fluorine and CF_3 substitution are from Ref. 16.

Figure 5 illustrates the difference in the calculated absorption wavelengths for the two isomers. A clear and advantageous trend emerges for the CCl_3 substitution. For all the molecules, the CCl_3 substitution consistently gives the largest gap between the absorption peaks of the two isomers. This large spectral separation is a significant practical advantage, as it makes it easier to selectively drive the motor cycle by photoactivation.

The spectroscopic and kinetic consequences of H→Cl at the same stereogenic center are discussed in the Supporting Information.

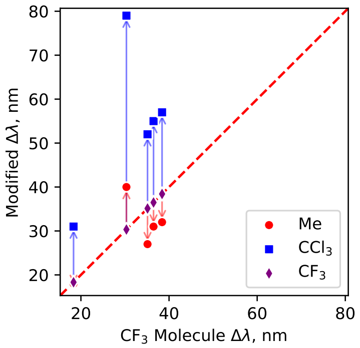

Figure 5: Difference in excitation wavelength, $\Delta\lambda$, of the two isomers of the molecules with methyl (red), CCl_3 (blue) and CF_3 (purple)[16] groups at the stereogenic center. The substitution of the methyl for CCl_3 consistently increases the gap and thereby would improve selectivity in the photoexcitation.

Conclusion

In summary, the effect of Me → CCl_3 substitution at the stereogenic center of second generation molecular motors is explored by theoretical calculations. The results show that a methyl to CCl_3 substitution at the stereogenic center will increase the speed of rotation and also improve spectroscopic properties for selective activation, more so than the previously studied CF_3 substitution. The effect of replacing the hydrogen atom at the same stereogenic center by chlorine (H→Cl), which leads to a qualitative change in the ground-state landscape, is discussed in the Supporting Information.

Methods

The minimum energy paths (MEPs) for the THI and TI transitions were calculated using the climbing image nudged elastic band (CI-NEB) method,[22–24] using energy-weighted springs[25] as implemented in the ORCA software,.[26] The initial path was generated using the sequential image dependent pair potential (S-IDPP) method.[27] The position of each image on the path was converged to a tolerance of $2.5 \cdot 10^{-3}$ a.u. (RMS) and $5 \cdot 10^{-3}$ a.u. (MAX) for the force perpendicular to the local tangent, with one order of magnitude tighter tolerance for the climbing image. The climbing image was then made to converge fully on the first order saddle point using a saddle point search method[25] until the atomic forces had dropped below 10^{-4} a.u. (RMS) and $3 \cdot 10^{-4}$ a.u. (MAX).

The DFT calculations were carried out using the B3LYP hybrid functional approximation[28–30] and a linear combination of atomic orbitals formalism employing the 6-31G(d,p) basis set.[31,32] The B3LYP functional is chosen for its proven performance in a wide range of molecular systems, and the 6-31G(d,p) basis set is selected for its balance between computational efficiency and accuracy.

The ground state electronic structure calculations were converged to thresholds of 10^{-7} a.u. for the maximum component of the density change, $5 \cdot 10^{-9}$ a.u. for the root mean square (RMS) of the density change, and $5 \cdot 10^{-7}$ a.u. for the error in the direct inversion in the iterative subspace (DIIS). The structure of the stable and metastable states of all molecular motors were optimized to a tolerance of 10^{-4} a.u. (RMS) and $3 \cdot 10^{-4}$ a.u. (MAX) for the gradient, and $2 \cdot 10^{-3}$ a.u. (RMS) and $4 \cdot 10^{-3}$ a.u. (MAX) for the optimization step.

The rate constant for thermally activated transitions was calculated using the harmonic approximation to transition state theory (HTST),[33,34]

$$k_{\mathrm{HTST}} = \frac{\prod_i^{3N} \nu_i^{\mathrm{min}}}{\prod_i^{3N-1} \nu_i^{\ddagger}} \exp\left[-\frac{E^{\ddagger} - E^{\mathrm{min}}}{k_{\mathrm{B}}T}\right], \tag{1}$$

where ν_i^{min} and $\nu_i^{\ddagger}$ refer to vibrational frequencies at the minimum and first-order saddle point, respectively, and E^{min} and $E^{\ddagger}$ denote the corresponding values of the energy (zero point energy corrections included). The overall half-life of the metastable isomers was calculated as $t_{1/2} = \ln 2/(k_{\mathrm{THI}} + k_{\mathrm{TI}})$. The methodology described above for estimating the half-life of the metastable isomer has previously been tested and found to give results in close agreement with experimental measurements for a wide range of molecular motors.[16]

The spectra were calculated using linear-response TDDFT within the adiabatic approximation. All calculations were performed with the ORCA 6.1 software.[26] The data was extracted using ChemParse.

Acknowledgement

This work was funded by the Icelandic Research Fund (grants 239970 and 2511544). We thank Tetiana Orlova and Gianluca Levi for helpful discussions. The calculations were carried out at the IREI HPC facility at the University of Iceland.

Data Availability Statement

The data supporting the findings of this work are available for download at Zenodo.

References

(1) Feringa, B. L. The Art of Building Small: From Molecular Switches to Motors (Nobel Lecture). *Angewandte Chemie International Edition* **2017**, *56*, 11060–11078.

(2) Roke, D.; Wezenberg, S. J.; Feringa, B. L. Molecular Rotary Motors: Unidirectional Motion around Double Bonds. *Proceedings of the National Academy of Sciences of the United States of America* **2018**, *115*, 9423–9431.

(3) Gold, V., Ed. *The IUPAC Compendium of Chemical Terminology: The Gold Book*, 4th ed.; International Union of Pure and Applied Chemistry (IUPAC): Research Triangle Park, NC, 2019.

(4) Koumura, N.; Geertsema, E. M.; van Gelder, M. B.; Meetsma, A.; Feringa, B. L. Second Generation Light-Driven Molecular Motors. Unidirectional Rotation Controlled by a Single Stereogenic Center with Near-Perfect Photoequilibria and Acceleration of

the Speed of Rotation by Structural Modification. *Journal of the American Chemical Society* **2002**, *124*, 5037–5051.

(5) Irie, M.; Fukaminato, T.; Matsuda, K.; Kobatake, S. Photochromism of Diarylethene Molecules and Crystals: Memories, Switches, and Actuators. *Chemical Reviews* **2014**, *114*, 12174–12277.

(6) Guinart, A.; Korpidou, M.; Doellerer, D.; Pacella, G.; Stuart, M. C. A.; Dinu, I. A.; Portale, G.; Palivan, C.; Feringa, B. L. Synthetic Molecular Motor Activates Drug Delivery from Polymersomes. *Proceedings of the National Academy of Sciences* **2023**, *120*, e2301279120.

(7) Hou, J.; Mondal, A.; Long, G.; de Haan, L.; Zhao, W.; Zhou, G.; Liu, D.; Broer, D. J.; Chen, J.; Feringa, B. L. Photo-Responsive Helical Motion by Light-Driven Molecular Motors in a Liquid-Crystal Network. *Angewandte Chemie International Edition* **2021**, *60*, 8251–8257.

(8) Rajonson, G.; Ciobotarescu, S.; Teboul, V. Optimizing the Motion of a Folding Molecular Motor in Soft Matter. *Physical Chemistry Chemical Physics* **2018**, *20*, 10077–10085.

(9) Wang, J.; Feringa, B. L. Dynamic Control of Chiral Space in a Catalytic Asymmetric Reaction Using a Molecular Motor. *Science* **2011**, *331*, 1429–1432.

(10) Orlova, T.; Lancia, F.; Loussert, C.; Iamsaard, S.; Katsonis, N.; Brasselet, E. Revolving Supramolecular Chiral Structures Powered by Light in Nanomotor-Doped Liquid Crystals. *Nature Nanotechnology* **2018**, *13*, 304–308.

(11) Pooler, D. R. S.; Lubbe, A. S.; Crespi, S.; Feringa, B. L. Designing Light-Driven Rotary Molecular Motors. *Chemical Science* **2021**, *12*, 14964–14986.

(12) Vicario, J.; Meetsma, A.; Feringa, B. L. Controlling the Speed of Rotation in Molec-

ular Motors. Dramatic Acceleration of the Rotary Motion by Structural Modification. *Chemical Communications* **2005**, 5910–5912.

(13) Huang, H.; Orlova, T.; Matt, B.; Katsonis, N. Long-Lived Supramolecular Helices Promoted by Fluorinated Photoswitches. *Macromolecular Rapid Communications* **2018**, *39*, 1700387.

(14) Bléger, D.; Schwarz, J.; Brouwer, A. M.; Hecht, S. O-Fluoroazobenzenes as Readily Synthesized Photoswitches Offering Nearly Quantitative Two-Way Isomerization with Visible Light. *Journal of the American Chemical Society* **2012**, *134*, 20597–20600.

(15) Štacko, P.; Kistemaker, J. C. M.; Feringa, B. L. Fluorine-Substituted Molecular Motors with a Quaternary Stereogenic Center. *Chemistry – A European Journal* **2017**, *23*, 6643–6653.

(16) Tambovtsev, I.; Schmerwitz, Y. L. A.; Levi, G.; Darmoroz, D. D.; Nesterov, P. V.; Orlova, T.; Jónsson, H. Fine Tuning of the Rotational Speed of Light-Driven, Second-Generation Molecular Motors by Fluorine Substitution. *The Journal of Physical Chemistry Letters* **2025**, 4014–4020.

(17) Vicario, J.; Walko, M.; Meetsma, A.; Feringa, B. L. Fine Tuning of the Rotary Motion by Structural Modification in Light-Driven Unidirectional Molecular Motors. *Journal of the American Chemical Society* **2006**, *128*, 5127–5135.

(18) Pollard, M. M.; Meetsma, A.; Feringa, B. L. A Redesign of Light-Driven Rotary Molecular Motors. *Organic & Biomolecular Chemistry* **2008**, *6*, 507–512.

(19) Pollard, M. M.; Wesenhagen, P. V.; Pijper, D.; Feringa, B. L. On the Effect of Donor and Acceptor Substituents on the Behaviour of Light-Driven Rotary Molecular Motors. *Organic & Biomolecular Chemistry* **2008**, *6*, 1605–1612.

(20) Cnossen, A.; Pijper, D.; Kudernac, T.; Pollard, M. M.; Katsonis, N.; Feringa, B. L. A Trimer of Ultrafast Nanomotors: Synthesis, Photochemistry and Self-Assembly on Graphite. *Chemistry (Weinheim an Der Bergstrasse, Germany)* **2009**, *15*, 2768–2772.

(21) García-López, V.; Liu, D.; Tour, J. M. Light-Activated Organic Molecular Motors and Their Applications. *Chemical Reviews* **2020**, *120*, 79–124.

(22) Mills, G.; Jónsson, H.; Schenter, G. K. Reversible Work Transition State Theory: Application to Dissociative Adsorption of Hydrogen. *Surface Science* **1995**, *324*, 305–337.

(23) Henkelman, G.; Uberuaga, B. P.; Jónsson, H. A Climbing Image Nudged Elastic Band Method for Finding Saddle Points and Minimum Energy Paths. *The Journal of Chemical Physics* **2000**, *113*, 9901–9904.

(24) Henkelman, G.; Jónsson, H. Improved Tangent Estimate in the Nudged Elastic Band Method for Finding Minimum Energy Paths and Saddle Points. *The Journal of Chemical Physics* **2000**, *113*, 9978–9985.

(25) Ásgeirsson, V.; Birgisson, B. O.; Bjornsson, R.; Becker, U.; Neese, F.; Riplinger, C.; Jónsson, H. Nudged Elastic Band Method for Molecular Reactions Using Energy-Weighted Springs Combined with Eigenvector Following. *Journal of Chemical Theory and Computation* **2021**, *17*, 4929–4945.

(26) Neese, F. Software Update: The ORCA Program System—Version 6.0. *WIREs Computational Molecular Science* **2025**, *15*, e70019.

(27) Schmerwitz, Y. L. A.; Ásgeirsson, V.; Jónsson, H. Improved Initialization of Optimal Path Calculations Using Sequential Traversal over the Image-Dependent Pair Potential Surface. *Journal of Chemical Theory and Computation* **2024**, *20*, 155–163.

(28) Lee, C.; Yang, W.; Parr, R. G. Development of the Colle-Salvetti Correlation-Energy

Formula into a Functional of the Electron Density. *Physical Review B* **1988**, *37*, 785–789.

(29) Becke, A. D. Density-Functional Exchange-Energy Approximation with Correct Asymptotic Behavior. *Physical Review A* **1988**, *38*, 3098–3100.

(30) Becke, A. D. Density-functional Thermochemistry. III. The Role of Exact Exchange. *The Journal of Chemical Physics* **1993**, *98*, 5648–5652.

(31) Hehre, W. J.; Ditchfield, R.; Pople, J. A. Self—Consistent Molecular Orbital Methods. XII. Further Extensions of Gaussian—Type Basis Sets for Use in Molecular Orbital Studies of Organic Molecules. *The Journal of Chemical Physics* **2003**, *56*, 2257–2261.

(32) Weigend, F. Accurate Coulomb-fitting Basis Sets for H to Rn. *Physical Chemistry Chemical Physics* **2006**, *8*, 1057–1065.

(33) Wigner, E. The Transition State Method. *Transactions of the Faraday Society* **1938**, *34*, 29–41.

(34) Vineyard, G. H. Frequency Factors and Isotope Effects in Solid State Rate Processes. *Journal of Physics and Chemistry of Solids* **1957**, *3*, 121–127.

TOC Graphic

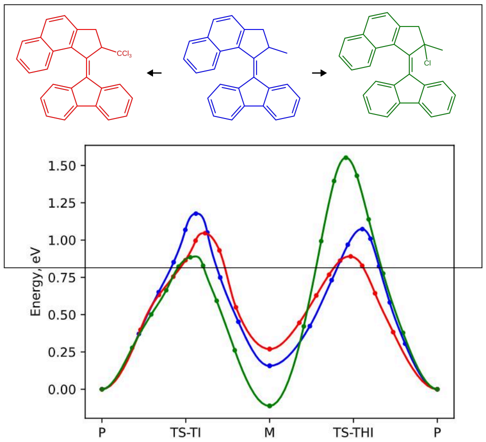

Paper IV

Pair interaction of localized topological structures in confined chiral media

Ivan M. Tambovtsev et al.

Phys. Rev. E 108, 024705 (2023)

Developed minimization procedure; performed numerical analysis; prepared figures and manuscript draft.

PHYSICAL REVIEW E **108**, 024705 (2023)

Pair interaction of localized topological structures in confined chiral media

I. M. Tambovtsev,[1,2,3] I. S. Lobanov,[1] Alexei D. Kiselev,[4] and V. M. Uzdin[1,2]
[1]*Faculty of Physics, ITMO University, 197101 St. Petersburg, Russia*
[2]*Department of Physics, St. Petersburg State University, St. Petersburg 198504, Russia*
[3]*Science Institute and Faculty of Physical Sciences, University of Iceland, 107 Reykjavík, Iceland*
[4]*Laboratory of Quantum Processes and Measurements, ITMO University, 199034 Saint Petersburg, Russia*

(Received 15 May 2023; accepted 8 August 2023; published 31 August 2023)

We study pairwise interactions between localized topological structures in chiral magnetic and cholesteric liquid crystal (CLC) systems confined in the planar geometry. Our calculations for magnetics are based on the lattice model that takes into account the bulk and surface anisotropies along with the exchange and the Dzyaloshinskii-Moriya interactions. In CLC cells, these anisotropies describe the energy of interaction with an external magnetic or electric field and the anchoring energy assuming that the magnetic or electric anisotropy is negative and the boundary conditions are homeotropic. We have selected the region of the phase diagram, where various localized solitonlike structures, including skyrmion tubes, torons, and leeches, embedded in the ground state of the z-cone (conical phase) coexist, and carried out numerical analysis of the distance dependencies of the effective intersoliton interaction potentials. For skyrmions and torons, the potentials are found to be attractive in the large separation region. It turned out that for these potentials, the effects of axial asymmetry are negligible. By contrast, it turned out that for the intermediate structures between the skyrmions and torons known as the leeches, the leech-leech potentials generally depend on the orientation of the intersoliton separation vector and their large distance parts may become repulsive at certain directions of the vector. All the potentials have the short distance repulsive parts and the local minima located at the equilibrium separations. It is found that the skyrmion-skyrmion potential has an additional metastable configuration shifted towards the short-distance region.

DOI: 10.1103/PhysRevE.108.024705

I. INTRODUCTION

Magnets, liquid crystals (LCs), and colloids are known as host materials for numerous topological solitons such as skyrmions, antiskyrmions, torons, bobbers, hopfions, heliknotons, and twistions [1–9]. In the zoo of solitons, the skyrmions represent one of the most studied structures that are promising for a new generation of racetrack memories and a wealth of spintronic and photonic applications [10–14]. Under certain conditions, especially in three-dimensional systems, different localized topological structures can coexist [15].

There are chiral materials such as chiral magnets and chiral nematic liquid crystals, also known as cholesteric liquid crystals (CLCs), that have attracted particular interest as systems providing valuable insights into the above diversity of localized structures [8,15–18]. The chirality of magnetic materials is typically due to the Dzyaloshinskii-Moriya interaction (DMI) caused by the spin-orbit coupling, whereas chiral ordering observed in CLCs is an immediate consequence of the broken mirror symmetry caused by the presence of anisotropic molecules with no mirror plane. An important point is that the bulk chirality of CLC materials, which is typically determined by the concentration of chiral additives, can be controlled by external stimuli such as temperature, electromagnetic fields, and the anchoring conditions at boundary surfaces [19–23]. The latter is closely related to the size and type of the confined geometry, which is another important factor that may greatly influence localized structures in both chiral magnetic and CLC systems.

In thin chiral magnetic films, the quasi-two-dimensional skyrmions can appear either as individual objects or as skyrmion lattices [24]. In magnetic systems that are a few atomic monolayers thick, these topological solitons are uniform along the normal to the film [3]. By contrast, in bulk chiral media, one can observe extended skyrmion tubes with discrete translational symmetry along the tube. Thus, these structures are not completely homogeneous along these lines [25].

In the bulk of chiral ferromagnets, at external magnetic fields in a certain range, the ground state is the cone phase with the cone axis along the magnetic field [26]. Such systems may also contain metastable asymmetric skyrmions. In the slab geometry, the cone ground state and metastable skyrmions can be realized in LC cells with homeotropic anchoring of the director at the substrates [15,27]. When the cell thickness compares with the equilibrium pitch of the bulk helical ground-state structure, additional localized structures such as torons and leeches can be implemented [15].

Although localized topological structures in chiral media behave like separate quasiparticles, they interact and this interaction determines the geometry of many-solitonic structures, as well as their collective dynamics and properties.

In the two-dimensional case, magnetic skyrmions tend to repel each other, but this interaction decreases exponentially with the interskyrmion distance [18,28–30]. The repulsion is determined by the change in DMI, which makes a negative contribution to the self-energy of a single skyrmion. However, in metal films with frustrated exchange interaction, at certain distances between skyrmions, effective attractive interactions may occur, leading to the formation of skyrmion clusters [31].

In three-dimensional systems, skyrmion tubes can be attracted to each other and form quite complex topological structures. In Refs. [32,33], it was found that skyrmion tubes perturb the surrounding chiral environment, leading to the formation of complex superstructures that contain both parallel and orthogonal tubes. The tubes can be deformed when they are separated by the distance of the order of their diameter.

Direct observation of attractive skyrmions and skyrmion clusters in the conical phase of the cubic Cu_2OSeO_3 helimagnet was reported by Loudon *et al.* in Ref. [34]. In B20-type FeGe strips, the skyrmion attraction was also observed at moderate magnetic fields. The attraction is found to change into repulsion as the field increases [35].

In bulk chiral materials, the structure of the skyrmion clusters can be rather complex and can be controlled using an external magnetic field. Skyrmion tubes can be located either perpendicular or parallel to the external magnetic field, and such configurations coexist in a specific range of fields [25,32] A similar complex configuration of skyrmion tubes has been predicted and observed in chiral LC systems [33]. The crossover between different regimes of skyrmion interaction has been revealed by changing the layer thickness and/or the surface anchoring.

Interestingly, topological particlelike localized LC structures bear some resemblance to colloidal particles dispersed in a LC host (see reviews [6,36,37] for details on liquid crystal colloids). Colloidal interactions are mediated by elastic distortions induced by the interacting particles [38–46]. When the characteristic length of the distortions is larger than the particles' size, the elastic interaction can be approximately described using an analogy with the interaction between electrostatic multipoles [47]. Otherwise, the confined geometry and the anchoring conditions may have a profound effect on the colloidal interactions [44–46].

Similar to interparticle interaction in LC colloids, the interskyrmion interaction in CLCs is determined by the elastic interactions [48]. These interactions can also be tuned by an external electric field [49].

In magnetic films, the properties of localized magnetic structures such as skyrmion tubes depend on the film thickness [50]. In thin films, new localized topological structures can be stabilized near the surfaces and interfaces of magnetic and LC-chiral media [15]. These include chiral bobbers experimentally observed in thin plates of B20-type FeGe [16], stacked spin spirals in magnetic films [51], torons, twisted walls, fingers, and their hybrids in chiral nematics [52].

Interaction between such structures is much less studied as compared to the interskyrmion interaction in the bulk. In this paper, the intersolitonic interaction between topological structures formed in the films filled with chiral magnetic and LC media will be our primary concern.

The paper is organized as follows. In Sec. II, we describe the model and the soliton structures simultaneously stabilized in the coexistence region of the phase diagram. The numerical procedure employed for computing the intersoliton interaction potentials is outlined in Sec. III, where we also present the results of our calculations. Three-soliton structures are briefly discussed in Sec. IV. Finally, in Sec. V, we draw our results together and make some concluding remarks.

II. MODEL AND LOCALIZED STRUCTURES

Following our previous study [15], we consider a chiral magnetic and nematic liquid crystal material confined in the slab geometry and begin with the continuum model of the film giving the free energy functional of the following form:

$$F[\mathbf{m}] = \int_V dV \{\mathcal{A}(\nabla\mathbf{m})^2 - \mathcal{D}\mathbf{m}\cdot[\nabla\times\mathbf{m}] - \mathcal{K}_b(\mathbf{m}\cdot\mathbf{z})^2\} - \mathcal{K}_s\int_S ds(\mathbf{m}\cdot\mathbf{z})^2, \quad (1)$$

where V is the volume of the film and S is the bounding surface represented by two substrates normal to the z axis; $\mathbf{m}(\mathbf{r})$ is the vector field representing either the unit magnetization vector or the CLC director; and $\mathbf{z}$ is the unit vector along the anisotropy axis assumed to be normal to the bounding surfaces S.

For magnetic systems, the first term describes the exchange interaction determined by the exchange stiffness $\mathcal{A}$, which is assumed to be homogeneous in the bulk of the film. The second term corresponds to chiral Dzyaloshinskii-Moriya interaction (DMI) with the interaction constant $\mathcal{D}$. The third contribution is the density of magnetic anisotropy described by the parameter $\mathcal{K}$, whose values inside the film, $\mathcal{K} = \mathcal{K}_b$, and at its boundaries may differ, $\mathcal{K}_s \neq \mathcal{K}_b$.

For LC systems, the value of $\mathcal{A}$ and the chiral interaction constant $\mathcal{D}$ are expressed in terms of the Oseen-Frank moduli in the one-constant approximation where all the elastic constants are assumed to be equal, $K_1 = K_2 = K_3 = K$: $\mathcal{A} = K/2$ and $\mathcal{D} = Kq_0$, where q_0 is the free twisting wave number. In this case, the bulk value of the anisotropy constant, $\mathcal{K}_b$, plays the role of the coupling constant for interaction with the external magnetic field, whereas its value at the substrates corresponds to the anchoring energy strength (the anchoring conditions are assumed to be homeotropic).

As in Ref. [15], our overall computational strategy involves two basic steps: (a) we introduce a properly discretized version of the free energy (1) as the lattice model of the Heisenberg-like form on the rectangular three-dimensional (3D) grid of the size $N_x \times N_y \times N_z$, and (b) we employ the direct energy minimization by the nonlinear conjugate gradient method in Cartesian coordinates with constraints that fix the unit length of the magnetization or director at the sites of the lattice.

For the lattice model with magnetic moments or CLC directors localized at the sites of a simple cubic lattice, the energy of the system reads [15]

$$E[\mathbf{S}] = -\sum_{\langle i,j\rangle}(J\mathbf{S}_i\cdot\mathbf{S}_j + \mathbf{D}_{i,j}\cdot[\mathbf{S}_i\times\mathbf{S}_j]) - \sum_i K_i\big(S_i^z\big)^2, \quad (2)$$

where summation $\langle i, j\rangle$ is performed over the nearest neighbors, $J = 2a\mathcal{A}$ is the exchange parameter, $\mathbf{D}_{ij}$ is the DMI vector of the length $|\mathbf{D}_{ij}| \equiv D = a^2\mathcal{D}$, and $K_{b,s} = a^2\mathcal{K}_{b,s}$ is the anisotropy parameter; a is the lattice constant and $\mathbf{S}_i \equiv \mathbf{m}_i$ is the unit vector along the magnetic moment or CLC director

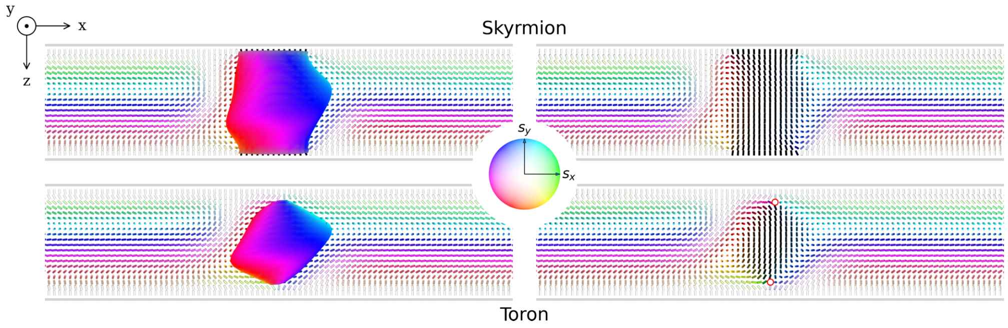

FIG. 1. Orientational structures in the xz plane for a skyrmion (top) and a toron (bottom) embedded into the film filled with chiral magnetic or LC material. The film thickness is p_0 and horizontal gray lines indicate planar confining surfaces with homeotropic anchoring conditions. The magnetization or LC director field, **S**, is shown using rods colored according to the color palette in the inset at the center that describes the x and y projections of **S**. This color wheel represents the northern hemisphere of magnetization or director orientations where S_z is non-negative and the white color represents the direction along the z axis with $S_z = 1$. In the southern hemisphere, the colors become darker as S_z decreases, approaching the southern pole with $S_z = -1$ indicated by black color. The surfaces on the left are isosurfaces of the z projection of **S** computed at $S_z = 0$ for the skyrmion (top) and the toron (bottom) structures, whose orientational fields are depicted on the right side of the figure. Circles indicate two point defects (hedgehogs) in the toron structure.

at the site i. For the sake of brevity, the vectors $\mathbf{S}_i$ representing the unit magnetization vector or CLC director are sometimes loosely called the spins.

Similar to the continuum model (1), the first term on the right-hand side of Eq. (2) describes the exchange interaction, whereas the second term is DMI. Both the exchange parameter J and the length of the DMI vector, $\mathbf{D}_{ij}$, $|\mathbf{D}_{ij}| = D$, are assumed to be constant. The direction of the DMI vector $\mathbf{D}_{ij}$ is along the vector connecting the nodes i and j, thus stabilizing the Bloch-type skyrmion structures.

The last term in the energy (2) represents the magnetic anisotropy with the anisotropy axis normal to the substrates (the z axis). For the easy-plane anisotropy, the bulk value of K_i is negative, $K_i = K_b \leqslant 0$, and is fixed for all layers of the film. In magnetic systems, such anisotropy can be induced, for example, by magnetostatic interactions due to the flat shape of the sample [53]. We assume that owing to the additional surface anisotropy $K_s > 0$, the anisotropy parameter at the interfacial layers, $K_i = K_b + K_s$, is positive.

For LC systems, the spin $\mathbf{S}_i$ gives vectorization of the CLC director field at the ith site and the exchange constant J is proportional to the Frank elastic constant: $J = aK$. The easy-plane anisotropy in the bulk corresponds to the energy of interaction between a LC with negative magnetic susceptibility, $\Delta\chi < 0$, and a magnetic field applied across the cell, whereas the surface anisotropy with the positive anisotropy parameter describes the surface energy for the CLC with the homeotropic anchoring conditions at bounding surfaces. The CLC chirality is characterized by the equilibrium twist wave number $q_0 = 2\pi/p_0 = \arctan(D/J)$, where p_0 is the pitch of the helical structure representing the ground state in an unbounded sample.

It is convenient to introduce dimensionless parameters: $\kappa^b = K_b J/D^2$ and $\kappa^s = K_s J/D^2$. For states homogeneous along the y axis, the phase diagram in the κ^b-κ^s plane was calculated in Ref. [15]. According to this diagram, the ground state can be represented by various types of delocalized structures, such as the z-helix, the z-cone, the x-helicoid, and the oblique helicoid depending on the dimensionless parameters of bulk and surface anisotropy, κ^b and κ^s.

It was shown that for sufficiently large values of the surface anisotropy κ^s, the ground state of the chiral film is the conical phase which is invariant with respect to in-plane translations and is described by the z-cone structure. Several localized topological structures can be embedded into the z-cone far-field background in the form of metastable excitations [15]. Figures 1 and 2 present some of these states, which can be regarded as topological solitons.

Orientational structures for the skyrmion tube and the toron in the cell geometry are depicted in Fig. 1. The skyrmion tube shown in Fig. 1 (top) resembles skyrmion tubes in bulk chiral magnets in a vertically aligned magnetic field [25,32]. In moderate magnetic field, the magnetically induced conical phase is found to impose a twisting effect on the tube, leading to the crankshaft structure.

Figure 1 (bottom) presents the solitonic structure that, following notations of Refs. [8,52], can be identified as the toron. This structure is essentially a skyrmion tube terminated on two point defects (hedgehogs of opposite charge) near the substrates, whereas the remaining part of the toron is localized in the bulk of the film. Although the toron in Fig. 1 (bottom) bears a general resemblance to those described in [8,52], in our case, it is surrounded by the conical phase that, similar to the skyrmion tube, induces twists of the toron.

The solitonic structure shown in Fig. 2 can be viewed as the intermediate case between the skyrmion tube and the toron and will be called the leech [15]. In asymmetric LC cells, the leechlike structures were previously described as skyrmion or toron hybrids [5,52]. By contrast to the hybrids, the leech structures under consideration are embedded into the twisted conical background of symmetric cells.

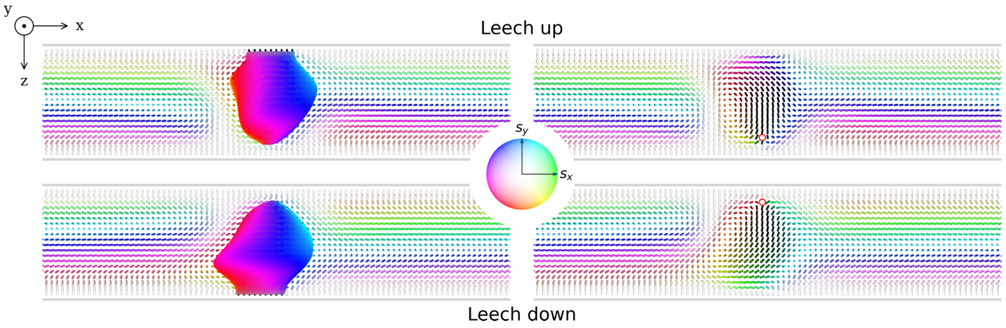

FIG. 2. Orientational structures in the xz plane for the leech up (top) and the leech down (bottom) representing the leeches that terminate on the point defects located near the upper and lower bounding surfaces, respectively (parameters and colors are described in the caption of Fig. 1).

From Fig. 2, these structures are attached to one of the substrates and terminate on a singular point near the other substrate. When the terminating point defect is located close to the upper (lower) bounding surface, the leech will be referred to as the leech up (leech down).

The regions of stability for these states are generally different. As the bulk anisotropy (external field) increases, the skyrmion tube decays into a pair of bobbers, whereas the leech and the toron will transform into a single bobber and the z-cone, respectively.

An important point is that there is the range of anisotropy parameters where all the above structures can coexist simultaneously. In this coexistence range of the phase diagram (see Fig. 14 in Ref. [15]), we shall study the intersoliton interaction between different topological structures.

In Figs. 1 and 2 and in our subsequent calculations, the values of the surface and bulk anisotropies are taken to be $\kappa^s = 24$ and $\kappa^b = -0.25$, respectively. These values correspond to the point in the coexistence domain of the phase diagram. We shall also assume that the film thickness equals the equilibrium pitch $p_0 = N_z a$, where a is the lattice constant and $N_z = 20$, and thus the DMI parameter (the length of the DMI vector) is $D = J\tan(\pi/10)$. The in-plane (lateral) size of the film with the boundary surfaces (substrates) parallel to the x-y plane is $N_x \times N_y = 400 \times 400$ and the in-plane boundary conditions are periodic.

III. PAIRWISE INTERSOLITON INTERACTIONS

In this section, we study the interactions between the localized topological (soliton) structures depicted in Figs. 1 and 2. Orientational distributions for these structures computed using the parameters listed at the end of the preceding section can now be used to produce the initial seed states for two-soliton configurations spaced at a given intersoliton distance. More specifically, the initial configurations are obtained by placing two cutouts from single-soliton textures in the nonoverlapping cylinder-shaped domains of the radius equal to $7.5a$ into the background structure without topological solitons.

Each seed state is subjected to the three-step minimization procedure. During the first step, orientation of two magnetic moments or CLC directors (spins) located at the centers of interacting solitons are kept intact and the initial structure is optimized to achieve a local energy minimum under the above constraint that fixes the intersoliton separation. At the second step, in order to reduce the error in estimated energy arising due to the presence of frozen (pinned) spins, a minimization procedure is applied so as to correct the orientation of the magnetic moments or CLC directors (spins) in close vicinity of the pinned spins, including themselves (the radius of the neighborhood is $5a$). This step ensures that the spins outside the neighborhood remain unchanged. Finally, the minimization procedure used at the first step is repeated. This procedure can be continued iteratively, but calculations show that the difference between the energies evaluated at the last two steps is negligibly small. So, changes in energy are mainly produced by minimization performed at the second step. Note that our approach can be employed to improve the accuracy of the calculations of the skyrmion-skyrmion and skyrmion-defect interactions performed in Refs. [29,54,55], where the distances are fixed using the fixed center-spin method corresponding to the first step of our procedure.

Note that at sufficiently large distances, additional unconstrained minimization of the optimized structure will not produce noticeable changes in the loci of the solitons. This is the lattice (discretization) effect that manifests itself in the presence of numerous nearly degenerate metastable configurations on the energy surface.

The above numerical procedure is applied to compute the energy of the two-soliton structures as a function of the distance between the solitons. The difference between this energy and the sum of single-soliton energies gives the interaction energy. In order to reduce numerical error caused by subtraction of large energies resulting from a huge number of spins, the energies were counted from the cone ground state.

Note that the intersoliton separation is determined by the vector connecting the centers of the solitons evaluated using the procedure that bears close similarity to evaluating the center of mass. In this procedure, the weight of the ith point is

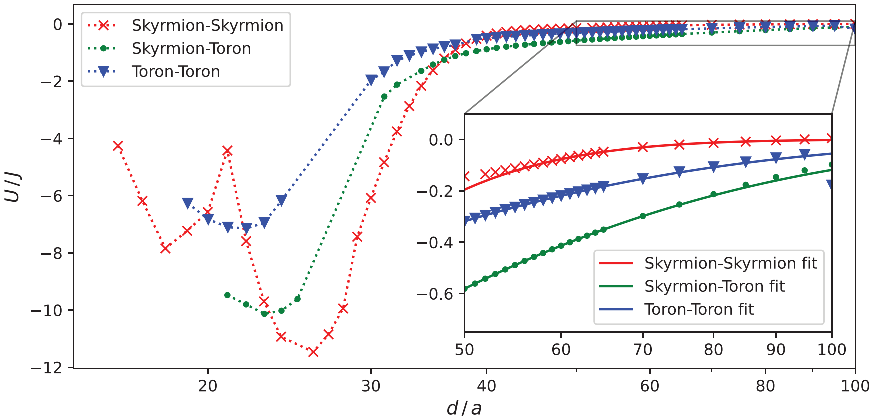

FIG. 3. Dependence of effective potentials of pairwise interactions between skyrmions and torons on dimensionless intersoliton separation, d/a. The inset enlarges the long-separation tails of the potentials fitted assuming that their large-distance asymptotic behavior is described by formula (3). Solid lines are the fitting curves computed at the values of the decay rate fitting parameter: $c_2 = 0.0282$ (the toron-toron interaction), $c_2 = 0.0847$ (the skyrmion-skyrmion interaction), and $c_2 = 0.0249$ (the toron-skyrmion interaction).

the length of difference between the local spin (magnetization, LC director) $\mathbf{S}_i$ and the corresponding vector $\mathbf{S}_i^{(\mathrm{cone})}$ specifying the orientation of the unperturbed background structure: $|\mathbf{S}_i - \mathbf{S}_i^{(\mathrm{cone})}|$.

Figure 3 shows the results for the dependence of the interaction energy on the separation d computed for different pairs: a pair of skyrmion tubes (S-S), a pair of torons (T-T), and a toron-skyrmion tube pair (T-S). It can be seen that at large separations, skyrmions and torons are attracted to each other.

According to theoretical studies on the pair interaction between 2D skyrmions [18,28–30], the asymptotic behavior of interskyrmion potentials is described by the relation

$$U(d) \approx \frac{c_1}{\sqrt{d}} \exp(-c_2 d). \tag{3}$$

Note that for 3D skyrmions, this result also follows from the theoretical considerations of Ref. [48], where the skyrmions were viewed as colloidal particles and the interskyrmion interaction was treated as an elastic interaction between colloidal particles. According to Ref. [43], formula (3) also governs the long-distance regime of the interparticle potential for colloidal particles in a nematic cell with rigid homeotropic anchoring conditions.

We have used Eq. (3) to fit large-distance tails of the potentials using coefficients c_1 and c_2 as the fitting parameters. The results presented in the inset of Fig. 3 show that in the large-separation range, the asymptotics given by formula (3) provide a good approximation for intersolitonic interactions involving skyrmions and torons. Specifically, the toron-toron interaction potential with $c_2 = 0.0282$ is found to decay slower than both the interskyrmion ($c_2 = 0.0847$) and the skyrmion-toron ($c_2 = 0.0249$) potentials. The coefficients in the asymptotics are computed for the parameters specified above.

Referring to Fig. 3, at small distances of the order of the size of topological solitons, the particlelike structures repel each other and, for each interaction potential, there is a minimum intersoliton distance $d_{\min}$ giving the equilibrium separation of the most energetically favorable two-solitonic configuration. Clearly, our considerations are not applicable to the region of intersoliton separations that are smaller than the soliton size, where orientational structures are significantly disturbed, forming new complex states.

As can be seen from Fig. 3, the minimum distances are ordered as follows: $d_{\min}^{(T-T)} < d_{\min}^{(T-S)} < d_{\min}^{(S-S)}$. Thus, the largest minimum distance corresponds to the two-skyrmion structure, whereas the pair of torons possess the shortest equilibrium separation. The potential well for the bounded pair is deeper for solitons with larger separations, so the two-skyrmion pair is the most stable configuration, whereas the pair of torons is the least stable one. Interestingly, the two-skyrmion potential exhibits two local minima at the distances $d = 18a$ and $d = 26a$, where the latter represents the equilibrium structure with the lowest energy (Fig. 3).

In the vicinity of the minimum, the distance dependence of the interaction energy is parabolic and can be described in terms of the stiffness of the effective interaction k. From Fig. 3, it is clear that as opposed to the case of the minimum distances, the largest stiffness k_{T-T} corresponds to the pair of torons, whereas a couple of skyrmion tubes has the smallest stiffness, k_{S-S}. So, we have $k_{T-T} > k_{T-S} > k_{S-S}$.

The existence of the minima for the pair interaction potentials would result in the formation of spatially ordered structures such as two-dimensional clusters, similar to the schools of skyrmions observed in CLC films [49]. The above three equilibrium two-soliton structures are shown in Fig. 4. The values of the effective potential at local minima corresponding to these structures give two-soliton binding (bonding) energies. For skyrmions and torons, these energies are listed in the first column of Table I.

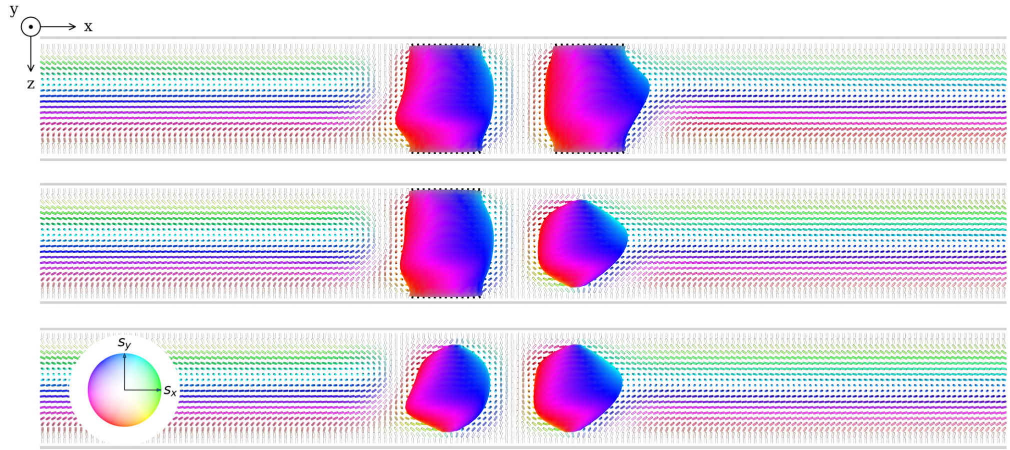

FIG. 4. Equilibrium two-soliton configurations for a pair of interacting skyrmion tubes (top), skyrmion-toron structure (middle), and toron-toron structure (bottom) in the chiral magnetic film or CLC cell (parameters and elements of visualization are explained in the caption of Fig. 1).

Although topological solitons are, in general, cylindrically (axially) asymmetric, the interaction potentials are found to be nearly insensitive to rotations of the intersoliton vector about the normal to the bounding surfaces (substrates). It agrees with the theoretical results of Refs. [18,48] and an important consequence of this is that both the skyrmion and toron lattices will be triangular.

Now we pass on to the interaction of the so-called leech states. As is shown in Fig. 2 (see, also, discussion in Sec. II), this structure is attached to one of the bounding surfaces of the film and looks like an intermediate state between the skyrmion tube and the toron. Since the film thickness only slightly exceeds the length of the leeches, the interaction between leeches located at different surfaces is strong enough to form two-leech structures. Therefore, for leeches, the diversity of interacting structures that depend on leech alignment is wider as compared to the skyrmion tubes and the torons.

We begin with the case of identically aligned leeches where the states are localized at the same film surface. The dependence of the interaction energy on the separation for a pair of leeches up is presented at the top of Fig. 5. It turns out that in contrast to the interaction of torons and skyrmions shown in Fig. 3, for leeches, the interaction is anisotropic and the interaction energy depends on the orientation of the intersolitonic separation vector. In Fig. 5, this orientation is specified by the angle α between the lateral component of the separation vector and the vector that defines the spin or director far-field orientation of the background spiral structure in the middle of the film. Insets in Fig. 5 illustrate orientations of the interleech vector at $\alpha \in \{0, \pm\pi/4, \pm3\pi/4, \pi\}$. It can be seen that whatever the orientation of the interleech vector is, there is a local minimum of the interaction energy representing a locally stable structure. The corresponding spatial two-leech configuration is illustrated in Fig. 6 (top). The depth of the minimum typically depends on the orientation of the intersoliton vector and is less pronounced than that for both the skyrmion tubes and the torons.

TABLE I. Binding energies of two-soliton and triple-soliton structures. Percents in brackets indicate the relative difference between the triple-soliton binding energy and the sum of pair interaction (two-soliton) energies associated with three (two) links of triangular (linear) configuration.

	Two-soliton structure	Triangular structure	Linear chain
Skyrmion	−11.46	−32.33 (6%)	−22.46 (2%)
Toron	−7.14	−17.34 (19%)	−14.28 (<1%)

Referring to Fig. 5 (top), variations of the results for the two-leech-up structures with $\Delta\alpha = \pi$ are within the accuracy of the computations, whereas the cases of the interleech vector orientations with $\alpha \in \{0, \pm\pi/4\}$ reveal noticeable differences. At $\alpha = -\pi/4$ (the separation vector is along the y axis), the local minimum is deeper than in other directions. Therefore, it might be expected that a square lattice will be formed as the stable state at certain temperatures.

In this case, in addition to the local energy minimum, the interaction potential reaches the maximum located at about $40a$. This maximum appears to be suppressed at $\alpha = 0$, whereas it is shifted to the region of longer distances and located at about $150a$ when $\alpha = \pi/4$ (the separation vector is along the x axis). Note that in the presence of the maximum, the long-distance tail corresponds to the repulsive part of the potential.

When the intersoliton vector is along the y axis and the distance exceeds the leech transverse size, the interaction is stronger than both the interskyrmion and the intertoron interactions. In addition, a comparison between Figs. 4 and 6 shows that in the region where, for skyrmions and torons, the far-field spiral structure is undisturbed (see Fig. 4), the interleech interaction produces noticeable distortions of the

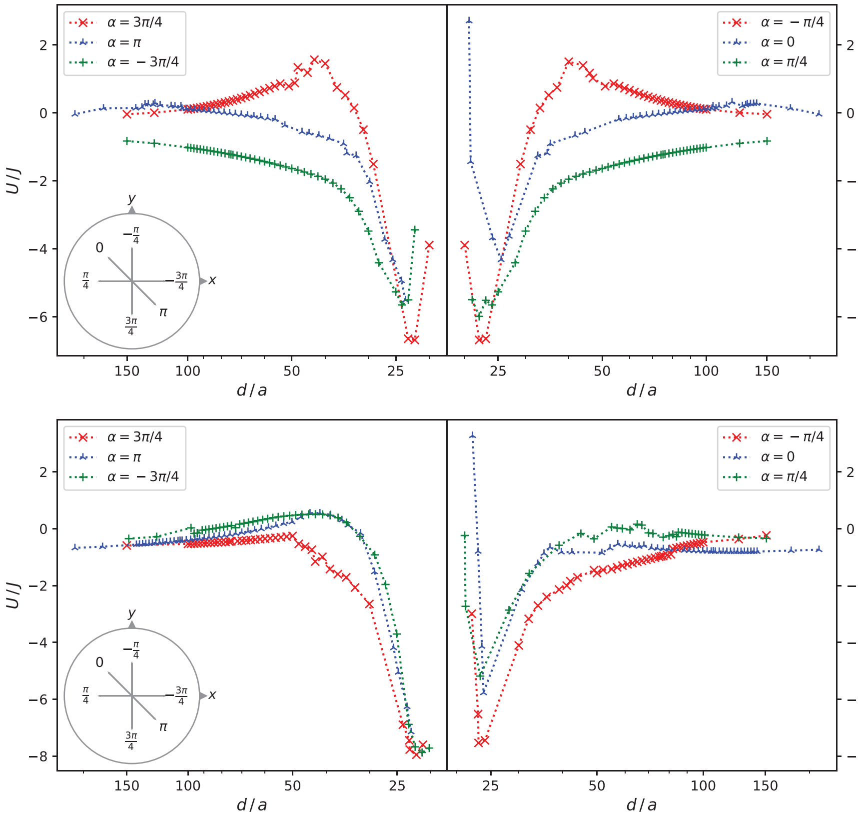

FIG. 5. Effective potential for pairwise interaction for identically aligned leeches (a pair of leeches up) (top) and for a leech up interacting with a leech down (bottom) at different values of the angle α between the intersoliton separation vector connecting the centers of the leeches and the spin or director of the background structure in the middle of the sample. Insets illustrate how the interleech vector is aligned depending on the value of α.

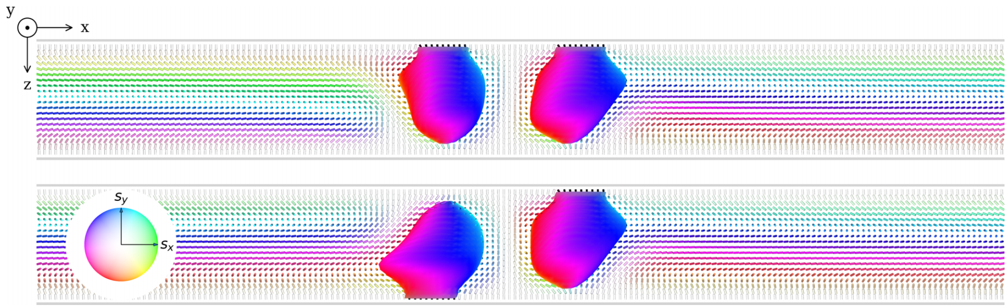

FIG. 6. Equilibrium states for two leeches up (top) and differently aligned leeches (bottom).

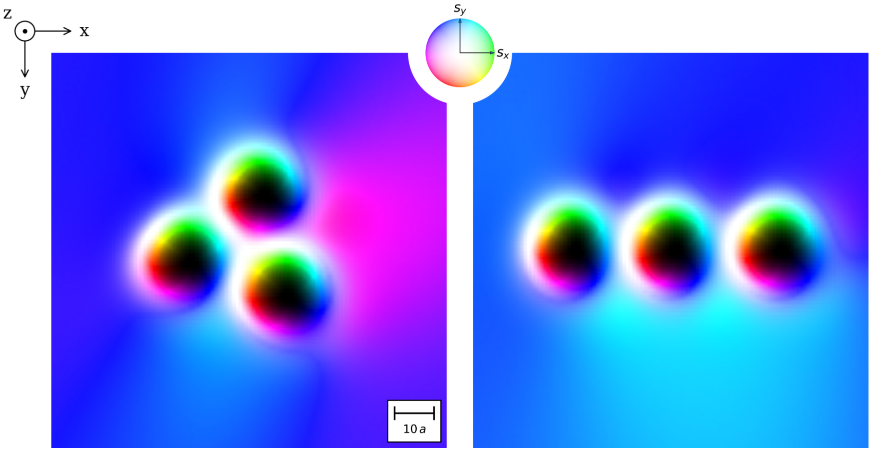

FIG. 7. Two three-skyrmion equilibrium configurations: the triangular structure (left) and the linear chain (right) in the chiral magnetic film or CLC cell (parameters and elements of visualization are explained in the caption of Fig. 1).

conical phase. Thus, we get the conclusion that the effective range of the interleech interaction is longer than the corresponding range of intersoliton interactions between skyrmions and torons.

For differently aligned leeches, the interleech interaction potentials of the the two-leech up-down structure computed at $\alpha \in \{0, \pm\pi/4, \pm3\pi/4, \pi\}$ are depicted in Fig. 5 (bottom). The two-leech configuration at the distance corresponding to the interaction energy minimum is shown in Fig. 6 (bottom).

At $\alpha = 0$ and $\alpha = \pi/4$, the separation dependence of the interaction energy exhibits a bit less pronounced maximum as compared to the case of identically aligned leeches with $\alpha = -\pi/4$. When the lateral component of the interleech vector is along the y axis ($\alpha = -\pi/4$), the maximum is suppressed and the long-distance part of the interaction is attractive.

It turns out that when the leeches are attached to different substrates, the interaction energy is no longer symmetric with respect to rotations about the z axis by π when the lateral component of the intersoliton vector changes its sign. In particular, from Fig. 5 (bottom), the difference between the energy maxima located on different sides of the reference structure is clearly seen.

IV. THREE-PARTICLE INTERACTION

As we have discussed in the previous section, the interaction between localized structures such as skyrmions and torons is attractive at sufficiently large separations. Therefore, it can be expected that these solitons will form ordered stable clusters determined by the pair interaction.

We have found that there are stable triple-soliton structures forming regularly shaped clusters of three solitons located at distances close to pairwise equilibrium. For skyrmions, Fig. 7 illustrates triangular and linearly ordered structures. The binding energies of skyrmion and toron structures, computed as the difference between the energy of the three-soliton configuration and the sum of single-soliton energies, are listed in Table I. It is seen that the skyrmion clusters are energetically favorable over the toron ones.

From Table I, a comparison between the sum of pair interaction energies and the three-soliton binding energy shows that pairwise interactions are the determining factors for linear chains of skyrmions and torons. For the solitons arranged in a regular triangle, the accuracy of the pairwise approximation is not good and breaks down in the case of torons, indicating the presence of the noticeable contribution coming from the three-body interaction.

V. CONCLUSIONS

In this paper, we have used the lattice model describing chiral magnetics and CLC systems confined in the slab geometry to study intersoliton interactions between a variety of topological structures coexisting at certain values of the surface and bulk anisotropies (the homeotropic anchoring energy strength and external magnetic field in the case of CLC cells). These structures include the skyrmion tubes, torons, and leeches (see Figs. 1 and 2).

The three-step minimization procedure detailed in Sec. III is employed to perform numerical analysis of the intersoliton interaction potentials that are plotted in relation to the separation (the intersoliton distance) in Figs. 3 and 5. For skyrmions and torons, all the potentials are found to be nearly cylindrically (axially) symmetric whose asymptotic behavior is determined by the attractive long-distance tails that can be fitted using the relation (3) previously derived for the skyrmion-skyrmion interaction potentials in Refs. [18,28–30,48]. Note that in reality, cylindrical symmetry is broken by the Dzyaloshinskii-Moriya interaction and the energy functional (2) is not invariant with respect to global rotations of the spins about the normal to the bounding surfaces.

Nevertheless, by contrast to the interleech potentials, the intersoliton potentials for skyrmions and torons appear to be symmetric, with the accuracy limited by the errors of discretization.

A feature shared by all the intersoliton interaction potentials is that there is a local minimum located at the equilibrium distance corresponding to the lowest-energy (equilibrium) two-soliton configuration (these structures are illustrated in Figs. 4 and 6). It is also found that in the case of the skyrmion-skyrmion interaction, there is an additional minimum representing a metastable state of the short-separated pair of skyrmion tubes.

For identically and differently aligned leeches, the results presented in Fig. 5 suggest sensitivity of the potential to orientation of the interleech separation vector. It is shown that at certain orientations of the vector, in contrast to the case of skyrmions and torons, the large-distance part of the potential may become repulsive owing to the presence a local maximum.

When several localized topological solitons can exist simultaneously, they may form ordered structures depending on the pairwise interaction between them. According to Fig. 7, the three-skyrmion locally stable structures are arranged either in a regular triangle or in a linear chain. Similar results hold for the three-toron structures. From Table I, the binding energies of linearly ordered structures are determined by the contributions coming from the two-soliton interaction, whereas, for the triangular structure of torons, the contribution of the three-soliton interaction cannot be neglected.

ACKNOWLEDGMENT

The study was supported by the Russian Science Foundation Grant No. 22-22-00632.

[1] N. Nagaosa and Y. Tokura, Topological properties and dynamics of magnetic skyrmions, Nat. Nanotechnol. **8**, 899 (2013).

[2] U. K. Rössler, A. N. Bogdanov, and C. Pfleiderer, Spontaneous skyrmion ground states in magnetic metals, Nature (London) **442**, 797 (2006).

[3] R. Wiesendanger, Nanoscale magnetic skyrmions in metallic films and multilayers: A new twist for spintronics, Nat. Rev. Mater. **1**, 16044 (2016).

[4] P. J. Ackerman and I. I. Smalyukh, Diversity of Knot Solitons in Liquid Crystals Manifested by Linking of Preimages in Torons and Hopfions, Phys. Rev. X **7**, 011006 (2017).

[5] I. I. Smalyukh, Review: Knots and other new topological effects in liquid crystals and colloids, Rep. Prog. Phys. **83**, 106601 (2020).

[6] I. Muševič, Interactions, topology and photonic properties of liquid crystal colloids and dispersions, Eur. Phys. J.: Spec. Top. **227**, 2455 (2019).

[7] B. Göbel, I. Mertig, and O. A. Tretiakov, Beyond skyrmions: Review and perspectives of alternative magnetic quasiparticles, Phys. Rep. **895**, 1 (2021).

[8] J.-S. Wu and I. I. Smalyukh, Hopfions, heliknotons, skyrmions, torons and both Abelian and non-Abelian vortices in chiral liquid crystals, Liq. Cryst. Rev. (2022), doi:10.1080/21680396.2022.2040058.

[9] V. M. Kuchkin, N. S. Kiselev, F. N. Rybakov, I. S. Lobanov, S. Blügel, and V. M. Uzdin, Heliknoton in a film of cubic chiral magnet, Front. Phys. **11**, 1201018 (2023).

[10] A. Fert, N. Reyren, and V. Cros, Magnetic skyrmions: Advances in physics and potential applications, Nat. Rev. Mater. **2**, 17031 (2017).

[11] *Magnetic Skyrmions and Their Applications*, Woodhead Publishing Series in Electronic and Optical Materials, edited by G. Finocchio and C. Panagopoulos (Elsevier, Duxford, UK, 2021), p. 451.

[12] J. H. Han, *Skyrmions in Condensed Matter*, Springer Tracts in Modern Physics Vol. 278 (Springer, New York, 2017), p. 177.

[13] *Skyrmions: Topological Structures, Properties, and Applications*, Series in Materials Science and Engineering, edited by J. P. Liu, Z. Zhang, and G. Zhao (CRC Press, Boca Raton, FL, 2017), p. 481.

[14] K. Everschor-Sitte, J. Masell, R. M. Reeve, and M. Kläui, Perspective: Magnetic skyrmions—Overview of recent progress in an active research field, J. Appl. Phys. **124**, 240901 (2018).

[15] I. M. Tambovtsev, A. O. Leonov, I. S. Lobanov, A. D. Kiselev, and V. M. Uzdin, Topological structures in chiral media: Effects of confined geometry, Phys. Rev. E **105**, 034701 (2022).

[16] F. Zheng, F. N. Rybakov, A. B. Borisov, D. Song, S. Wang, Z. A. Li, H. Du, N. S. Kiselev, J. Caron, A. Kovács, M. Tian, Y. Zhang, S. Blügel, and R. E. Dunin-Borkowski, Experimental observation of chiral magnetic bobbers in B20-type FeGe, Nat. Nanotechnol. **13**, 451 (2018).

[17] S. Schneider, D. Wolf, M. J. Stolt, S. Jin, D. Pohl, B. Rellinghaus, M. Schmidt, B. Büchner, S. T. B. Goennenwein, K. Nielsch, and A. Lubk, Induction Mapping of the 3D-Modulated Spin Texture of Skyrmions in Thin Helimagnets, Phys. Rev. Lett. **120**, 217201 (2018).

[18] D. Foster, C. Kind, P. J. Ackerman, J.-S. B. Tai, M. R. Dennis, and I. I. Smalyukh, Two-dimensional skyrmion bags in liquid crystals and ferromagnets, Nat. Phys. **15**, 655 (2019).

[19] S. S. Choi, S. M. Morris, W. T. S. Huck, and H. J. Coles, Electrically tuneable liquid crystal photonic bandgaps, Adv. Mater. **21**, 3915 (2009).

[20] T. N. Orlova, R. I. Iegorov, and A. D. Kiselev, Light-induced pitch transitions in photosensitive cholesteric liquid crystals: Effects of anchoring energy, Phys. Rev. E **89**, 012503 (2014).

[21] H. K. Bisoyi and Q. Li, Light-directed dynamic chirality inversion in functional self-organized helical superstructures, Angew. Chem., Intl. Ed. **55**, 2994 (2016).

[22] R. S. Zola and Q. Li, in *Functional Organic and Hybrid Nanostructured Materials*, edited by Q. Li (Wiley, New York, 2018), Chap. 8, pp. 307–357.

[23] H. K. Bisoyi, T. J. Bunning, and Q. Li, Stimuli-driven control of the helical axis of self-organized soft helical superstructures, Adv. Mater. **30**, 1706512 (2018).

[24] S. Heinze, K. von Bergmann, M. Menzel, J. Brede, A. Kubetzka, R. Wiesendanger, G. Bihlmayer, and S. Blugel, Spontaneous atomic-scale magnetic skyrmion lattice in two dimensions, Nat. Phys. **7**, 713 (2011).

[25] A. O. Leonov, A. N. Bogdanov, and K. Inoue, Toggle-switch-like crossover between two types of isolated skyrmions within the conical phase of cubic helimagnets, Phys. Rev. B **98**, 060411(R) (2018).

[26] A. O. Leonov, T. L. Monchesky, J. C. Loudon, and A. N. Bogdanov, Three-dimensional chiral skyrmions with attractive interparticle interactions, J. Phys.: Condens. Matter **28**, 35LT01 (2016).

[27] A. O. Leonov, Surface anchoring as a control parameter for shaping skyrmion or toron properties in thin layers of chiral nematic liquid crystals and noncentrosymmetric magnets, Phys. Rev. E **104**, 044701 (2021).

[28] B. M. A. G. Piette, B. J. Schroers, and W. J. Zakrzewski, Multisolitons in a two-dimensional skyrme model, Z. Phys. C-Particles Fields **65**, 165 (1995).

[29] D. Capic, D. A. Garanin, and E. M. Chudnovsky, Skyrmion-skyrmion interaction in a magnetic film, J. Phys.: Condens. Matter **32**, 415803 (2020).

[30] C. Ross, N. Sakai, and M. Nitta, Skyrmion interactions and lattices in chiral magnets: Analytical results, J. High Energy Phys. 02 (2021) 95.

[31] L. Rózsa, A. Deák, E. Simon, R. Yanes, L. Udvardi, L. Szunyogh, and U. Nowak, Skyrmions with Attractive Interactions in an Ultrathin Magnetic Film, Phys. Rev. Lett. **117**, 157205 (2016).

[32] S. M. Vlasov, A. O. Leonov, and V. M. Uzdin, Skyrmion flop transition and congregation of mutually orthogonal skyrmions in cubic helimagnets, J. Phys.: Condens. Matter **32**, 185801 (2020).

[33] H. R. O. Sohn, S. M. Vlasov, V. M. Uzdin, A. O. Leonov, and I. I. Smalyukh, Real-space observation of skyrmion clusters with mutually orthogonal skyrmion tubes, Phys. Rev. B **100**, 104401 (2019).

[34] J. C. Loudon, A. O. Leonov, A. N. Bogdanov, M. C. Hatnean, and G. Balakrishnan, Direct observation of attractive skyrmions and skyrmion clusters in the cubic helimagnet Cu_2OSeO_3, Phys. Rev. B **97**, 134403 (2018).

[35] H. Du, X. Zhao, F. N. Rybakov, A. B. Borisov, S. Wang, J. Tang, C. Jin, C. Wang, W. Wei, N. S. Kiselev, Y. Zhang, R. Che, S. Blügel, and M. Tian, Interaction of Individual Skyrmions in a Nanostructured Cubic Chiral Magnet, Phys. Rev. Lett. **120**, 197203 (2018).

[36] I. I. Smalyukh, Liquid crystal colloids, Annu. Rev. Condens. Matter Phys. **9**, 207 (2018).

[37] Y. Yuan, A. Martinez, B. Senyuk, M. Tasinkevych, and I. I. Smalyukh, Chiral liquid crystal colloids, Nat. Mater. **17**, 71 (2018).

[38] S. Ramaswamy, R. Nityananda, V. A. Raghunathan, and J. Prost, Power-law forces between particles in a nematic, Mol. Cryst. Liq. Cryst. Sci. Technol., Sect. A **288**, 175 (1996).

[39] R. W. Ruhwandl and E. M. Terentjev, Long-range forces and aggregation of colloid particles in a nematic liquid crystal, Phys. Rev. E **55**, 2958 (1997).

[40] T. C. Lubensky, D. Pettey, N. Currier, and H. Stark, Topological defects and interactions in nematic emulsions, Phys. Rev. E **57**, 610 (1998).

[41] B. I. Lev and P. M. Tomchuk, Interaction of foreign macrodroplets in a nematic liquid crystal and induced supermolecular structures, Phys. Rev. E **59**, 591 (1999).

[42] B. I. Lev, S. B. Chernyshuk, P. M. Tomchuk, and H. Yokoyama, Symmetry breaking and interaction of colloidal particles in nematic liquid crystals, Phys. Rev. E **65**, 021709 (2002).

[43] J.-i. Fukuda and S. Žumer, Confinement effect on the interaction between colloidal particles in a nematic liquid crystal: An analytical study, Phys. Rev. E **79**, 041703 (2009).

[44] O. M. Tovkach, S. B. Chernyshuk, and B. I. Lev, Theory of elastic interaction between arbitrary colloidal particles in confined nematic liquid crystals, Phys. Rev. E **86**, 061703 (2012).

[45] B. I. Lev, J.-i. Fukuda, O. M. Tovkach, and S. B. Chernyshuk, Interaction of small spherical particles in confined cholesteric liquid crystals, Phys. Rev. E **89**, 012509 (2014).

[46] O. M. Tovkach, S. B. Chernyshuk, and B. I. Lev, Colloidal interactions in a homeotropic nematic cell with different elastic constants, Phys. Rev. E **92**, 042505 (2015).

[47] V. M. Pergamenshchik, The model of elastic multipole, J. Mol. Liq. **267**, 337 (2018).

[48] S. B. Chernyshuk and E. G. Rudnikov, Theory of elastic interaction between axially symmetric 3D skyrmions in confined chiral nematic liquid crystals and in skyrmion bags, Liq. Cryst. **50**, 9 (2023).

[49] H. R. O. Sohn, C. D. Liu, and I. I. Smalyukh, Schools of skyrmions with electrically tunable elastic interactions, Nat. Commun. **10**, 4744 (2019).

[50] A. O. Leonov, Skyrmion clusters and chains in bulk and thin-layered cubic helimagnets, Phys. Rev. B **105**, 094404 (2022).

[51] F. N. Rybakov, A. B. Borisov, S. Blügel, and N. S. Kiselev, New spiral state and skyrmion lattice in 3D model of chiral magnets, New J. Phys. **18**, 045002 (2016).

[52] J.-S. B. Tai and I. I. Smalyukh, Surface anchoring as a control parameter for stabilizing torons, skyrmions, twisted walls, fingers, and their hybrids in chiral nematics, Phys. Rev. E **101**, 042702 (2020).

[53] W. Legrand, D. Maccariello, F. Ajejas, S. Collin, A. Vecchiola, K. Bouzehouane, N. Reyren, V. Cros, and A. Fert, Room-temperature stabilization of antiferromagnetic skyrmions in synthetic antiferromagnets, Nat. Mater. **19**, 34 (2020).

[54] J. Müller, A. Rosch, and M. Garst, Edge instabilities and skyrmion creation in magnetic layers, New J. Phys. **18**, 065006 (2016).

[55] S.-Z. Lin, C. Reichhardt, C. D. Batista, and A. Saxena, Particle model for skyrmions in metallic chiral magnets: Dynamics, pinning, and creep, Phys. Rev. B **87**, 214419 (2013).